December 2020

Sedimentology, Sequence Stratigraphy, and High-Precision U-Pb Age Constraints on the Late Paleozoic Ansilta Formation, Calingasta-Uspallata Basin, NW Argentina

John Ethan Malone
University of Wisconsin-Milwaukee

SEDIMENTOLOGY, SEQUENCE STRATIGRAPHY, AND HIGH-PRECISION U-PB AGE CONSTRAINTS ON THE LATE PALEOZOIC ANSILTA FORMATION, CALINGASTA-USPALLATA BASIN, NW ARGENTINA

by

John Ethan Malone

A Thesis Submitted in
Partial Fulfillment of the
Requirements for the Degree of

Master of Science
in Geosciences

at

The University of Wisconsin – Milwaukee
December 2020

ABSTRACT

Sedimentology, Sequence Stratigraphy, and High-Precision U-Pb Age Constraints on the Late Paleozoic Ansilta Formation, Calingasta-Uspallata Basin, NW Argentina

by

John Ethan Malone

The University of Wisconsin – Milwaukee, 2020
Under the Supervision of Dr. John Isbell, 2020

The Ansilta Formation, located several kilometers east of the Astronomical Observatory El Leoncito near Barreal, San Juan Province, Argentina was deposited during the late Mississippian to early Pennsylvanian. This succession includes glacimarine, nearshore, and fluvial systems deposited at the mid-Carboniferous portion of the late Paleozoic ice age within the Calingasta—Uspallata Basin on the western margin of the Protoprecordillera. The lower member of the Ansilta Formation is equivalent to the nearby Leoncito, Majaditas, and Hoyada Verde formations, and is composed of diamictite, conglomerates, sandstones, pebbly mudstones, and laminated mudstone. Glacial environments are unique in that facies changes occur as a result of glacial fluctuations that may be independent from changes of relative sea-level. For this reason, an alternative conceptual framework outside of the traditional sequence stratigraphic approach is necessary to understand these strata. The lower glacial member (0-540 m) records at least five glacial advances, where glacial dynamic signatures are interpreted using glacial sequence stratigraphy and glacial systems tracts (GST). The upper member of the Ansilta Formation (540-700 m) consists of progradational shallow marine and fluvial strata with conglomerates, sandstones, and mudstones. This assemblage shows no direct evidence of continued glaciation in the basin due to the absence of glacially faceted clasts and diamictites, representing a major deglaciation phase in western Argentina and is part of the stepped

deglaciation across Gondwana that ended elsewhere in the late Permian. Additionally, samples were collected from various sandstones throughout the formation for detrital zircon U-Pb geochronology to determine sediment provenance as a way of isolating different glacial sources and to assist in bracketing sequences. Results indicate multiple glacial advances, with at least three distinct source areas. The lowermost stage includes locally sourced and recycled underlying Ordovician and Silurian basement, represented by similar Famatinian (460-500 Ma) and Mesoproterozoic peaks (1050-1400 Ma) peaks, with the Mesoproterozoic source likely reworked locally from the underlying basement or derived from the Sierra de Pie de Palo range in the western Sierra Pampeanas. The middle stages of the upper glacial member show a population distinct unto itself, with a peak during the Mississippian (330-360 Ma). Pebble counts recorded along the section showed increasing quantities of plutonic and metasedimentary rock clasts and decreasing amounts of sedimentary clasts from the bottom to the top of the glacial interval. This is attributed to the un-roofing of sedimentary strata and subsequent erosion of the crystalline core of the Protoprecordillera, resulting in the influx of Carboniferous first-cycle sediments. The uppermost stage shows relations based on K-S statistical results to formations within the Paganzo basin to the northeast, which could represent a temporal link between the Calingasta-Uspallata and Paganzo basins during the late Carboniferous, manifested as distal outwash from braided fluvial systems.

TABLE OF CONTENTS

LIST OF FIGURES

LIST OF TABLES

ACKNOWLEDGEMENTS

I would like to start off by thanking my advisor Dr. John Isbell, whose counsel and direction was invaluable in the execution of this project, and for the numerous opportunities with which I was allowed to assist, furthering my geologic expertise in both field and laboratory. I would also like to thank Dr. Julie Bowles for assistance in the field as well as our Argentine colleagues Dr. Alejandra Pagani from the Museo Paleontológico Egidio Feruglio (MEF) and Dr. Arturo Taboada from the Universidad Nacional de la Patagonia for their assistance obtaining site permits and logistics in the field. Gratitude goes to the Arizona LaserChron Center at the University of Arizona for the use of their equipment and lab. Special thanks to former PhD candidate and fellow graduate student Dr. Kathryn Pauls, who was of great assistance in providing context for much of my detrital zircon data and the regional occurrence of potential source terranes. Many thanks to my funding sources: The National Science Foundation's International Research Experiences for Students (IRES) Grant and UWM Department of Geosciences for the financial support provided. Finally, many thanks go to my friends and family who have supported me along the way.

1. Introduction

The Late Paleozoic Ice Age (LPIA) is the longest icehouse interval during the Phanerozoic. Recent studies, provided by Fielding et al. (2008), Isbell et al. (2012), Montañez and Poulsen (2013), Craddock et al. (2019) and López-Gamundi et al. (2020) propose that this event consisted of multiple, diachronous glacial episodes as numerous ice sheets advanced and retreated across the Gondwana supercontinent. The LPIA had substantial impacts on Earth's geosphere at southern latitudes, and far field effects of this event may be observed in the northern hemisphere (Crowell, 1978; 1999; Crowell and Frakes, 1978; Heckel, 2008; Isbell et al., 2003; Isbell et al., 2012; Isbell et al., 2016; Kissock et al., 2018).

Glacial and glacially influenced diamictites in southern and central South America occur in the late Paleozoic basins and paleovalleys of Argentina, Brazil, Uruguay, Paraguay, and Bolivia (Limarino et al., 2014a; López-Gamundí et al., 2020; Fig. 1). Glaciation began in western Gondwana during the Late Devonian and ceased by the early Pennsylvanian. However the Tarija Basin in northern Argentina and southern Bolivia and Peru experienced sedimentation until the end of the Pennsylvanian as did the Paraná Basin in Brazil, the Chaco-Paraná Basin in eastern Argentina, the Sauce Grande Basin in Eastern Argentina, and the basin associated with the Sierra de la Ventana Fold Belt (López-Gamundí and Buatois, 2010; Isbell et al., 2012; Limarino et al., 2014b; Craddock et al., 2019; López-Gamundí et al., 2020; Veroslavsky et al., 2020). Glacial strata in west central Argentina indicate proximal to distal glacimarine, glacially influenced, and rare subglacial deposition. These glaciogenic strata occur in the Calingasta-Uspallata, Paganzo, and Río Blanco basins (López-Gamundí, 1987; Moxness et al., 2018).

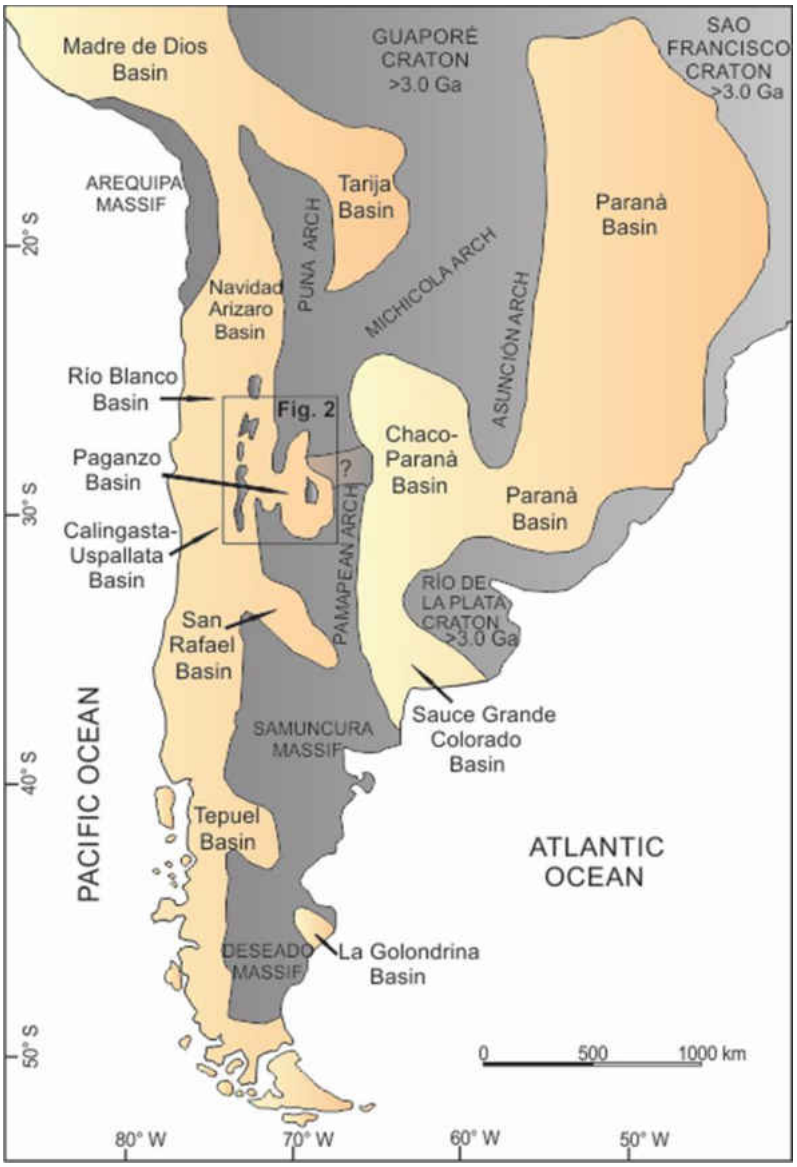

Figure 1 - Regional map of the distribution of late Paleozoic basins and interpreted basement paleotopographic highs in South America. Modified from Henry et al. (2010) and Moxness et al. (2018).

Limited chronostratigraphic studies have been implemented on these strata, focusing instead on the stratigraphy, paleobiology, and palynology as a means of providing relative age relationships (López-Gamundí, 1987; Taboada, 2004; 2009; César et al., 2011, 2020; César and Gutiérrez, 2014). Only recently have studies begun to constrain the absolute age of glaciation within the late Paleozoic South American basins using modern (i.e. single grain U-Pb on zircon) geochronological analytical methods (Gulbranson et al., 2010, Cagliari et al., 2016;

Griffis et al., 2018; Tedesaco et al., 2019; César et al., 2019; Craddock et al., 2019; Pauls et al., 2020; Valdez Buso et al., 2020).

The Calingasta-Uspallata Basin preserves a succession of mid-Carboniferous glacimarine strata. Several formations have been defined, including the Agua de Jagüel, Hoyada Verde, Leoncito, Majaditas, El Paso and Ansilta formations. Correlation between these formations is achieved using marine invertebrate index fossils, palynomorph, and lithostratigraphic assemblages (César and Gutiérrez, 2000; Taboda, 2004; Taboda, 2009; César et al., 2011, 2014, 2020; Limarino et al., 2014a). However, no isotopic ages or detrital zircon analyses are available in the Calingasta-Uspallata Basin to further constrain the age of deposition, provide a source of provenance for sediments, or identify possible ice centers.

This study will expand upon current chronologic and stratigraphic knowledge within the Calingasta-Uspallata Basin, focusing on the Ansilta Formation. A facies analysis was conducted on these strata to investigate ice sheet advance and retreat dynamics using glacial systems tracts. The lower member of the Ansilta Formation is a diamictite-bearing interval that was deposited during late Serpukhovian to early Bashkirian, when glaciation was at its maximum extent over western Gondwana (López-Gamundí, 1986; Taboada, 2004; Taboada, 2009; Limarino et al., 2014b; López-Gamundí et al., 2020). A hypothetical ice nucleation site or ice center has been proposed, and is thought to have been situated over the Protoprecordillera and/or on the Sierras Pampeanas ranges in the western Paganzo Basin (Moxness et al., 2018; Pauls et al., 2020). Here, I present a new detrital zircon data set collected from the Ansilta Formation that aids in determining if isolated alpine valley glaciers within the Protoprecordillera had their own provenance or if a distal glacial ice sheet or ice cap further to the east fed ice into these

paleovalleys. This analysis will also define whether or not this paleotopographic high was breached from the east during initial glaciation.

This new detrital zircon data is compared to detrital zircon age distributions from Pauls et al. (2020) and Craddock et al. (2019), which was gathered from the Guandacol and Tupe formations from the western Paganzo Basin. This comparison will aid in deciphering if sediments from the Calingasta-Uspallata Basin share the same sediment provenance as those in the Paganzo Basin to the north-east, which would indicate similarly sourced basement material or reworked early Paleozoic strata.

2. Geologic Setting

The Ansilta formation, which is as much as 750m thick, preserves a thick glacial succession of late Paleozoic strata of the western Precordillera in San Juan and Mendoza Province, Argentina. The Ansilta Formation was deposited along the eastern margin of the Calingasta – Uspallata Basin, in the footwall of the middle Paleozoic fold-and-thrust belt, the Protoprecordillera. Tectonism during the Cenozoic resulted in the formation of the active fold-thrust belt, the modern Precordillera, located east of the present-day Andes. The Protoprecordillera formed as an obducted early Paleozoic accretionary prism in a peripheral arc-related foreland basin setting during the Chañic orogeny, which resulted in the Chilenia terrane being accreted to the Cuyania terrane along the western margin of Gondwana during the Middle Devonian to Early Mississippian (Ramos et al., 1984, 1986; Limarino et al., 2006; Fig. 2). As a result, the synorogenic Calingasta-Uspallata, Río Blanco, and Paganzo basins are separated from those further to the east by the Pampean Arch. Post-collisional extension dominated during

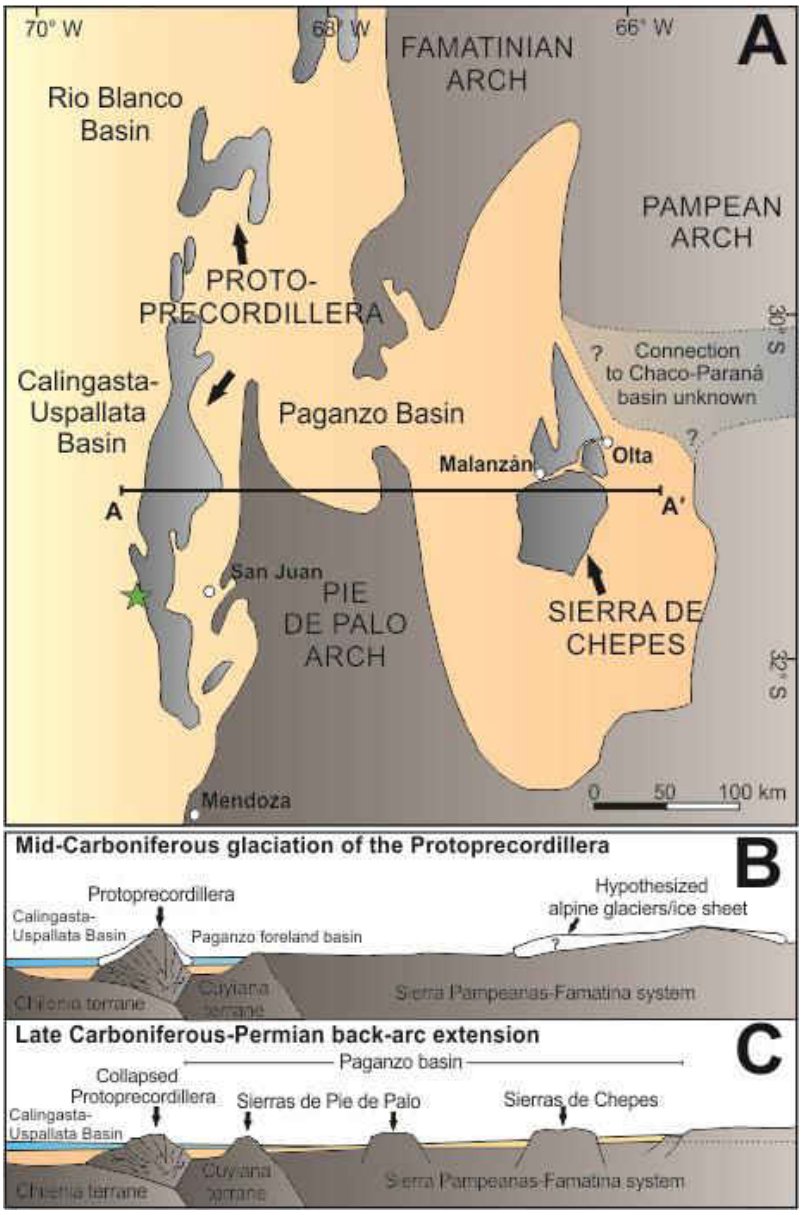

Figure 2 - Paleogeographic model and structural cross-section of northwestern Argentina during the late Paleozoic. Green star denotes study area. Modified from Henry et al. (2010) and Moxness et al. (2018).

the Pennsylvanian as subduction shifted westward, which allowed these basins to widen into a back-arc setting, and likely facilitated collapse of the former Protoprecordillera (Ramos et al., 1984; Ramos et al., 1986; Ramos, 1988; DeCelles and Giles, 1996; Limarino et al., 2006).

During the Viséan through the Serpukhovian, the ancestral Precordillera fold-and-thrust belt superimposed upon the Cuyania terrane is interpreted as a paleotopographic high.

Researchers term this tectonic belt as either the Protoprecordillera Range or the Tontal Arch, the major distinction between the two being the interpreted topographic prominence and elevation of this feature during the early Carboniferous (Aquino et al., 2014; Valdez Buso et al., 2017; Valdez Buso et al., 2020; Pauls et al., 2020) This paleogeographic high allowed alpine glaciers to extend both east and westward into the adjacent basins (López-Gamundí et al., 1994; Dykstra et al., 2006; Limarino et al., 2006, Henry et al., 2010). The supporting evidence for this interpretation includes incised paleovalleys with up to 2,500 m or more in relief, which contain glaciogenic strata deposited subglacially in a fjord paleovalleys or in open marine settings (López-Gamundí, 1986; Henry et al., 2008, 2010; Moxness et al., 2018; Aquino et al., 2014; López-Gamundí et al., 2016; 2020; Valdez Buso et al., 2017, 2020; Alonso-Muruaga et al., 2018; Pauls et al., 2020). These basins preserve a near continuous record of glacimarine sedimentation spanning the Mississippian-Pennsylvanian boundary, and are capped by post-glacial Bashkirian mudstones. A regional unconformity present throughout the Calingasta-Uspallata, Rio Blanco, and Paganzo basins cuts into the post-glacial shale and is overlain by the occurrence of regressive shallow marine and fluvial strata. These strata as well as detrital material from the Sierra Pampeanas being delivered to areas west of the Precordillera range indicate that an increase in base level occurred as a result of the subsidence and collapse of the Protoprecordillera mountain belt during the late Mississippian to early Pennsylvanian (Limarino et al., 2006, 2014; Isbell et al., 2012; Pauls et al., 2020).

Amos and Rolleri (1965), De Rosa (1983), López-Gamundí (1987), Henry et al. (2008), and López-Gamundí et al. (2016; 2020) provide excellent descriptions of late Paleozoic diamictite-bearing strata and sequences exposed in the Calingasta-Uspallata basin, comprising

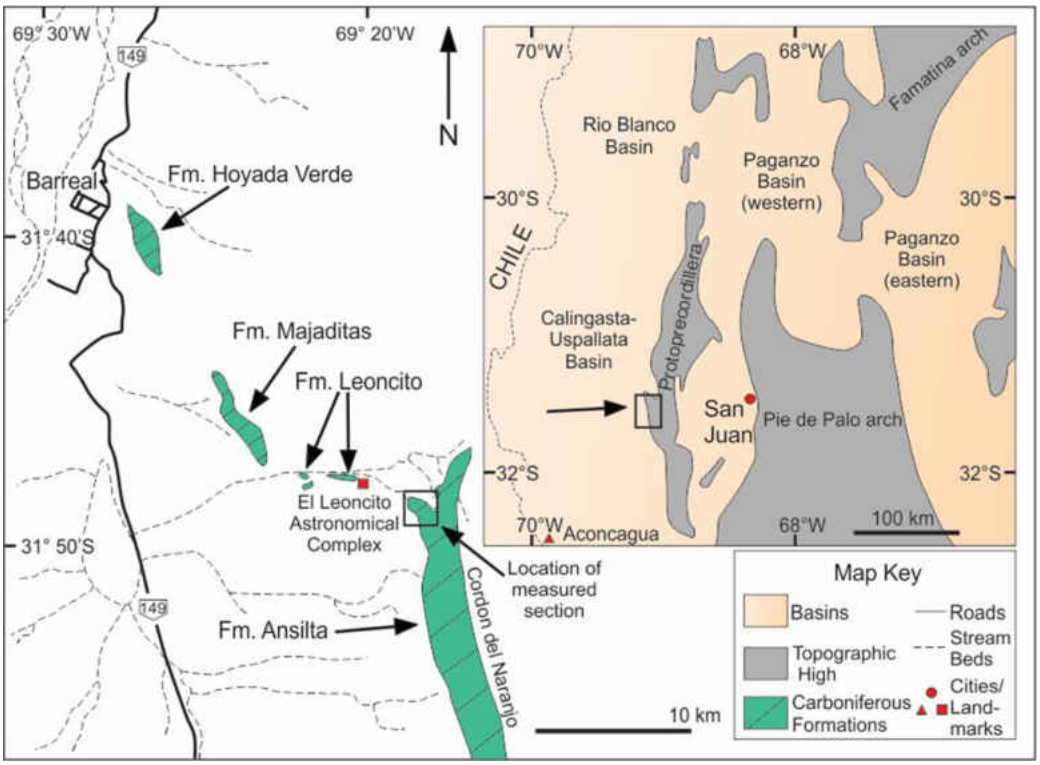

Figure 3 - Location map of Carboniferous-aged formations in the Calingasta-Uspallata Basin. Modified from López-Gamundí and Martínez (2003) and Isbell et al. (2012).

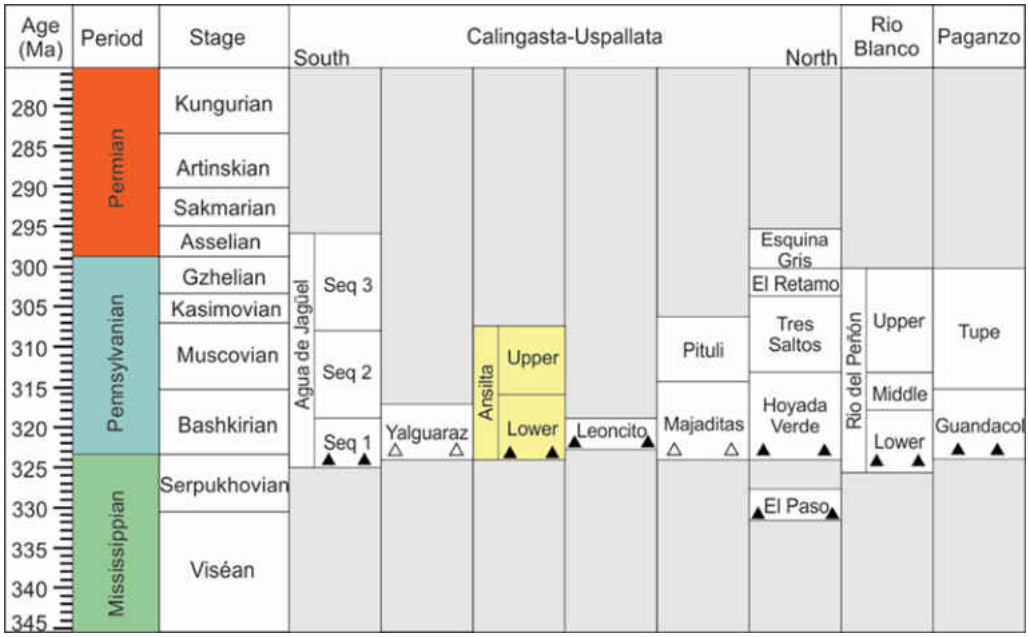

Figure 4 - Correlation of Late Paleozoic Sedimentary units in the Calingasta-Uspallata Basin. Dark triangles represent diamictites and un-filled triangles represents inferred diamictites at the locality. Yellow highlight is the formation of focus for this study. Modified after López-Gamundí et al. (1987), Taboada (2004), Henry et al. (2010), Limarino et al. (2012), and Césari et al. (2020).

the Agua de Jagüel, Hoyada Verde, Leoncito, Majaditas, and Ansilta formations (Fig. 3 & 4).Two depositional successions are identified in the Ansilta Formation, consisting of a lower glaciogenic member and an overlying shallow marine and fluvial sequence, which comprises the upper member. The lower member unconformably overlies the Upper Ordovician to Lower Silurian Hilario and Cabeceras formations and is overlain by the Permo-Triassic Santa Clara Group (Csaky, 1963; Amos and Rolleri, 1965). The lower member of the Ansilta formation is roughly correlative with other glaciogenic strata elsewhere in the basin, and is greater than 530 m thick and is composed of diamictite, conglomerate, sandstone, pebbly mudstone, and shale (López-Gamundí et al., 1987; Taboada, 2004; César et al., 2014). Amos and López-Gamundí (1981) identified six diamictite units in the lower member of the formation, which could be the result of glacial advance and retreat cycles. Based on contradictory reports, it is not known if these diamictites represent glaciomarine or terrestrial deposition, or if the diamictites represented gravity flows (mass transport, debris flows or turbidites) as these units have been interpreted differently by separate researchers. Amos and López-Gamundí (1981) term these diamicite-bearing units as ‘tillites’, which implies subglacial deposition, while López-Gamundí (1986) interpreted these same units as being the result of sediment gravity flows in a glacially influenced continental shelf and slope setting. This study tests these two hypotheses.

3. Study Area and Methodology

The Ansilta formation is located 30 km southeast of the town of Barreal, San Juan Province, Argentina. The Naranjo Range, and its continuation, the Ansilta Range, form a synclinal structure with an approximate north-south trending axis. Spanning nearly 10 km, the formation has been deformed into a series of folds, resulting in several repeated sections and

oblique extensional faults (Amos and Rolleri, 1965). This structure is a result of Cenozoic Andean tectonism, which compressed these strata into their present form.

A 700 m section of the Ansilta Formation was measured and described near Agua de los Burros creek, which occurs 5.5-6.3 km southeast of the Leoncito Observatory in Leoncito National Park (-31.832014, -69.244178). Permits were obtained for this work. This portion of the Ansilta Formation consists of a fault off, south-plunging anticline structure, and our field study focuses on the western limb of this structure (Fig. 5). Bed thickness was measured using a Jacob's staff, Brunton compass, and GPS, noting the observed lithologies, grain and clast composition, and bedding geometries.

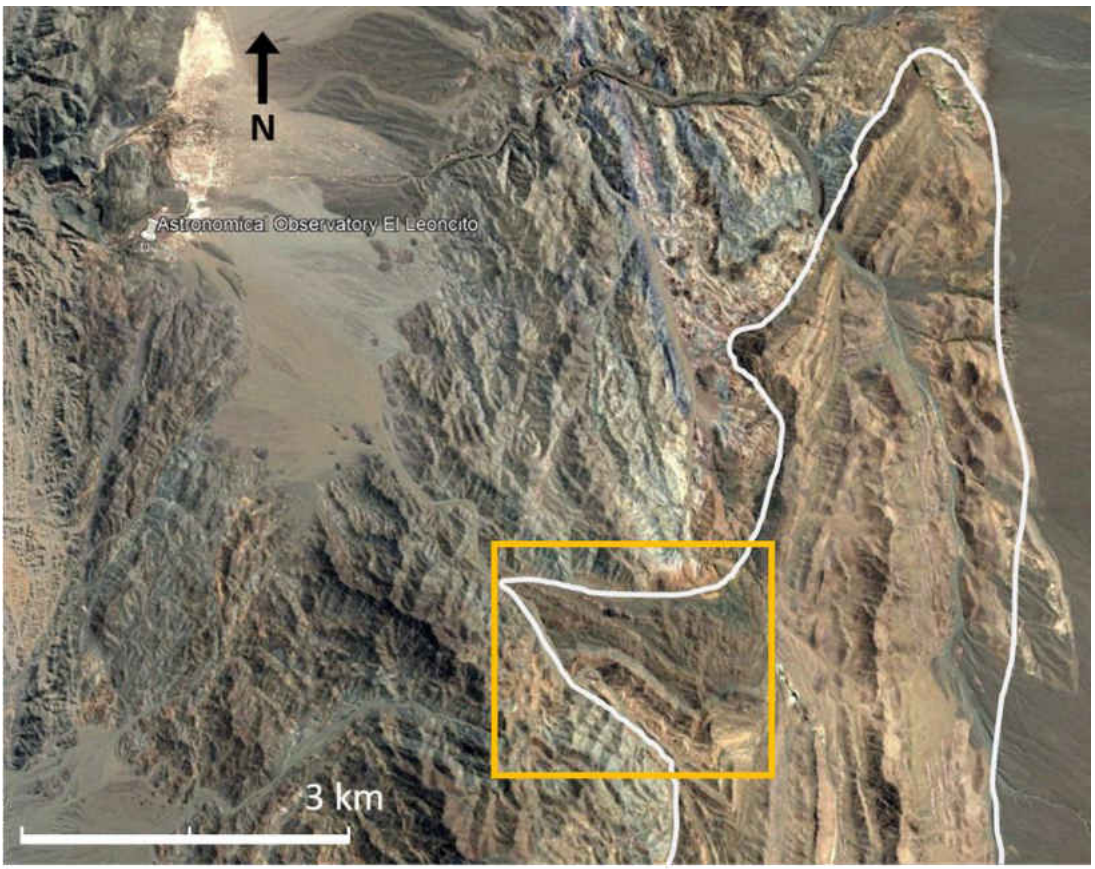

Figure 5 - Satellite map of northern extent of the Ansilta formation (outlined in white). The focus of our research endeavors is on faulted off block exposed along western side of structure (boxed in yellow).

Paleoflow measurements collected using a Brunton compass and corrected for structural dip (40-60°, NW-SE orientation dipping to the southwest) and magnetic declination (13.25° West) may yield inconclusive results due to possible structural rotation of this block by more than 10˚, nonetheless the trend was consistently to the south-west throughout the measured section, which is similar to paleoflow directions measured from other nearby sites (Henry et al., 2010; López-Gamundí et al., 2016).

A detailed stratigraphic column was drafted using traditional techniques with the goal of characterizing lithofacies, assigning a chronostratigraphy using detrital zircon geochronology from sandstone sampled from the various depositional stages, and interpreting the depositional environments as a way of deciphering glacier-ice dynamics and the events directly following glaciation. Glacial systems tracts are identified and defined based on previous work by Powell and Cooper (2002) and Rosenblume and Powell (2019), in order to explain ice dynamics and conceptualize glacial advance and retreat events. This sedimentology and chronostratigraphic analysis is supplemented with three primary provenance techniques to determine sediment source area compositions, which include U-Pb detrital zircon geochronology, pebble counts, and composition of dropstones.

Six samples were collected for detrital zircon geochronology (n=1226 total zircons analyzed). Sampling horizons included the underlying Ordovician and Silurian basement (US1A 1902), three channel-form sandstone beds within the diamictite-bearing portion of the succession (SE1A 1901, SE1D 1905, SE1E 1907), and two sandstones from the overlying regressive successions (SE1F 1910, SE1F 1911). U-Pb geochronology of zircons were conducted by laser ablation inductively coupled plasma mass spectrometry (LA-ICPMS) at the Arizona LaserChron Center (Gehrels et al., 2008, 2014). The analyses involve ablation of zircon

with a Photon Machines Analyte G2 excimer laser equipped with HelEx ablation cell using a spot diameter of 20 microns. Following analysis, data reduction was performed with an in-house Python decoding routine and an Excel spreadsheet (E2agecalc). The ages are shown on relative age-probability diagrams using the routines in Isoplot (Ludwig, 2008). A K-S analysis was completed to compare the age spectra of the samples analyzed here with published data from Craddock et al. (2019) and Pauls et al. (2020).

4. Facies Analysis

The Ansilta Formation includes nine facies assemblages: diamictite, conglomerate, graded and current rippled sandstone, wave rippled sandstone, cross-bedded sandstone, CUS sandstone and conglomerate, deformed sandstone, pebbly mudstone, and laminated mudstone. Lithologic classifications were made and modified from previous work in the region, with a focus on assigning system tracts to depositional sequences (cf. Powell and Cooper, 2002; Rosenblume and Powell, 2019) as a means of understanding ice and accommodation dynamics. Facies descriptions and environmental interpretations are shown in Table 1.

4.1. Diamictitie Facies

The diamictitie facies form multiple thick intervals in the lower depositional member (0-540 m).

4.1.1. Diamictitie Facies Description

Diamictites (Dm) occur as cm- to m-scale thick, laterally continuous sheets of massive to weakly stratified units (Fig. 6). The diamictites occur as both matrix-supported and clast-supported (closed framework) units. The matrix consist of varying amounts of mud and fine

Lithofacies and Depositional systems

Lithofacies	Features	Genesis	Depositional Environment
Diamictite (Dm)	Weakly laminated and bedded, clast- to matrix-supported, rounded and striated clasts; sharp and erosional contacts; slumps, folds, load structures, glide planes imbrication, contorted beds	Sediment gravity flows, mass transport, meltwater plume and iceberg rain-out, pods deposited as iceberg dump structures	Glacial: morainal bank, ice proximal and distal glacimarine
Conglomerate (Cg)	Massive and bedded clast-supported sandy conglomerates, fine- to coarse-grained sandstone; erosional and sharp basal contacts; normal and inverse grading, planar cross-bedding, imbricated clasts	Confined/channelized flow, hypercocentrated density flows, density-drive underflows, glacier base discharge	Glacial: subaqueous channel incising a morainal bank, ice proximal grounding line fan
Graded and Current Rippled Sandstone (Sgr)	Fine- to medium-grained sand; normally graded, isolated and rarely stacked asymmetric ripples, climbing ripples, ribbon furrow	Sediment reworking via current activity, hyperpycnal or turbid flows	Glacial: ice proximal and ice distal via hyperpycnal flows and/or turbidity currents
Wave Rippled Sandstone (Swr)	Fine- to medium-grained sand; stacked symmetric ripples, rare plane beds, flaser bedding, mud drapes, cyanobacteria biomats	Sediment reworking and deposition via wave activity	Non-glacial: shoreface progradation
Cross-bedded Sandstone (Sc)	Fine- to coarse-grained sand, rare interlayered conglomerate; sharp and erosional contacts; planar cross-bedding, trough cross-bedding rare bioturbation	Channelized flow, fluvial processes	Non-glacial: fluvial progradation

Table 1 – Summary of lithofacies characteristics and their interpreted depositional systems

Lithofacies	Features	Genesis	Depositional Environment
CUS Sandstone and Conglomerate (CS)	Fine- to coarse-grained sand, interlayered conglomerate; sharp erosional, and gradational contacts; coarsening upward packages, rare planar cross-bedding, bioturbation	Channelized flow, distributary deltaic processes	Non-glacial: deltaic progradation
Deformed Sandstone (Sd)	Fine- to medium-sand, grain- (clean) or matrix- (muddy) supported, often fining upwards; deformational, sharp and erosional contacts; sand boudins sheath folds, slumps, contorted beds	Turbidity currents, loading, subaqueous mass-tranport, slope failure	Glacial: ice proximal and ice distal glacimarine, morainal bank Non-glacial: shallow marine shelf or shoreface setting
Pebbly mudstone (Mp)	Claystone and siltstone with outsized clasts, some sub-verticle penetrating grains, occasional weak bedding, pods of clast-rich diamict (dump structures), slumped beds	Mud deposited via suspension settling of meltwater plume and iceberg rain-out, clasts transported via ice-rafting	Glacial: ice distal
Mudstone – Laminated (Ms)	Fissile thin laminated shale with few observable structures, condensed intervals, marlstone, organic debris	Meltwater plume and hemipelagic suspension settling, turbid cloud settling, marls form from pelagic settling under siliclastic starved conditons	Glacial: interglacial shelf, Non-glacial: flooding events during shoreface, deltaic, and fluvial progradation

Table 1 – continued.

.
sand, and ranging from clast-rich (>5% < 50% clasts) to clast-poor (<5% clasts) intermediate diamictites (cf. Moncrieff, 1989; Hambrey and Glasser, 2012). About 10% of clasts exhibit faceted and striated features, and the average clast size is 2.2 cm (ranging from 4 mm to 9.5 cm), with <1% of clasts being larger than 25.6 cm and the largest being 42 cm in diameter (Fig. 6A). Clasts within the lowermost diamictites are predominately sedimentary in origin (sandstone clasts are most abundant with rare occurrences of micritic limestone), with increasing quantities of metasedimentary (predominantly schist and quartzite) and plutonic clasts are observed higher in the formation. In clast counts (n=50), 84% of clasts are sandstone, 15% are quartz, and 1% are metasedimentary in the lowest portion of the measured section, and these percentages transition in the upper portion of the lower member to 70% sandstone, 20% metasedimentary, and 10% plutonic clasts (Fig. 6B). In the diamictites, some clasts are inclined at high angles to bedding, with the occasional clast penetrating laminations.

Massive diamictites exhibit no internal stratification, and can show lithified structurally controlled subhorizontal parting and fissile textures. These units ranges in thickness from 0 to 5 m, and interfinger with stratified diamictite, conglomerate, and sandstone. Bedded diamictites are composed of individual thin beds greater than 0.5 m thick, with the stratification represented by weak laminations or clast imbrication (Fig. 6C). These units often grade vertically and laterally into clast-poor to clast-rich diamictites, within which may contain pebbly sandstones and mudstones. Basal contacts are either sharp or erosional, while the upper contacts are either sharp or gradational with laterally adjacent or overlying units. Pods of stratified diamictite surrounded by deformed pebbly mudstone or laminated mudstone are found in the section (60 m and 230 m), with the deformation occurring perpendicular to the pod-like structure.

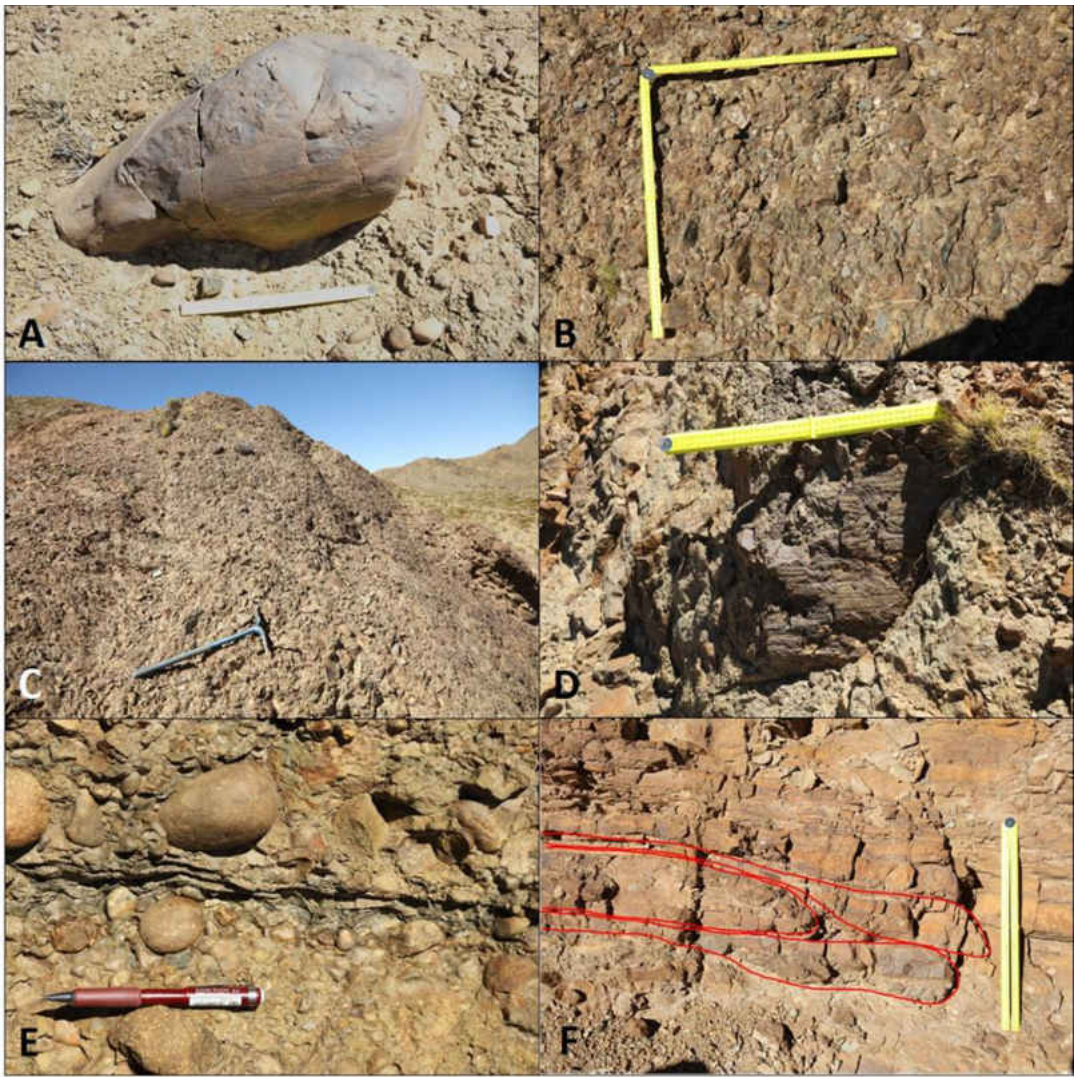

Figure 6 – Photo mosaic of the diamictite facies association. Ruler = 0.5 m; Pick = 1 m. A. Striated sandstone boulder in diamictite. B. Clast-supported and clast-rich diamictite. C. Weakly bedded clast-rich diamictite. D. Plough or sole marks caused by mass transport of diamicite. E. Glide plane separating diamicitie. F. Stacked slump beds of diamictite and sandstone.

Diamictite intervals are deformed, with cm- to m- scale folds or soft sediment striated surfaces (Fig. 6D). Glide planes or striated surfaces were occasionally found at or near the base of thick diamictite-bearing units (Fig. 6E). Folds form discontinuous bodies that display recumbent fold noses. Some folds are stacked and may show dewatering structures (Fig. 6F). The orientation of the fold noses suggest vergence or transport to the southwest. In addition, thin beds (<1 m) of sandy conglomerates and medium-grained sandstones are interlayered in the thicker diamictites, and these strata wedge out latterly when traced over several meters.

4.1.2. Diamictitie Facies Interpretation

Diamictites were deposited in ice proximal and ice distal settings, as: 1) iceberg rain-out of clay- to boulder-sized sediments as indicated by clast piercing weak stratification and the near vertical orientation of clast long axis, 2) meltwater plume rain-out of clay, silt, and sand emerging from the glacier terminus as suggested by massive, clast-poor diamictites , 3) sorting by water either due to meltwater discharge or density driven processes near the grounding line as suggested by interlayered normal graded sandstones in bedded diamictite, and 4) subaquaeous debris flows, slides , and slumps as indicated by cm- to m- scale folded clast-rich diamictites (cf. López-Gamundí, 1987; 1997; Dowdeswell et al., 1994; Powell and Cooper, 2002; Henry et al., 2010). The occurrence of striated and faceted clasts indicate their glacial affinity. Bedded and massive diamictites are produced by one or a combination of these processes, with fine grained material being deposited via suspension settling from meltwater and turbidity plumes with clasts introduced by ice rafting, or by debris flows, which commonly stem from the grounding line and or the slopes of a subaqueous morainal banks, due to these being unstable depositional environments where calving, pushing, and squeezing occur in front of a glacier (cf. López-Gamundí, 1991). Additional activity such as movement from earthquakes, storm-driven waves, and shock from calving icebergs contacting the substrate also prompt mass transport and debris flow processes in glacimarine environments. Deformation, such as slumping and folding, occurs as reworked material collapses downslope, while folding occurs due to frictional differences along a glide plane as material moved across the basal surface or as density contrasts between units post-depositionally (Fig. 6D).

Owing to the thickness of, interfingering of multiple different facies of sandstone, conglomerate, mudstone, and diamictite, and the persistent deformation throughout the

diamictite intervals, I interpret that initial deposition was probably along the front of a morainal bank, near the terminus of a wet-based tidewater glacier, with subsequent strata being deposited on and migrating over the top of each other due to changing glacial conditions (cf. Powell, 1983; Cai et al., 1997; Henry, 2010). A morainal bank is a drawn-out bank of diamictite, conglomerate, sandstone, and mud that forms as a result of rapid sedimentation in front of a grounded, tidewater glacier. Many depositional processes, such as melt-out from the glacier front, rain-out from icebergs, the pushing and squeezing of advancing glaciers, and meltwater plume deposition can collectively form a morainal bank. Bank core systems contain a poorly sorted mixture of conglomerate, sandstone, and diamictite facies, rare muds, and may include glaciotectonic compression and thrust structures. Morainal bank front systems generally consist of sediment reworking via gravity flows due to the advance and retreat of glaciers and the slope of a morainal bank, resulting in unstable bank deposits. Grounding-line fan deposits, fans deposited in front of the point source of a subglacial discharge jet, consist of stratified sands and conglomerates, and some sediment gravity flow deposits. Modern studies on glacimarine setting have recorded morainal banks as thick as 200 m (Cai et al., 1997; Powell, 2002). Field relations and unit geometries indicate at least three separate advance/retreat cycles containing morainal bank deposits ranging in thickness from 22 m to 150 m, and are separated from each other by ice distal facies.

Clasts within the diamictite interval exhibit rounded and faceted surfaces and striations suggesting mechanical wear during transport, characteristics common in glaciated environments. Well-rounded clasts likely underwent multiple cycles of transport within a glacially influenced system. Striae orientations on individual clasts were nonuniform when compared to adjacent clasts, indicating that these strata were not transported or deposited

subglacially. Sandstone clasts are most abundant in the lower diamictite interval, derived from Lower Proterozoic to lower Paleozoic aged strata that form the Protoprecordillera. A single micritic limestone clast near the basal contact of the formation likely belongs to the Ordovician-aged San Juan Limestone. Strata of this formation are exposed in the current Precordillera range 18 km to the east-north-east of the Ansilta study locality, and extensive exposures occur along the eastern side of the modern range 50 to 60 km to the east. A clast belonging to this formation along with the sandstone clast suggest local derivation of sediment within the lower member of the Ansilta Formation. Higher in the lower member succession, granitic, vein quartz, and metamorphic clasts are eroded from the Middle Carboniferous intrusions and pre-Carboniferous metasedimentary units from the Protoprecordilleran core (Ramos, 1988; Azcuy, 1999).

Slumped and folded diamictite were formed by the reworking of sediments from cohesive debris flows and mass transport processes (Mulder and Alexander, 2001). Orientations of slumps consistently trend to the south/southwest, likely oriented perpendicular to and caused by the unstable environment attributed to morainal banks. The vertical and lateral grading of these deposits into sandstone and mudstone laden units may have been deposited by other sediment gravity flow processes, such as hyperconcentrated flows and turbidity currents.

4.2. Conglomerate Facies

The conglomerate facies occurs throughout the lower member of the measured section (0-540 m).

4.2.1. Conglomerate Facies Description

The conglomerate (Cg) facies consists of clast-supported sandy conglomerate and fine- to coarse-grained sandstone (Fig. 7). Conglomerate clasts range in size from 0.04 to 26 cm, while the average size is 2 cm in diameter, as shown by clast counts (n=50). Conglomerate bedding varies from 4 cm thick beds up to 6 m thick massively bedded units, however massive beds are rarely observed in this section. Basal contacts are sharp or erosional, while upper contacts are sharp and occasionally gradational where conglomerates grade normally into sandstone or diamictite respectively. Conglomerates can occur as laterally extensive sheets, but pinch out into adjacent units when traced over several tens to a hundred meters. Interlayered sandstone occurs and is medium- to coarse-grained, and bed thicknesses range from 1 to 50 cm. Most sandstones associated with conglomerates are structureless/massive, however rare cross-laminations occur. Conglomerates occasionally preserve primary sedimentary structures, including planar cross-beds and imbricated clasts (Fig. 7A). Internal fabrics of conglomerates are massive, normal or inverse graded beds. Thin beds typically show normal grading, whereas thicker beds (>50cm) more commonly show inverse grading (Fig. 7B).

A 150m wide channel and levee system composed of interfingering conglomerate and sandstone beds occurs 170 m from the base of the section and is encapsulated by diamicite (Fig. 7C & 7D). Internal channels are up to 20 m wide and have erosional basal and lateral contacts with the surrounding diamictite. Channel conduits are occupied by conglomerate while the channel fill, wings consist of muddy sandstone with the sediments fining laterally and perpendicular to flow.

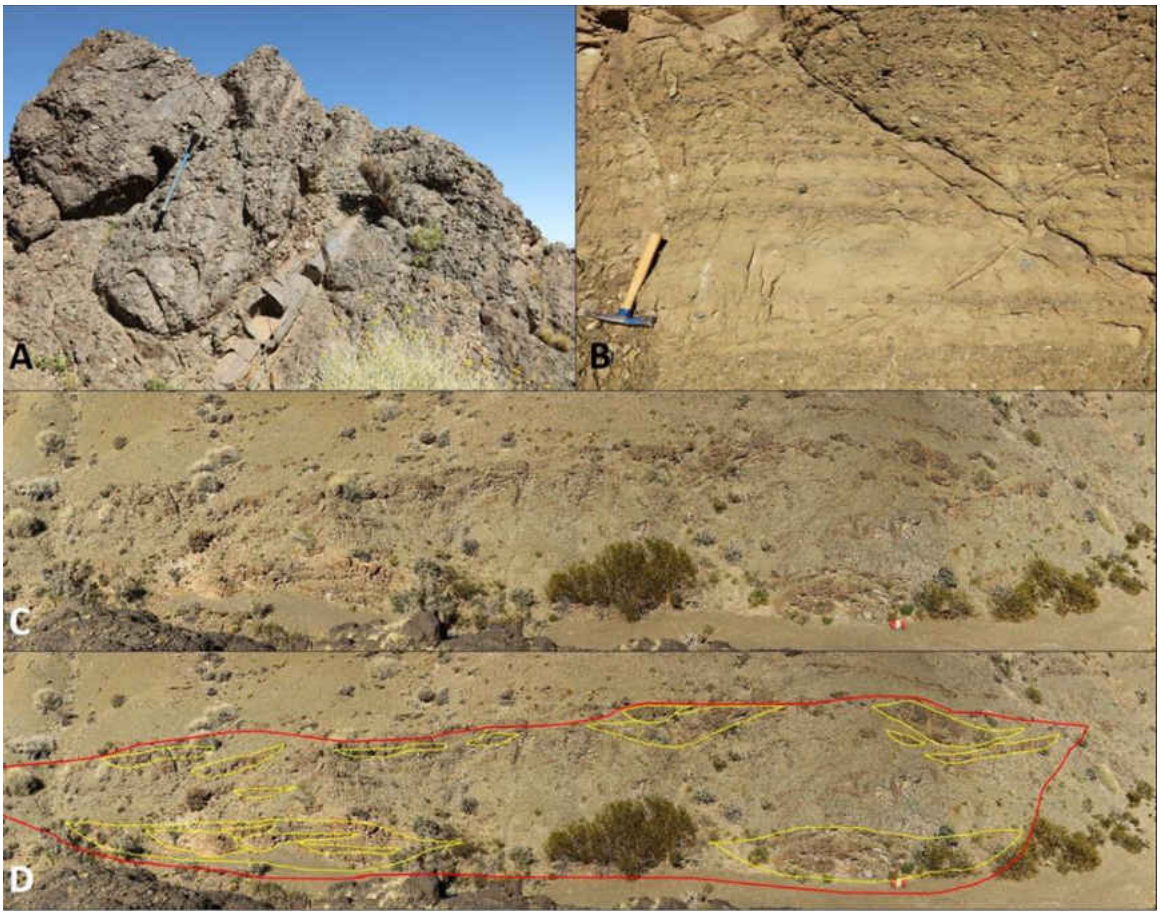

Figure 7 – Photo mosaic of the conglomerate facies association. A. Cross-bedded conglomerate and sandstone. Hoe pick (1 m) for scale B. Rhythmically bedded small scale cohesive debris flows of conglomerate grading into sandstone, interpreted as a grounding line fan deposit. Rock hammer (50 cm) for scale. C. Channel system (150 m) with amalgamated and isolated channels. D. Annotated photo of Figure 7C.

4.2.2. Conglomerate Facies Interpretation

The conglomerate facies was deposited by either one or a combination of the following processes: 1) confined to unconfined flow in a subaqueous channel system, 2) density-driven underflows, 3) hyperconcentrated density flows, 4) and discharge flow from a glacier base.

Subaqueous channel systems are mapped worldwide, in both modern and ancient environments, and usually consist of complex dendritic-like arrangement of tributary channels that converge and gather flow into large channels that run down a slope, becoming distributary-like channels and vanishing once they reach the basin floor. Here density-driven sediment flows

shift from confined, convergent flow to divergent, unconfined flow. Sediment is typically supplied by continental margin-failure processes or river input. However, in glaciated environments, meltwater outbursts and hyperpycnal flows laden with suspended sediments can also lead to flows within channel conduits (Powell and Domack, 2002).

The 150 m wide channel and levee system located 211 m from the base of the section has a low aspect depth-width ratio of 12.5: 1, which suggests a slope channel fill recording focused flow over an extended period of time (Hofstra et al., 2015; Pemberton et al., 2016). Sediments fine laterally, perpendicular to flow, suggesting a transition from confined to unconfined flow, likely near a channel-lobe transition zone. Due to the surrounding diamictite, this channel likely incised the top of a morainal bank and then was actively receiving sediments form a proximal tidewater glacier. Due to its location in a glacial proximal position and in association with morainal bank deposits, this deposit may be part of a grounding line channel system.

Conglomerates and sandstones that occur as sheet-like bodies and display sharp basal contacts and internal normal grading are interpreted as unconfined flows, perhaps as a fan surface, grounding line fan, or as levees where flow topped the margins of channels, forming lobate splay geometries. The occurrence of these units within thick diamictite-bearing intervals leads us to interpret these features as a grounding line fan deposit. For conglomerate and sandstone that have erosive basal contacts, deposition occurred due to either sedimentation incising a channel, or by turbulent meltwater discharge flowing along the substrate (cf. Powell, 1990).

4.3. Graded and Current Rippled Sandstone Facies

The graded and current rippled sandstone facies occur throughout the lower member of the measured section, often associated with diamictites, conglomerates, and mudstone.

4.3.1. Graded and Current Rippled Sandstone Facies Description

The graded and current rippled sandstone (Sgr) facies occur as both lenticular and sheet-like bodies, often displaying normal grading or are arrange in fining upward packages, and can be found interlayered within diamictite and mudstone at the top of the lower member dominated by glacigenic related facies (Fig. 8). Common primary structures include assymetric ripples, climbing ripples, sole marks, and rib and furrow occur frequently in sandstone throughout the lower member (Fig. 8A-8C). This facies occur as 3 cm to 40 cm thick beds, often as a single rippled surface and rarely stacked, and composed of sub-rounded, fine- to medium-grained sandstone, with rare occurrences of interbedded coarse-grained sandstone and mudstone.

4.3.2. Graded and Current Rippled Sandstone Facies Interpretation

The graded and current rippled sandstone facies represents sediment deposition and modification by current activity. Asymmetric ripples are dominate in the lower diamictite-bearing interval, deposited as a result of unidirectional flow associated with hyperpycnal or turbidity currents (Fig. 8D). Currents are generated by both confined and unconfined flows, however this facies is more apparent in inferred confined flow deposits, due to the association of channel geometry directing flow and the single-direction of current flow, whereas turbidity current generated features are characteristic of unconfined flows.

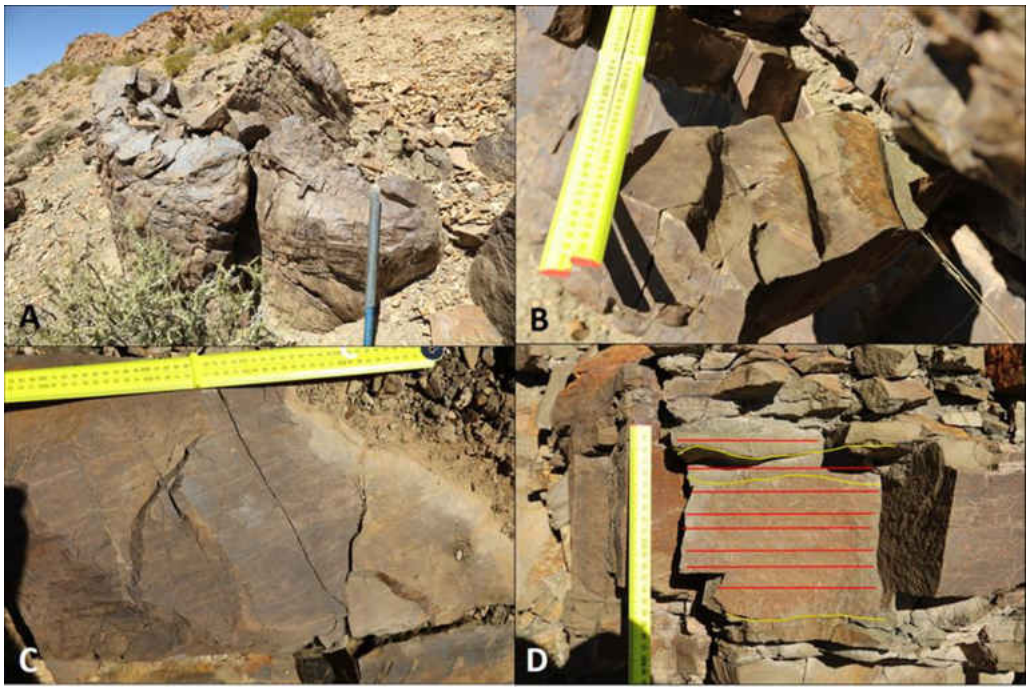

Figure 8 – Photo mosaic of the graded and current rippled sandstone facies association. A. Lenticular body of current rippled sandstone in mudstone. Hoe pick (1 m) for scale. B. Asymmetric current ripples from sandstone body surrounded by mudstone. Ruler (25 cm) for scale. C. Climbing current ripples. Ruler (50 cm) for scale. D. Turbidity current Bouma sequence T_b (red) and T_c (yellow) beds. Ruler (25 cm) for scale.

4.4. Wave Rippled Sandstone Facies

The wave rippled sandstone facies occur throughout the upper member of the measured section (545-560 m), often associated with cross-bedded sandstones, conglomerates, and mudstone.

4.4.1. Wave Rippled Sandstone Facies Description

The wave rippled sandstone (Swr) facies occur as sheet-like bodies and is the most abundant sandstone facies in the upper member (Fig. 9). Symmetric ripples and rib and furrow occur frequently in sandstone throughout the upper member, while occurrences of plane beds, flaser bedding, and cyanobacteria wrinkled textures rarely appear (Fig. 9A-9C). Sandstones occur as 3 to 40 cm thick beds, often stacked, fine- to medium-grained sandstone, with rare occurrences of interbedded coarse-grained sandstone and mudstone.

4.4.2. Wave Rippled Sandstone Facies Interpretation

The wave rippled sandstone facies represents sediment modification by wave activity. In the upper interval, numerous levels of symmetric wave ripples compose the base of coarsening- and shallowing- upward parasequences, indicating oscillatory flow and wave activity. Rare instances of planed off wave ripple crests represent extremely shallow water. Wrinkled textures occupy the troughs of these planed of ripples are interpret as being formed by cyanobacteria mats in very shallow water no more than several cm deep (Schieber, 1999). However, since most of the ripples are symmetrical, this suggests a wave-dominated shoreface environment with the flat-topped ripples and biomats occurring at the top of these successions.

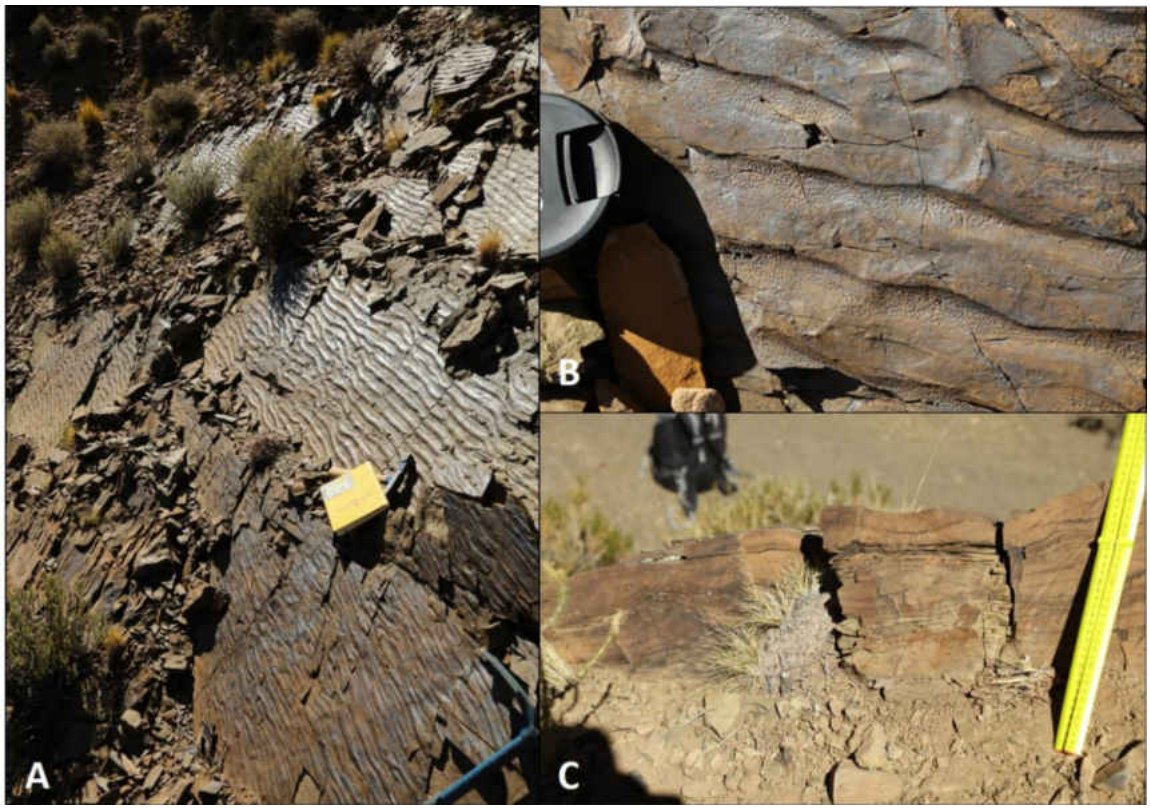

Figure 9 – Photo mosaic of the wave rippled sandstone facies association. A. Stacked wave rippled sandstone. Notebook (25 cm) for scale B. Planed-off wave ripples with cyanobacteria mat traces in the troughs. Camera lens cover (7 cm) for scale, C. Cross-section view of 3-D wave ripples. Ruler (25 cm) for scale.

4.5.1. Cross-bedded Sandstone Facies

The cross-bedded sandstone facies occur in the upper interval of the measured section (670-700 m), often associated with rippled sandstones, conglomerates, and mudstone.

4.5.1. Cross-bedded Sandstone Facies Description

The cross-bedded sandstone (Sc) facies occur as amalgamated sheet or multi-storey geometry bodies (Fig. 10). Basal contacts are erosional or sharp, bedding is often stacked, and internal structures include planar cross-stratification, trough cross-stratification, and rare bioturbation (Fig. 10A-10C). Cross-bedded sandstones are often interbedded with

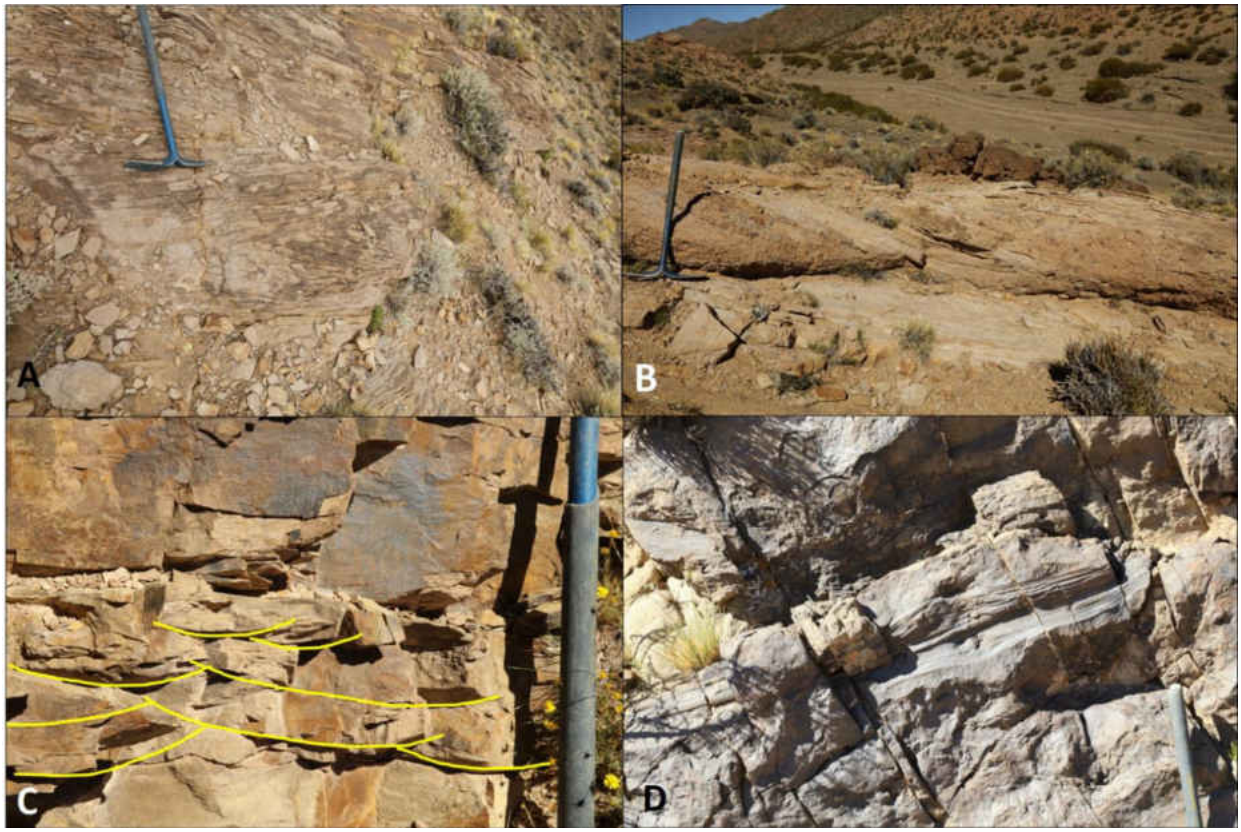

Figure 10 – Photo mosaic of the cross-bedded sandstone facies association. A. Planar cross-bedding in sandstone. Hoe pick (1 m) for scale. B. Downstream accreting foresets of conglomerate and sandstone. Hoe pick (1 m) for scale. C. Trough cross-bedding in sandstone. Hoe pick handle (50 cm) for scale. D. Impression of wood fragment in sandstone. Hoe pick handle (50 cm) for scale.

conglomerate, sandstone, and mudstone. Upper contacts are commonly erosional or sharp, and the cross-bedded sandstones facies consist of massive >0.5 m thick, sandstone displaying sub-rounded, fine- to coarse-grained mature sandstone. An abundance of organic debris was found within sands in the upper interval, primarily wood fragments and rare bioturbation (Fig. 10D). The facies is found in gentle to steeply dipping clinoforms which show downstream accreting foresets and possible overbank splays. Inferred splay deposits typically show graded bedding, which consist of an erosive basal contact, followed by the deposition of coarse grained bed load that transitions into finer grained sediments, and may contain organic terrestrial debris.

4.5.2. Cross-bedded Sandstone Facies Interpretation

The cross-bedded sandstone facies represents aggrading fluvial environments. Towards the top of the upper member, the cross-bedded facies overlies symmetric rippled sandstone and mudstones, indicating a transition from wave-dominated marine system to current-dominated fluvial depositional processes, likely as a braided stream. The preservation of foreset beds indicate ample sediment supply and rapid dune migration downstream under steady-flow conditions (Leclair et al., 2002).

4.6. CUS Sandstone and Conglomerate Facies

The coarsening upward succession (CUS) sandstone and conglomerate facies occur in the upper member of the measured section (565-660 m), often associated with wave rippled sandstones, cross-bedded sandstone, and mudstone.

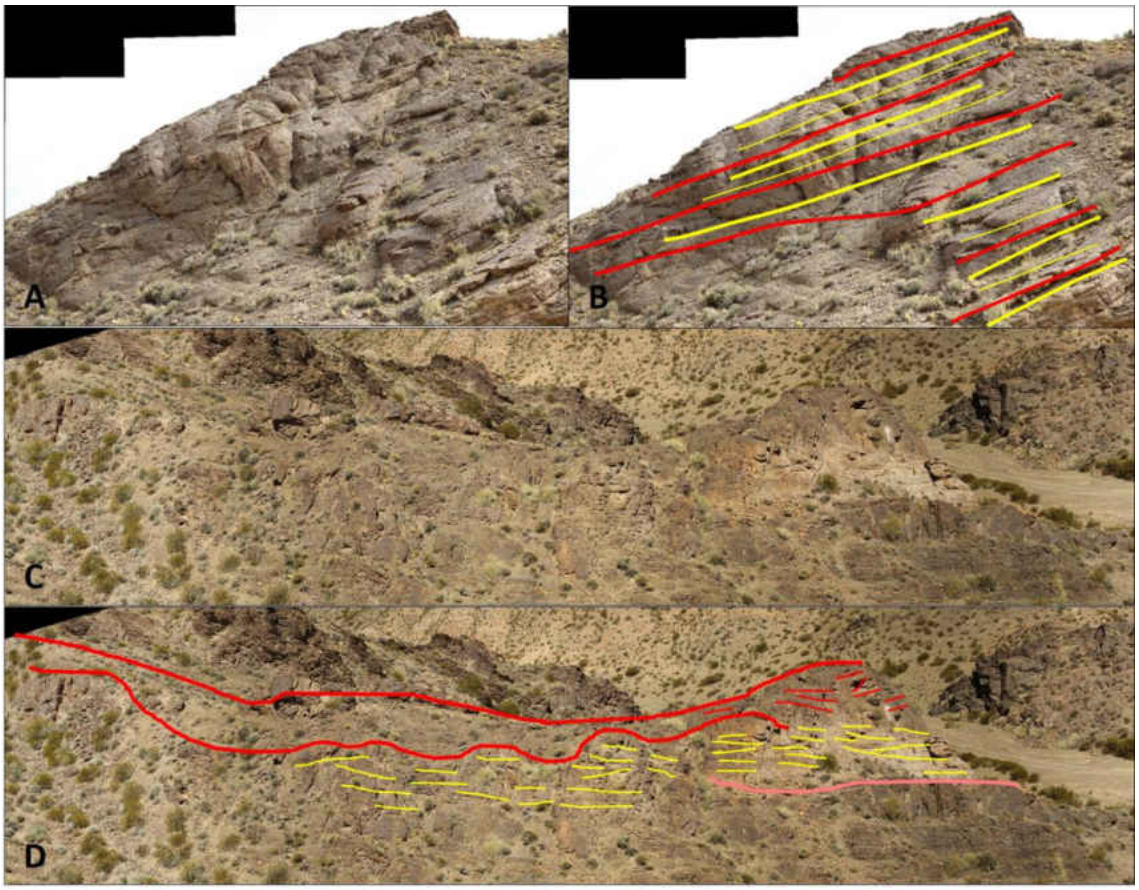

Figure 11 – Photo mosaic of the CUS sandstone and conglomerate facies association. A. Gently dipping clinoforms of coarsening upward sandstone to conglomerate. Individual clinoforms are 1-2 m thick. B. Annotated photo of Figure 11A. Red lines are conglomerate beds and yellow are sandstone beds. C. Panorama of wave rippled and cross-bedded sandstone that is eroded and grades into conglomerate. The conglomerate body (red outline) is approximately 100 m wide. D. Annotated photo of Figure 11C.

4.6.1. CUS Sandstone and Conglomerate Facies Description

The CUS sandstone and conglomerate (CS) facies occur as laterally extensive sheet geometry bodies (Fig. 11). Basal contacts are erosional, and internal structures include coarsening upward packages of sandstone to conglomerate and imbricated clasts (Fig. 11A and 11B). Upper contacts are commonly erosional or gradational. Conglomerate bedding varies from 4 cm thick beds up to 5 m thick massively bedded units, and conglomerate clasts range in size from 0.04 to 26 cm, while the average size is 5 cm in diameter. Associated sandstone are

medium- to coarse-grained, bed thicknesses range from 1 to 50 cm, and are often structureless, however rare planar cross-bedding and bioturbation were observed.

4.6.2. CUS Sandstone and Conglomerate Facies Interpretation

The CUS sandstone and conglomerate facies represents a prograding or aggrading deltaic environment. In the upper member, CUS sandstone and conglomerate occur as the upper portion of parasequences (560-570 m; 595-605 m). The conglomerate and sandstone contain imbricated clasts, gently dipping forsets, and erode into underlying shoreface deposits, which are interpreted to represent a prograding delta front. The erosional base of these deposits may represent that they are part of a forced regression during falling base level conditions.

4.7. Deformed Sandstone Facies

Deformed sandstone facies occur above and occasionally interlayered with diamictite intervals in the lower diamictite-bearing member (0-22 m; 410-430 m) as well along the lower boundary of the upper member (535 m).

4.7.1. Deformed Sandstone Facies Description

The deformed sandstone (Sd) facies consists of sub-rounded, fine- to medium-grained, muddy or clean sandstone, with rare occurrences of interbedded diamictite, coarse-grained sandstone, and mudstone (Fig. 12). Basal contacts are sharp or deformational, with upper gradational contacts with overlying units (Fig. 12A). Where sandstone beds are deformed, sheath folds, slumps, glide planes, water escape pipes, sediment loading, and sand boudinage structures are typical (Fig. 12B - 12E). Boudinage structures occur at the base of sandstone

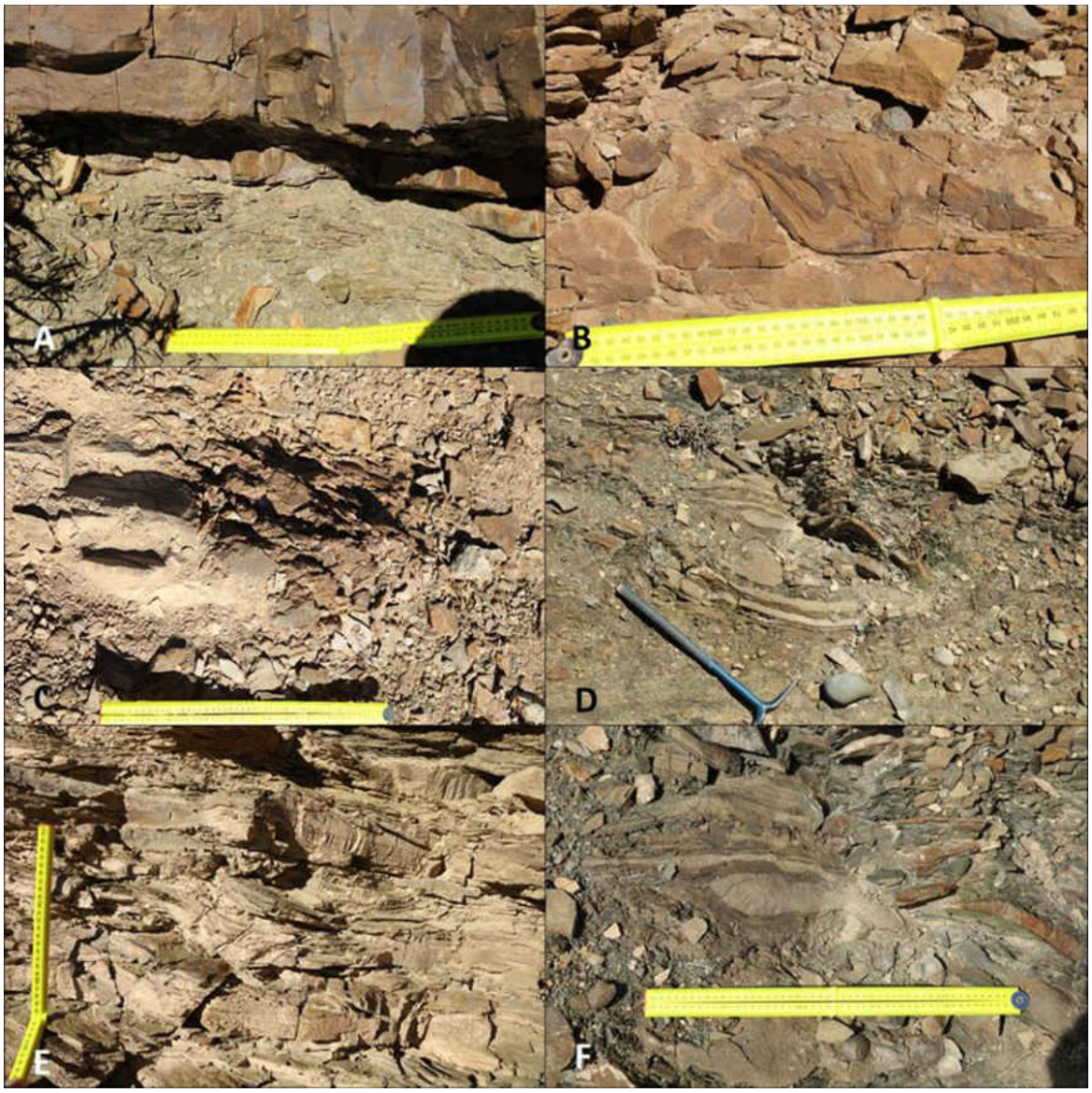

Figure 12 – Photo mosaic of the deformed sandstone facies association. A. Sandstone loading over mudstone. Ruler (50 cm) for scale. B. Load and flame deformation of sandstone. Ruler (30 cm) for scale C. Folded sandstone with ruler (50 cm) for scale. D. Cross-sectional view of sheath fold encapsulating sandstone and mudstone. Hoe pick (1 m) for scale E. Water escape structures in sandstone with ruler (25 cm) for scale F. Sandstone boudinage structures beneath pebbly mudstone and diamictite. Ruler (50 cm) for scale.

bodies, and the deformation may be localized to the basal regions and not show elsewhere in the same sandstone body (Fig. 12F). Normally graded sandstones with sole marks also occur, often associated with the rippled sandstone facies. Bedding ranges from 2 cm to 2 m thick beds, and interbedded sandstones and shale can occur as m-scale sheath fold.

4.7.2. Deformed Sandstone Facies Interpretation

The deformed sandstone facies exhibit a diverse array of deformational sedimentary structures representing subaqueous mass-transport and turbidite deposits. Where mudstone is dominate, fine sands were likely deposited by rain-out from meltwater plumes or as low-density turbid underflows. Deformation structures were generated by slope failure, allowing a body of material to slide down a paleoslope forming glide planes, sheath folds, and contorting underlying beds. Sand boudins formed at the base of sandstone-dominate bodies overlying muddy material, where the sand masses are stretched and sheared along a glide plane due to rheological contrasts between the sand and the surrounding mud (Woodcock, 1976).

4.8. Pebbly Mudstone Facies

Pebbly mudstone facies occur above the lowermost diamictite interval (50-105 m), and is interlayered within the uppermost diamictite (~430 m) in the lower member of the Ansilta.

4.8.1. Pebbly Mudstone Facies Description

The pebbly mudstone (Mp) facies consists of claystone and siltstone containing outsized clasts, with rare occurrences of fine- and medium-grained sandstone (Fig. 13). These fall under the mudstone with dispersed clast category in Moncrief (1989) and Hambrey and Glasser (2003) classification scheme and contain less than 1% gravel (>2mm in grain size) in the whole sediment. Clasts vary from 0.02 to 24 cm in diameter, with pebble-sized clasts (0.04-6.4 cm) being most prominent (Fig. 13A). Clast compositions are predominately sandstone and vein quartz, however granitic clasts become more abundant further up section. Faint striations are visible on approximately 25% of clasts, with rare occurrences of faceted and polished clasts. Clasts within pebbly mudstone facies do not show a preferred orientation, however the long

axes of some clasts are orientated at high angles to bedding and penetrate or down-warp underlying laminations (Fig. 13B). Occasional deformation structures are present, represented by sheath folds and loading, and claystone and siltstone may be rhythmically bedded. Claystone and siltstone are often fissile or splintery textured as a result of strata depressurization due to Cenozoic uplift, dark gray in color, and bedding ranges from thinly laminated (1-3 mm) to massively bedded units.

Pods composed of diamictite occur within the pebbly mudstone overlying the basal diamictite interval (Fig. 13C). The pods are lens-shaped and have a maximum diameter of 3m. The pods occur throughout 13 m of section, and are surrounded by mudstone containing outsized clasts. The pods have sharp basal contacts and appear to deform surrounding mudstone along the base and sides of the pod. Thin discontinuous lenses, clumps, ribbons of normally graded sands are also observed within this facies (Fig. 13D).

4.8.2. Pebbly Mudstone Facies Interpretation

The pebbly mudstone represent a combination of distal iceberg rain-out and suspension settling processes. When rhythmic bedded claystone and siltstone occurs, deposition was from suspension settling of fine-grained particles or as distally-deposited turbidity currents (Cowan et al., 1990). Clast lithologies of sandstone, quartz, and granite were likely derived from Protoprecordilleran basement rocks (Ramos, 1988; Azcuy, 1999). Folds, slumps, and slides formed from water-saturated material of assorted grain sizes as result of high sedimentation rates, failure of the substrate and downslope resedimentation of the material. The combination of pebbles and mudstone formed via multiple glacimarine processes synchronously, with the clay and silt-sized particles settling from suspension while the clasts were derived from icebergs

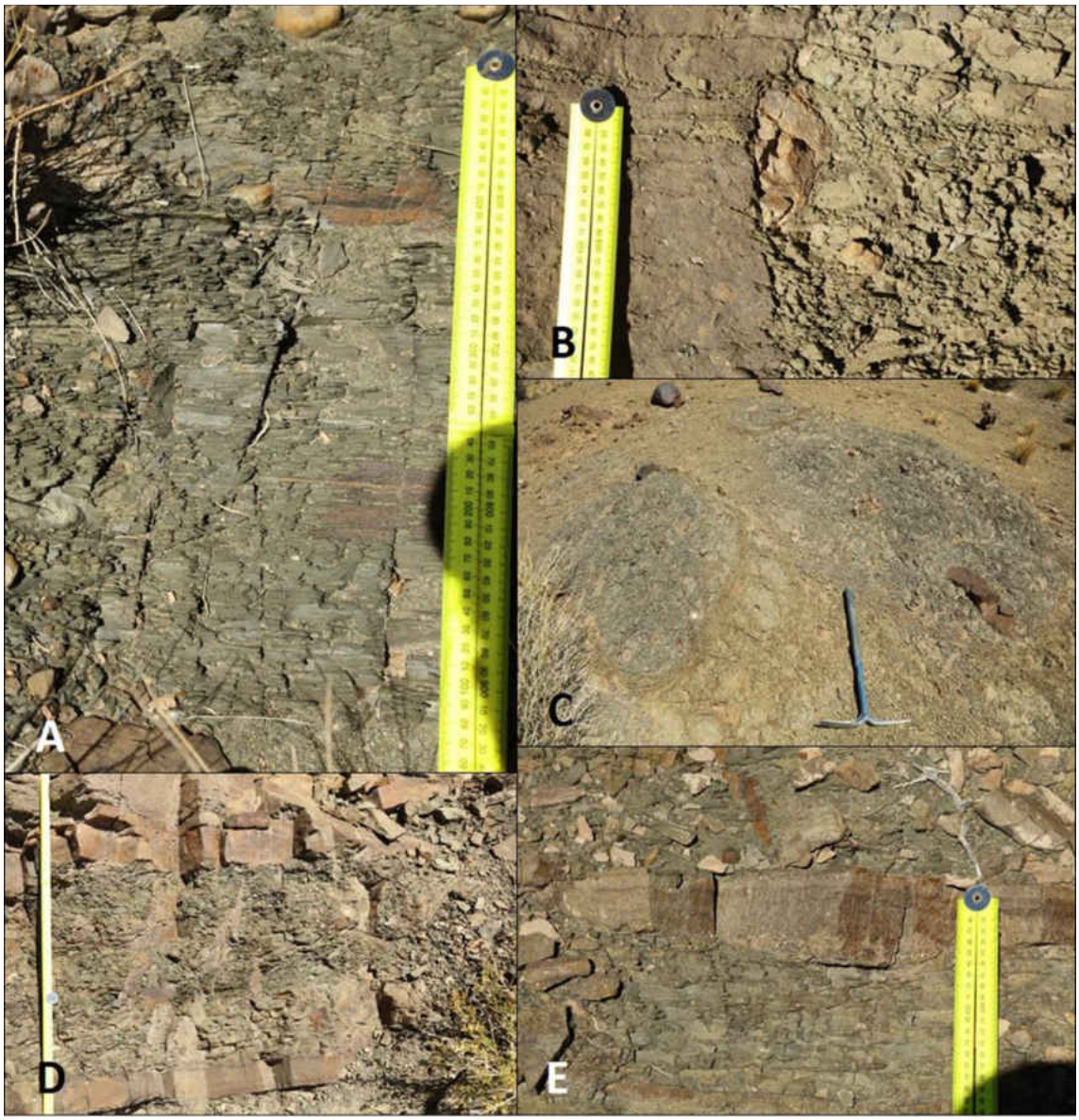

Figure 13 – Photo mosaic of the pebbly mudstone facies association. A. Outsized clasts within laminated mudstone. Ruler (50 cm) for scale. B. Outsized clast penetrating laminations. Clast is 8 cm in length C. Lens-shaped pods of diamictite within a thick interval of pebbly mudstone. Hoe pick (1 m) for scale. D. Layer of pebbly mudstone with interlayered sandstone lenses near the top of glacially influenced interval. Ruler (75 cm) for scale. E. Ribbon of sandstone showing normal grading within pebbly mudstone. Ruler (25 cm) for scale.

that calved from a distant tidewater glacier (cf. López-Gamundí, 1997; Powell and Domack, 2002). Likewise, diamictite pods were deposited from icebergs rolling and melt-out of ice-bound sediments, termed iceberg dump structures (Thomas and Connell, 1985). The sediments would sort according to their size and shape attributed to different settling velocities as they

traversed through the water column and warp underlying strata due to the weight of the overlying sediments (Thomas and Connell, 1985; Fig. 13E).

4.9. Laminated Mudstone Facies

The laminated mudstone facies occurs throughout the measured section, with sizeable outcrops located between the lowermost and middle diamictite-bearing intervals (22-50 m; 105-160 m), above the uppermost diamictite interval (435-540 m) signifying the end of glaciation, and as marine flooding surfaces that separate parasequences within the nearshore and fluvial sands at the top of the measured section.

4.9.1. Laminated Mudstone Facies Description

The laminated mudstone (Ms) facies consists of claystone and siltstone, with rare occurrences of interlayered marlstone and fine- to medium-grained sandstone (Fig. 14). Claystone and siltstone are often fissile textured, occasionally bioturbated, olive to dark gray in color, with bedding ranging from thinly laminated (1-3 mm) to massively bedded units (Fig. 14A). Marine fossils are nearly absent from this facies within the glacial interval, with only a single unidentified gastropod found within the laminated mudstone. Limonitic marls occur as thin bedded (<5cm) micritic limestone interlayered within silty shales (Fig. 14B). Fine- to medium-grained sandstone occurs as lenticular bodies, and is frequently deformed, with sand load structures being dominate when overlying mudstone (Fig. 14C & 14D). Lenticular sandstone bodies are less than 2 m thick, and have a width of between 5-25 m. Bedding ranges from 0.5-4 cm thick, and internal structures include rare current ripples, and may display mud drapes or normal grading. Isolated bodies of sandstone within mudstone intervals often show the shales onlapping onto sands.

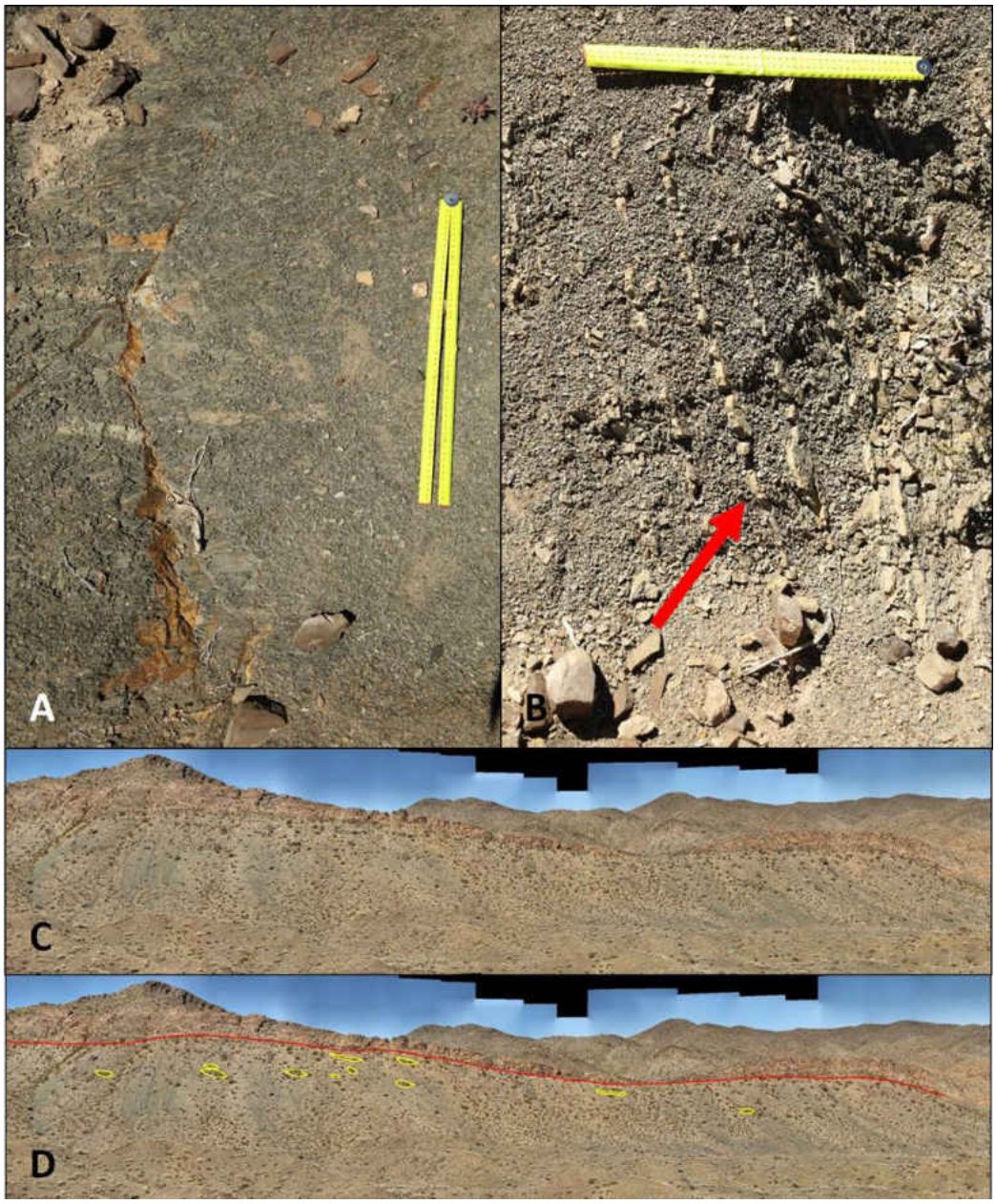

Figure 14 – Photo mosaic of the laminated mudstone facies association. A. Laminated, occasionally massive, mudstone. B. Marl in mudstone (red arrow). Ruler (50 cm) for scale. C. Thick interval (100 m)of mudstone above the last glacial signature, with isolated sandstone lenses. D. Annotated photo of Figure 14C.

4.9.2. Laminated Mudstone Facies Interpretation

The laminated mudstone facies show no glacial indicators, even though it may overlie glacially-influenced facies. Due to the absences of outsized clasts and other glacial indicators, this suggests that the facies was deposited in quiet waters without the influence of glaciers,

possibly due to a loss of glacier or that they retreated onto land, or were isolated from direct influences of glaciers and floating ice caused by a corralling of icebergs in a sub-basin or paleofjord. The primary process of deposition of laminated claystone and siltstone was hemipelagic sedimentation via suspension settling. The presence of marlstone within glacially influenced systems has been used by Argentine researchers to suggest clastic-starved conditions, allowing diagenetic carbonate production to occur (López-Gamundí, 1997).

Where mudstone is dominate, fine- to medium-grained sands indicate underflow deposition or distal turbidites. Plane laminated and current rippled sands that grade normally into laminated siltstone and shales represent Bouma beds (T_d & T_e) deposited by turbidity currents. Turbidite muds are often weakly stratified to massive when compared to massively bedded muds deposited by hemipelagic sedimentation (cf. Powell and Cooper, 2002). The sandstone bodies near the top of the lower member (520-540 m) represent mass transport deposits, and are likely distal signatures associated with the progradation of the overlying sandstone.

5. Glacial Sequence Stratigraphy

Sequence stratigraphy concepts have been used by researchers and exploration geologists as a means of classifying, correlating, and mapping sedimentary rocks in a chronostratigraphic framework to better understand the controlling depositional factors that influence sequence sedimentation, such as: eustatic and local sea-level changes, subsidence/accommodation, sediment supply, and climate (Handford and Loucks, 1993; Posamentier and Allen, 1999; Powell and Cooper, 2002; Catuneanu et al., 2009). Over the past fifty years, sequence stratigraphy has been used extensively by the oil and gas industry understanding the geology of shallow marine depostional systems primarily from low latitude

siliciclastic and carbonate settings. However, glaciated environments are unique in the sense that facies changes may occur as a result of glacial fluctuations, and may act independently from changes in eustatic sea-level, accommodation, rates and styles of sediment delivery to the continental margin, and local tectonism (Boulton, 1990; Powell and Cooper, 2002; Isbell et al., 2003; Limarino et al., 2006). For this reason, an alternative model is required to interpret strata of this nature rather than the traditional sequence stratigraphic approach. Strata belonging to the nearshore and fluvial sequences at the top of the section are described using traditional siliciclastic systems.

5.1. Facies Succession and Motifs

Powell and Cooper (2002) and Rosenblume and Powell (2019) provide a model for modern glaciated shelf settings, with distinct glacial system tracts that are related to glacial advance and retreat signatures. Powell and Cooper define 4 different systems tracts: glacial maximum (GMaST), minimum (GMiST), advance (GAST), and retreat (GRST) systems tracts. In this scheme, systems tracts are separated by glacial bounding surfaces (GBS), which consists of glacial advance (GAS), glacial retreat (GRS), maximum retreat (MRS), and iceberg termination (ITS) surfaces. Parasequences of glacial systems often vary in composition and thickness as they transition across a shelf into a slope setting, however they are dominated by facies that represent the movement of a glacier's grounding-line rather than being solely restricted to changes in relative sea-level.

Facies successions have been established as a means of creating a hypothetical glacial advance and retreat cycle motif, which various researchers have assigned to Cenozoic glacial shelf successions in Antarctica, the Arctic, Alaska, and Greenland (Dowdeswell 1998; Fielding

et al. 2001; Naish et al. 2001; Powell and Cooper 2002; Rosenblume and Powell, 2019). These facies motifs represent an idealized glacial cycle and here, have been modified to incorporate new data collected from the Ansilta Formation for this study.

The lower portion of a hypothetical motif consists of a broad fining upwards trend from diamictite, sandstone and conglomerate, to pebbly mudstone, muddy sandstone and interstratified muds, and laminated mudstone showing a decrease in glacial signatures up section (Fielding et al., 2001; Powell and Cooper, 2002; Fig. 15). The transition from coarse- to fine-grained facies is rapid, often occurring over a 1-m-thick interval. This portion corresponds to a GAST, comprising a basal erosional surface or GAS and the deposition of diamictite. This is followed by a fining upwards interval marked by a GRS, above which encompasses a GRST. The middle interval represents a relatively ice-free open marine setting, where hemipelagic settling is the dominate mode of deposition. This interval may start with an ITS, after which sedimentation is inferred to have little to no glacial influence. The upper portion of the motif consists of coarsening upward succession from mudstone, to pebbly mudstone or clast-poor diamictite and muddy sandstone, showing an increase in glacial signatures up section which represents a glacial readvance. It should be noted that due to the erosive and dynamically complex nature of glacial environments, facies motifs will not be uniform in appearance and may be incomplete due to glacial readvances removing previously deposited material. This idealized model interpretation may work for some successions.

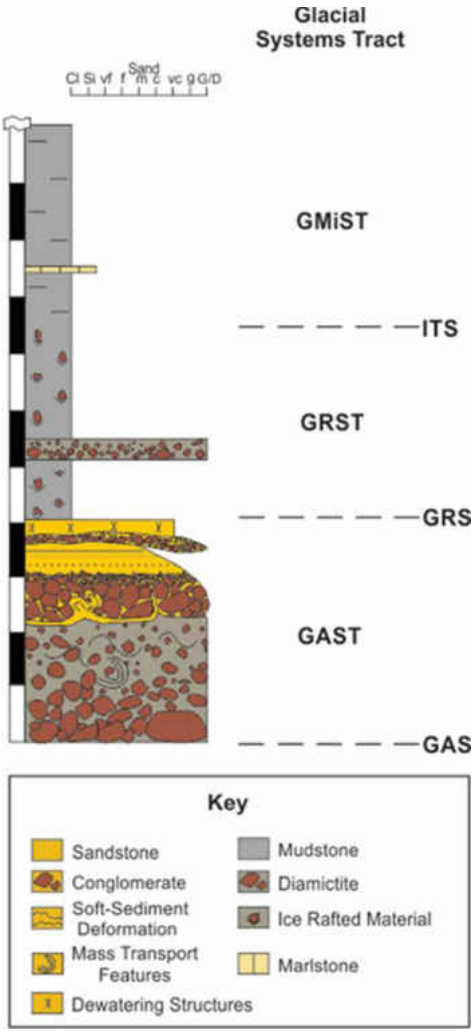

Figure 15 – Hypothetical glacial retreat motif, consisting of a broad fining upwards trend from diamictite, sandstone and conglomerate, to pebbly mudstone, to laminated mudstone with marlstone, showing a decrease in glacial signatures up section.

5.2. Facies Sequence Discussion

A facies analysis of the Ansilta Formation reveals three stages of depositional regimes for the glacial interval, recording at least five separate glacial advances, and an additional four stages in the overlying shelf, near shore, and fluvial successions which are unrelated to glacial advance and retreat cycles within the Calingasta-Uspallata Basin (Fig. 16). Stages are defined here based on similar sedimentological characteristics and facies associates that have led to an interpreted depositional environment.

Stage 1 (0-158m) consists of one complete and a partial glacimarine facies motif recording two advance and retreat cycles. It should be noted, that the unconformity between the Ordovician Basement and the Ansilta Formation does not contain evidence that glaciers overrode the study site within this basal GAST. While other studies in the region have attributed the deposition of diamictite-bearing strata to be in a fjord setting, the strata from the lower member of the Ansilta Formation was likely deposited in a basinal shelf or ramp setting (Henry et al., 2010; López-Gamundí et al., 2016). This interpretation has been established for a small area of exposure for the Ansilta Formation and is justified due to the gentle relief along the basal contact with the underlying basement, the lack of a U-shaped paleovalley or subglacial indicators, and the absence of onlapping geometries along a valley wall. Since the entirety of the Ansilta Formation was not explored during this field investigation, this interpretation may not be valid everywhere, and satellite imagery show some areas in the northeast portion of the formational outcrop belt where there is possibly significant relief along the basal unconformity. However, a basinal shelf or ramp setting is the most applicable depositional setting for strata deposited in the vicinity of the measured section. A GAS marks the lower glacial sequence boundary between Ordovician-Silurian aged slate, phyllitic sandstone, and quartz pegmatite basement and depositional Stage 1. The contact is erosional showing a change in relief of up to 5 m, and the contact was likely sub-aerially exposed and eroded at one point, however basal units of the Ansilta formation were deposited in a sub-aqueous setting. Therefore, this boundary is not interpreted to represent a glacial erosional surface, which are often missing if the glacier does not advance across the shelf (Fig. 17). Above the GAS is a GAST, represented by diamictite, conglomerate, and sandstone with abundant slump and turbid underflow deposits present throughout (0-22 m). Striated clasts and dropstones in this basal stage offer the first

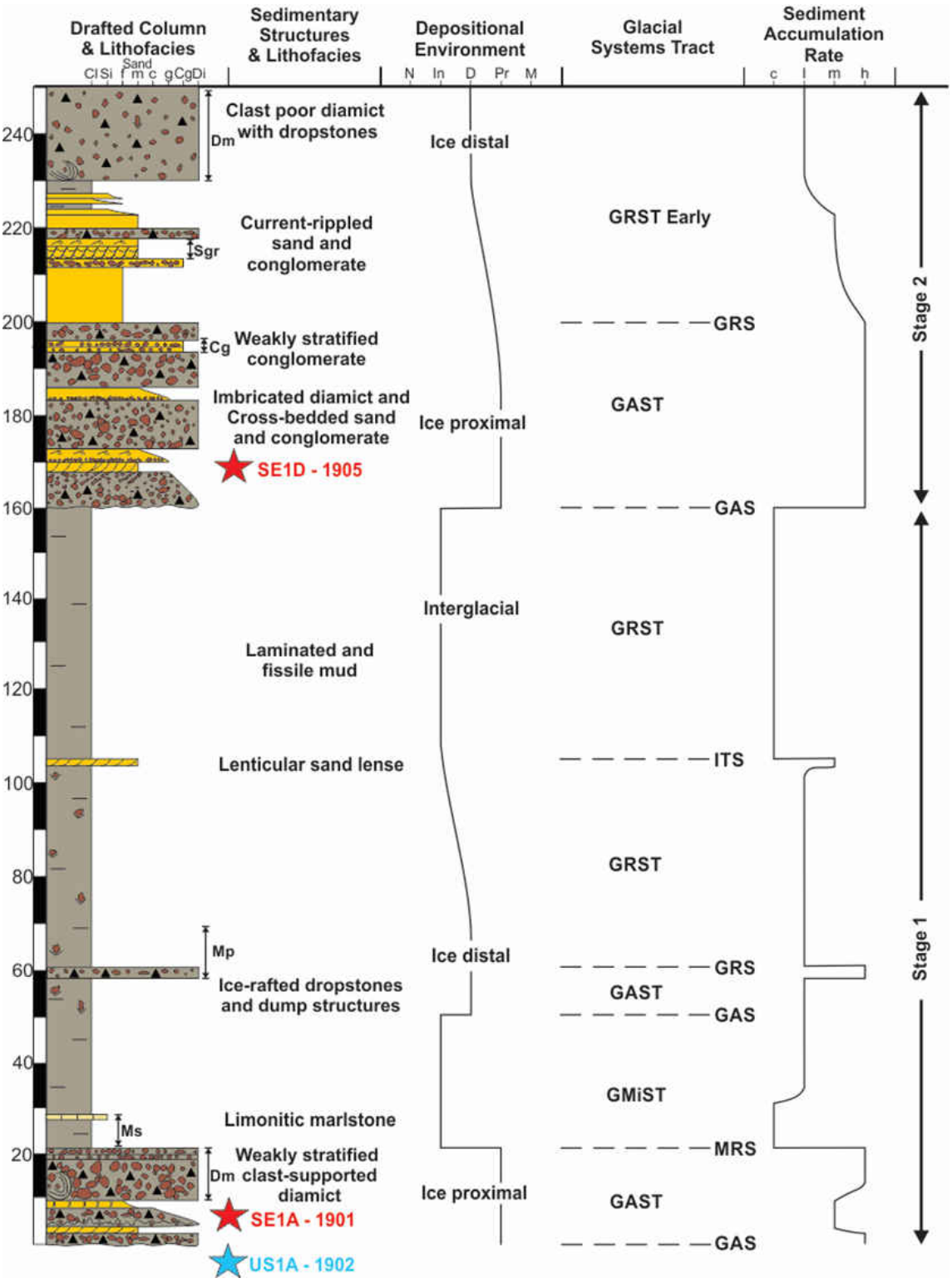

Figure 16 – Stratigraphic column, system tracts, and interpreted depositional processes for the Ansilta Formation. Red stars mark sandstone horizons sampled for the detrital zircon analysis. Symbols across the top for depositional environments include: N = non-glacial; In = interglacial; D = ice distal; Pr = Ice proximal; M = morainal bank. Sediment accumulation rate symbols include: c = condensed; l = low; m = medium; h = high.

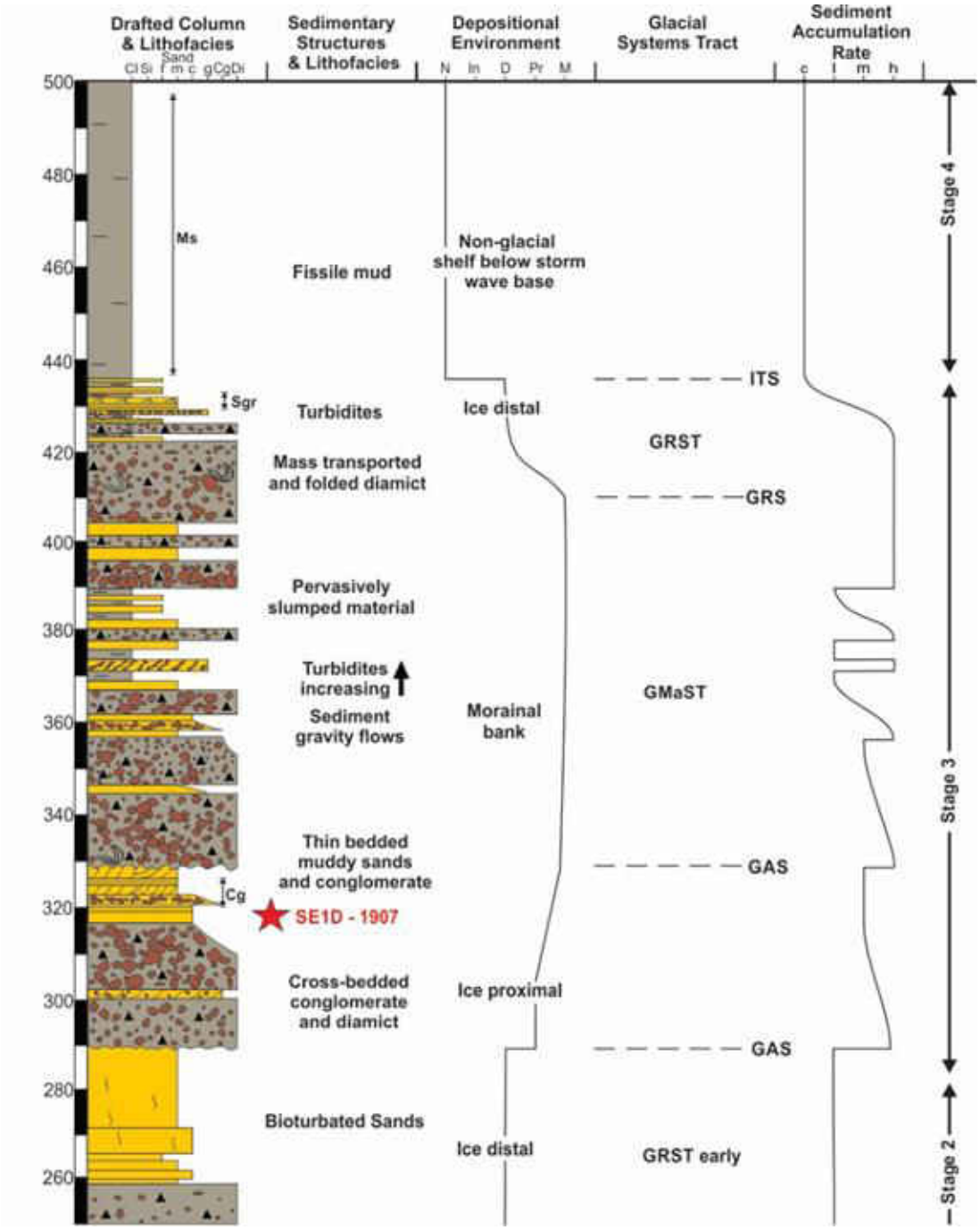

Figure 16 – continued.

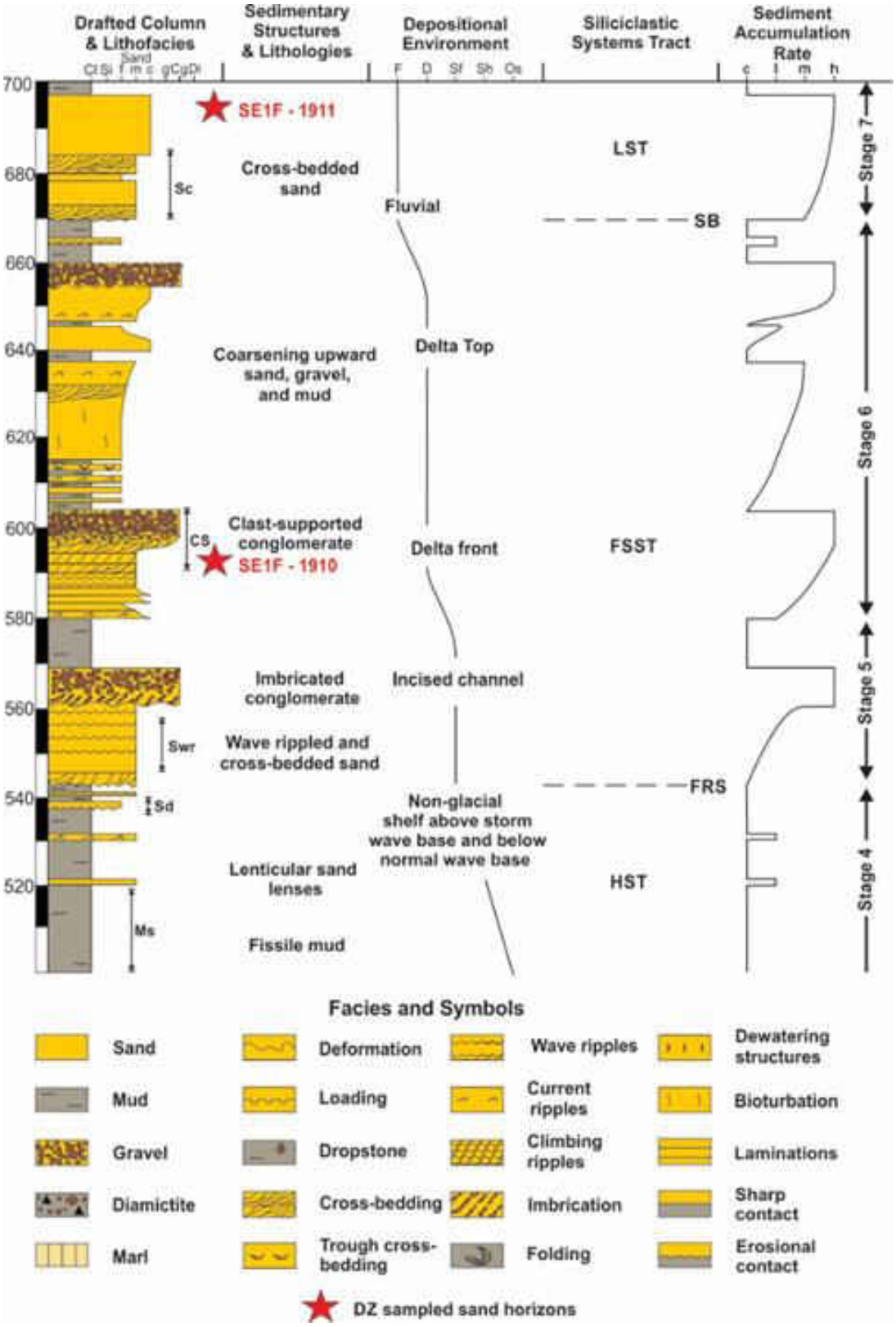

Figure 16 – continued. Symbols for depositional environments include: F = fluvial; D = deltaic; Sf = shoreface; Sh = shelf; Os = offshore.

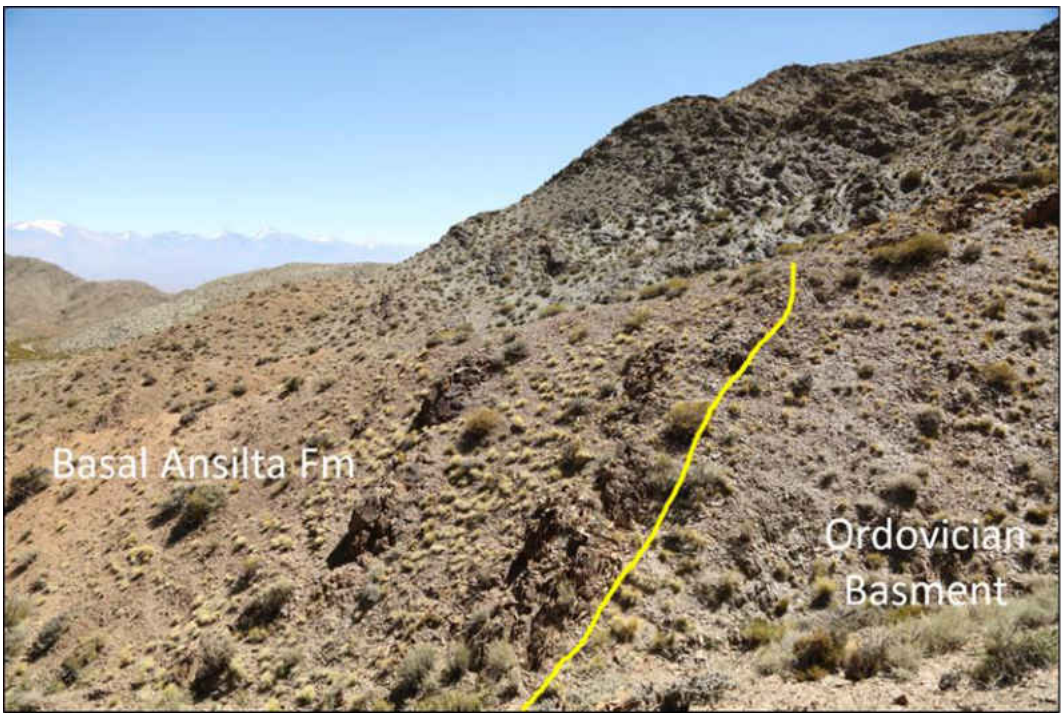

Figure 17 – Basal erosional contact between the Ordovician strata and the Ansilta Formation.

evidence of nearby glaciers. These mass transport and sediment gravity flow deposits wedge out laterally over several meters and often downlap underlying strata, suggesting progradation of a morainal bank front or a glacially influenced subaqueous fan in a shelf setting. This diamictite-bearing interval is capped by a MRS, above which glacially influenced signatures are absent. Directly above the MRS is the GMiST, marked by the presence of laminated, mudstone and limonitic marlstone. This interval (22-52 m) is interpreted as a glacial minimum interval, which would explain the lack of coarse-grained sediments and the occurrence of marl deposition during an interval when glaciers were absent (López-Gamundí, 1997; Powell and Cooper, 2002; Henry et al., 2010). At 52 m, another GAS is observed and glacier influence resumes (GAST), this time characterized by mudstone containing outsized clasts. Clasts are occasionally striated and penetrate laminations at high angles suggesting deposition from ice rafted debris. Dump structures are present at 60 m, suggesting distally sourced material carried by iceberg-rafting

and deposited in a deep-water, open ocean setting. Above this pod of diamictite is a GRS and ensuing early GRST comprising pebbly mudstone, and this facies dominates until 108 m, where a lenticular sand sheet marks an ITS. This sand body is approximately 70 m wide and 1 m thick at its axis, and likely represents a distal underflow deposit. This sand body is capped by laminated mudstone without outsized clasts, signifying a GMiST from 109-158 m. This interval marks the end of stage 1.

Stage 2 (158-290 m) begins with a GAS represented by an erosional surface beneath a debris flow of a thick diamictite-bearing interval with striated and faceted clasts incising underlying mudstone. The GAS consists of a basal grooved surface showing sole marks. High density flow deposits, slides, and slumps are present in this section, evident from sole marks and plough marks as well as inverse and normal grading (Sobiesiak et al., 2018). The conglomerate and sandstone become complexly interlayered starting at 170 m, often fining and pinching out laterally into diamictite over several meters. This suggests channelized confined and levee/splay unconfined flows or the compensational stacking of sheet flows in an ice-contact fan, due to the fining of material as layers pinch out, erosional and sharp contacts, and the tabular nature of channel deposits (Deptuck and Sylvester, 2018). The channels cut into diamictite levees, with conglomerate occupying the channel axis and sandstone filling the channels and over flow splays. Due to the similarity with those of stage 1, these strata were likely deposited as an ice-contact fan incising a morainal bank front setting, with overbank lobate deposits. The diamictite interval is topped by a GRS at 200 m, and glacial signatures represented by diamictites and striated clasts decrease gradually throughout the rest of stage 2, indicating an early GRST. A diamictite, gravel, and sand-filled channel system is observed from 211-224 m, consisting of clast-poor diamictite, trough cross-bedded sandstone, and pebble conglomerates (Fig. 18).

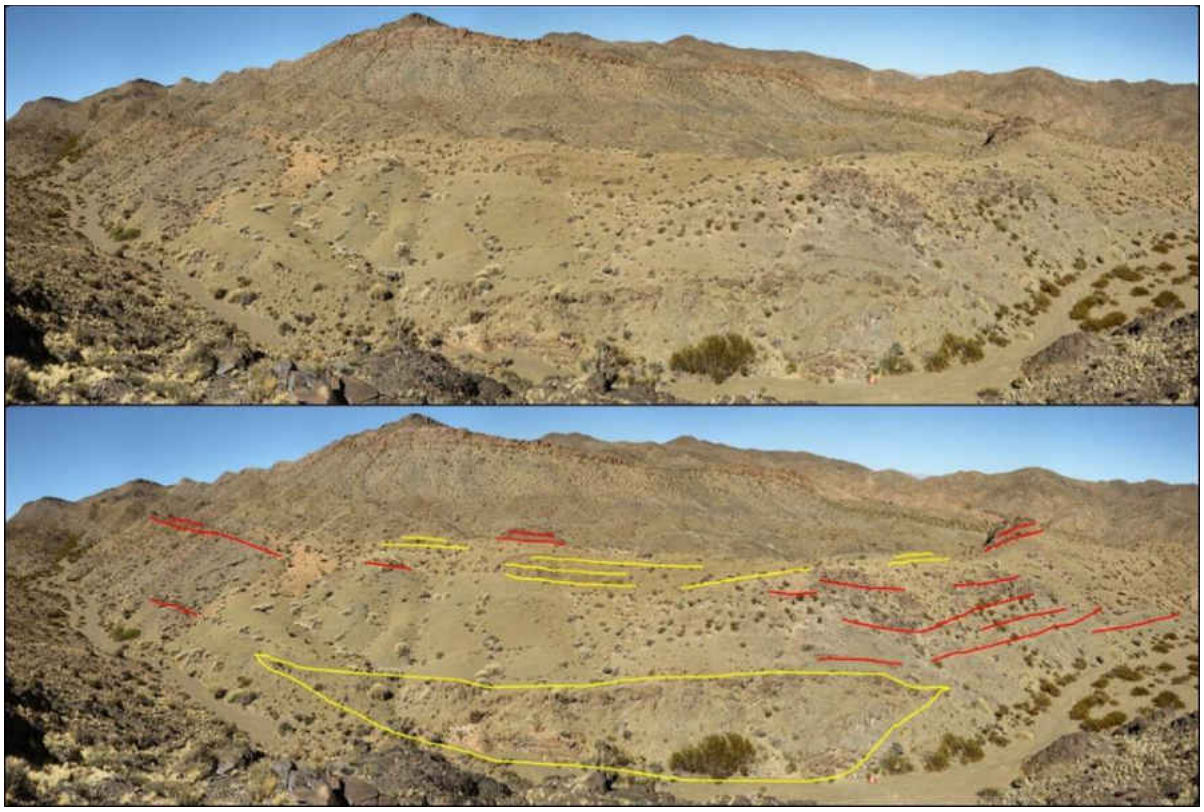

Figure 18 – Subaqueous channel complex (150 m) incising diamictite, transitioning upward into discontinuous bodies of interfingered massive sandstone (yellow lines) and weakly bedded clast-poor diamictite (red lines).

Lunate current and climbing ripples are present, suggesting unidirectional flow likely within an unconfined system as sedimentary structures indicate that flow was slowing down in the direction of the flow. Sand layers are not laterally extensive and often interfinger with adjacent units of diamictite; this relationship of layers suggests progradation, potentially laterally, as sand-laden overflows top the channel margins. Due to the geometry of the channel body, having a width-depth ration of 12.5: 1, and the nature of sedimentary structures and characteristics, this channel system is interpreted to have incised into the underlying morainal bank lobate fan deposit and served as a conduit for transporting glacially derived material to deeper water ice distal settings. The channel system passes upward into clast-poor diamictite with abundant dropstones and discontinuous bodies of folded diamictite, interpreted as iceberg rafted debris and slides and slumps. This diamictite is different from those seen elsewhere in the

section due to the lack of any apparent bedding and the higher mud matrix to clast ratio. This interval, which runs from 230-259 m, shows a decrease in the number of clasts with increasing elevation, indicating a decline in the source of clast through time, suggesting waning glacial influence. These strata were likely deposited by a combination of iceberg rain-out and suspension settling from a meltwater plume. Stage 2 is capped by alternating layers of fine- to coarse-grained muddy bioturbated sandstone from 259-290 m.

Depositional Stage 3 (290-437 m) begins with a GAS, above which a thick diamictite interval with striated and faceted clasts, containing interbedded conglomerate, sandstone, and mudstone. This erosional surface is beneath a debris flow deposit of diamictite, representing a resurgence in glacial activity. A fining upward trend is observed from 290-330 m as weakly bedded diamictite passes up into thinly bedded, cross-bedded muddy sandstone and pebble conglomerate that is topped with an erosional GAS. There is a temptation to interpret this interval as a GRST, however the presence of thin cross-bedded sands without bioturbation suggests that glaciation is still widespread. Instead, this sand body may represent a grounding-line fan system being deposited by meltwater discharge from the base of a glacier, and the superimposed GAS may only indicate a minor glacial surge in an overall advance or retreat cycle. This contact is erosional in some places, however in other localities the sand and overlying diamictite interfinger and form tangential forests, which provide another possible indicator for a grounding-line fan system. Above this GAS is another thick interval of diamictite and sandstone, containing abundant evidence of sediment gravity flows, glide planes, fold noses, and turbidites that increase in quantity up section. Thin lenses of interlayered deformed sandstone within the diamictite are likely slumped sands, shed from the bed load material as it moved down a slope. From 370-390 m, alternating thin layers of conglomerate, sandstone, and

shale are observed, representing a debrite that formed as a result of substrate failure and the reworking of material on a scale of 1cm to 1m thick. Clasts protrude into the sand layers, indicating cohesive flow and grain to grain collision, the sand being shed from the coarse material and the fine-grained particles settling from suspension. The top of the glacially influenced portion of the lower member consists of diamictite becoming clast poor with elevation and a complex assemblage of pervasively reworked material. One occurrence of a 4-m-thick interval resulting from a block of material sliding or ploughing down a slope consists of a basal glide plane, and the block of material contains sand boudins and sheath folds, indicating that abundant substrate failure manifested by the slumping of material and substrate shearing was happening before and at the time of the emplacement of this sediment block. Above this from 423-437 m are massive sands, occasionally laminated, and rare incidences of laminated sands capped by a single rippled bedform, then normally grading into silt and mudstone. These assemblages are interpreted as underflows deposited by turbidity currents, the massive sand (Bouma A; T_A) beds settled from turbulent suspension, laminated sand (Bouma B; T_b) beds representing upper flow regime plane bed traction, rippled sand (Bouma C; T_c) beds signifying lower flow regime traction, and the silt and mudstone (Bouma D; T_D, Bouma E; T_E) deposited as suspension fallout (Shanmugam, 1997). All Bouma sequence beds may or may not be present in a single succession, and the occurrence of outsized clasts present in all the different layers indicates a glacial ice front was releasing icebergs and ice rafted debris into the basin. The overall thickness (~140 m) and the prolific occurrence of folds and slumps throughout this interval are key indicators that suggests high sedimentation rates and a proximal glacial setting, perhaps as a morainal bank core or a trough mouth fan situated in an upper slope setting (Vorren and Laberg, 1997; Powell and Cooper, 2002). Due to the previous interpretation of the

underlying diamictite-bearing stages, as well as the observed characteristics and thickness of these deposits, a moranial bank core is the assumed depositional environment.

The glacial interval is capped by depositional Stage 4 (437- 542 m), consisting of a thick interval of massive and laminated shales deposited in deep water by suspension settling in the absence of glaciers. The mudstones show signs of apparent slumping, indicating there was some slope to the depositional surface and may have formed as a result of the overlying prograding shelf shedding sediment downslope into deeper water. This interval marks a HST and the abrupt termination of coarse clastics being delivered to the system, which can be interpreted by some combination of the following: glaciers receded from an open ocean, wet-based glacier retreating on to land, or an increase in accommodation space. Glaciers likely retreated out of a deeper marine setting, which resulted in the deposition of finer-grained material. This increase in accommodation space appears to have happened synchronously with the final glacial retreat and subsequent deglaciation of the Protoprecordillera, as any evidence/indicators of glacial activity disappears. The top of Stage 4 comprises several thin lenses (<1 m) of sandstone, which show straight crested current ripples as well as sand loading and mud drapes, while shales onlap onto sand bodies. The sands were deposited as distal underflows in a shallow marine shelf environment above storm wave base and below normal wave base, likely representing the onset of forced regression with the prograding shelf sands at the edge of a prograding shelf platform failing and sliding down the slope.

The base of Stage 5 (542-580 m) marks the boundary between the upper and lower members of the Ansilta Formation, as well as a major unconformity and a transition from shelf sedimentation to a shallow water, wave influenced setting. The unconformity is an erosional contact with occasional sediment load structures, and due to contrast of depositional settings

from a shallow marine shelf to a shoreface setting, the contact is interpreted to represent a forced regression surface (FRS). This contact is also a sequence boundary (SB) due to the occurrence of normal wave base deposits overlying offshore or deeper water deposits without a transition between, and was caused by a sudden and substantial drop in relative base level. This interval includes an early FSST consisting of lunate current ripples superimposed by wave ripples, and higher up in the shoreface succession these ripples are occasionally planed off. Crinkled textures are observed within the troughs of the planed off ripples, and are interpreted to represent cyanobacteria biomats (Schieber, 1999). The crinkled textures coupled with the flat-topped ripples suggest very shallow water, probably several cm- deep. This sand body coarsens upward into a cobble conglomerate, which is not laterally persistent and contains imbricated clasts, likely representing a coarse lag deposit from a prograding coarse-grained fan delta due to the wedge- and lenticular-shaped geometry of laterally discontinuous conglomerate bodies. Some clasts within the conglomerates bear very faint striations, and may have been sourced from distal glacial outwash or reworked glacial deposits to the east. This interval is capped by a flooding surface consisting of silty mudstone.

Stage 6 (580-670 m), consists of aggradationally stacked, coarsening upward mudstone-sandstone-conglomerate parasequences bounded by flooding surfaces deposited in a shoreface setting (Fig. 19). The slight thinning of successive parasequences upward suggest that the rate of sea-level rise waned with time (Mitchum and Van Wagoner, 1991; Hampson and Storms, 2003). From 590-607 m, bioturbated and cross-bedded, coarse-grained sandstones transitions upward into a massively bedded, sandy, cobble conglomerate that in places interfingers and wedges out into adjacent medium- to coarse-grained sandstone and in others downlap onto

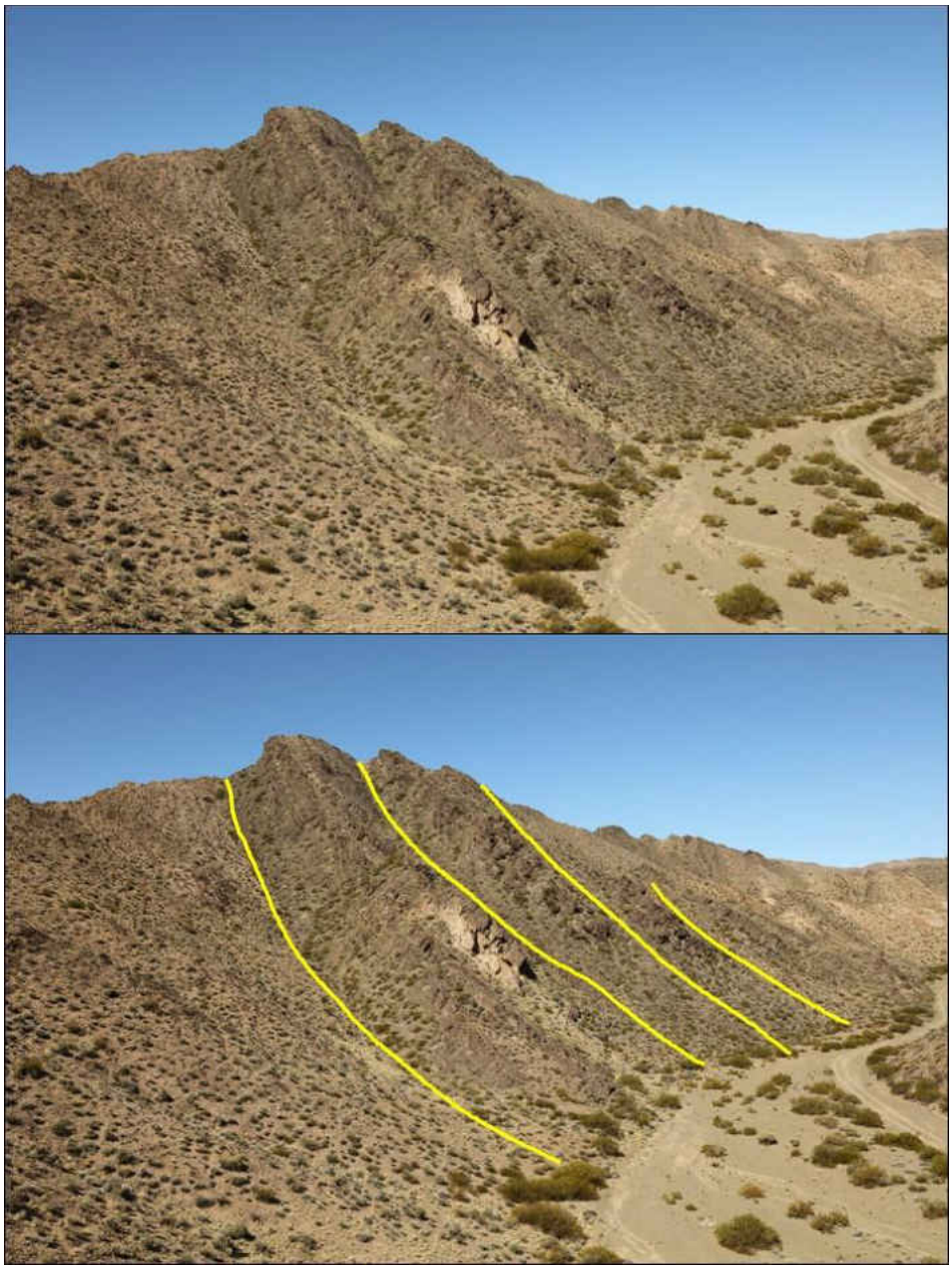

Figure 19 – Stacked parasequences of shallow marine sandstones and mudstones from the upper member of the Ansilta formation (~100 m thick). Yellow lines are flooding surfaces.

relief of an erosional surface. This interval is interpreted to represent a prograding delta front or an incised distributary channel in a delta top setting, which was eroded into into underling strata due to a sudden high flow regime surge, perhaps caused from a significant onshore flooding event or the emptying of an embayed body of water. Above this interval is another flooding

surface overlain by a coarsening upward succession with alternating layers of medium-grained, muddy sands and shale (607-637 m), bedding varying in thickness from 1 to 8cm. Trough cross-bedding, rib and furrows, current ripples, and flaser to wavy laminations provide clues as to the depositional setting, which was influenced by current, wave, and tidal influences. This succession indicates a lateral or retrogradational migration of the delta front to a distal delta front or offshore transition setting, which was followed by a readvance of the delta front. Overlying strata from 637-660 m show another flooding surface and another overall coarsening upward trend of medium- to coarse-grained sandstone, conglomerate, and interlayered shale. The sandstone initially transitions from thick bedded, burrowed, medium-grained muddy sandstone with occasional planar laminations to coarse-grained mature sandstones becoming thin bedded with trough cross-beds. From 637 to 646 m, a 5m thick body of medium-grained sand fines upward into fine-grained sandstone, and capped by shale. The upper shale is topped (646-660 m) by a coarsening upward succession of medium-grained sandstone to clast-supported sandy pebble and gravel conglomerate. The basal contact of the conglomerate is erosive and interlayered sands grade laterally into conglomerate. Sediments fine in the direction of flow as indicated by paleo current structures and grain dispersal patterns, representing a change from wave to current dominated action. The depositional environment for these strata is complex, and likely serves as a transitional assemblage from a delta top to a braided stream on a coastal plain setting due to the occurrence of CUS sandstone and conglomerate being overlain by channelized cross-bedded sandstone (Fig. 20). Overlying strata from 660-670 m represent coastal plain sandstone and mudstones, which contain an abundant of wood and organic fragments however no coal seams were identified in the section.

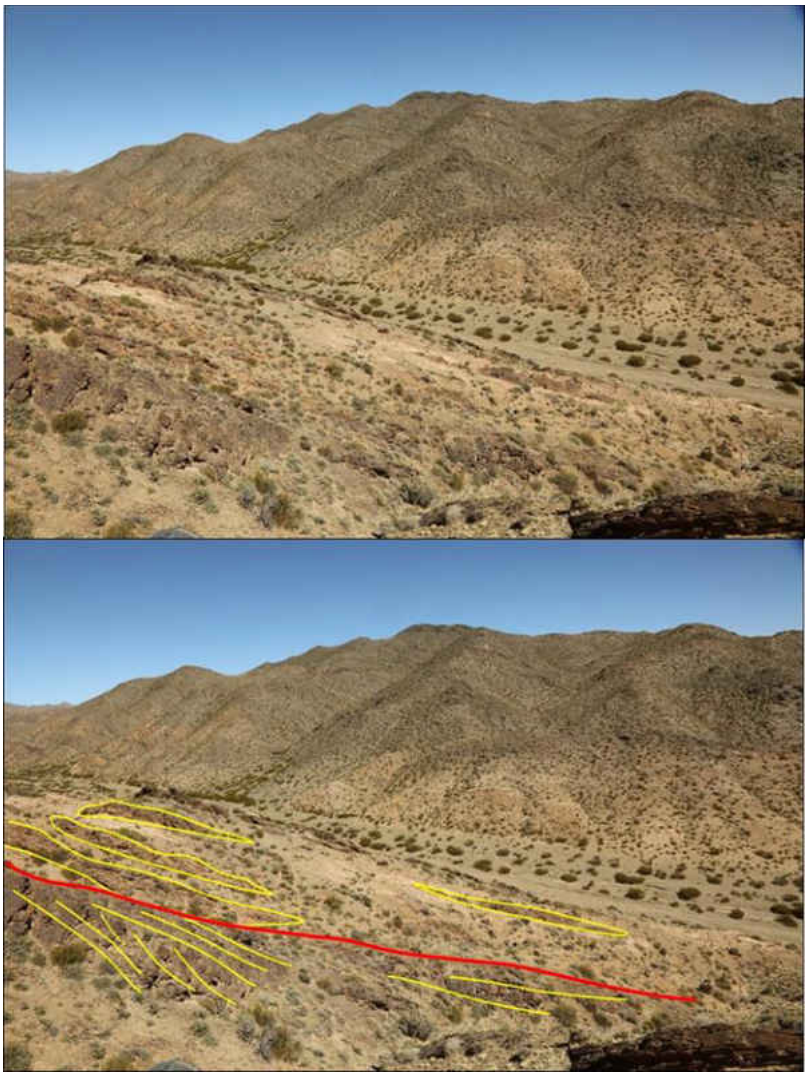

Figure 20 – Transition from deltaic marine to fluvial deposition (30 m), represented by the red line. Below the boundary are CUS sandstones and conglomerates (yellow lines), interpreted to represent a delta top environment. Above the boundary are channelized cross-bedded conglomerates and sandstones (outlined in yellow), interpreted as a braided stream environment.

Stage 7 (670-695m) is the final depositional phase in the measured section, and consists of cross-bedded medium- to coarse-grained sandstone with dispersed clasts. The base of this stage marks an unconformable boundary, above which are LST sands deposited by fluvial processes in contrast to the wave dominated structures observed below this boundary. Large downstream accreting multi-storey sand bars are identified throughout this interval, likely

representing a braided stream environment. This stage is capped by mudstones deposited on a floodplain, which marks the top of the measured section through the Ansilta formation.

6. Detrital Zircon Geochronological Analysis

Six sand horizons were sampled and collected from various stages throughout the sequence for detrital zircon U-Pb geochronology to determine sediment provenance as a way of isolating different glacial sources. One sample is from the underlying Ordovician strata, three are from the glacial interval, and two are from the overlying shallow marine and fluvial assemblages (Fig. 21).

Sample US1A 1902 (n=211) was collected from the underlying Ordovician strata and has zircons that range in age from 451-2794 Ma. The principal peak is Mesoproterozoic (1099 Ma), with a lesser peak of Ordovician ages (470 Ma). Famatinian-aged (470-450 Ma) granitic intrusions in the Sierra de Valle Fértil, Mesoproterozoic-aged 'Grenvillian' basement within the Sierra de Pie del Palo, or reworking of the local basement in the Precordillera are likely source rock candidates, and thus sediment would have been derived from local sources in the eastern Precordillera margin and the Cuyania terrane (Abre et al., 2012; Thomas et al., 2015). In addition, some of this Mesoproterozoic aged material may have origins from the Grenville Province in North America since it has been proposed that the exotic Cuyania terrane was rifted from the Laurentia Craton and docked to the western margin of South America during the middle to late Ordovician (Ramos, 2004; Naipauer et al., 2010).

The age spectra for sample SE1A 1901 (n=101), collected from sands in depositional stage 1 near the basal contact of the Ansilta, ranges from 321-2043 Ma. Age peaks are 1170,

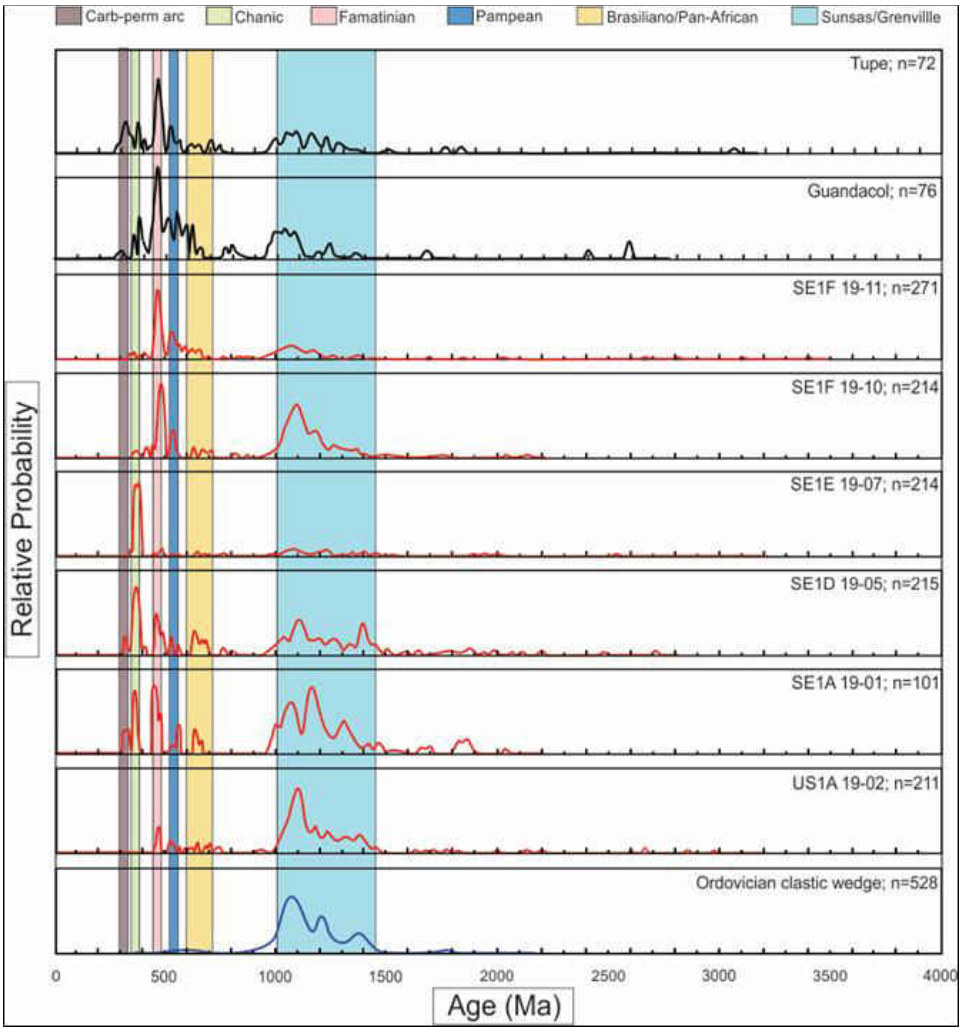

Figure 21 – Stacked probability plots of samples analyzed as part of this project and from other formations in the Paganzo Basin, with the maximum depositional age for the Ansilta formation of 333.6 ± 2.4 Ma. The red colored age frequency curves are from this study, blue are from Thomas et al. (2015) collected from various early Paleozoic formations in the Precordillera range, and black are from Craddock et al. (2019) for the Tupe Formation and Pauls et al. (2020) for the Guandacol Formation. The timing of Gondwanan orogenies are indicated by the colored backgrounds. Purple = Frontal Cordillera island arc (~290-330 Ma), green = Chañic orogeny (~330-390 Ma), pink = Famatinian orogeny (~450-490 Ma), dark blue = Pampean orogeny (~500-550 Ma), yellow = Brasiliano/Pan-African orogeny (~590-700 Ma), and light blue = Mesoproterozoic/Grenvillian source (1000-1450 Ma).

1078, 453 and 365 Ma. The correspondence of Famatinian and the 1078 Ma Mesoproterozoic age peaks indicates similar source areas. The 1170 Ma peak could also contain reworked sediments from other early Paleozoic sedimentary deposits in the Precordillera and Cuyania Terrane. Thomas et al. (2015) discuss the provenance of detrital grains from the Middle - Upper Ordovician clastic wedge in the Precordillera, which has detrital zircons from 1000-1350 Ma

and a secondary mode from 1350-1500 Ma. They interpret the strata as having formed as an accretionary prism that had its sediment derived from the western Sierras Pampeanas for the younger Proterozoic-aged population and a Laurentian source for the older ages. Ordovician age strata located 5-10 km to the east and immediately to the north of our study area indicate that the local basement underlying the Ansilta served as the main source for the 1170 Ma and 1078 Ma age peaks. This is also the first occurrence of Chañic-aged (370-340 Ma) zircons within the sample set for the Ansilta Formation, and likely originated from post-orogenic granitic complexes in the Andean Frontal Cordillera, Precordillera, or the Famatinian Arch (Geuna et al., 2008; Gallastegui et al., 2014; Moreno et al., 2018; Dahlquist et al., 2018). Gallastegui et al. (2014) provide an age of 348 Ma for a conglomerate clast collected from the Del Raton Formation, which rocks of similar age occur 10 to 20 km east of our study site. Clast counts from diamictites in this interval are consistent with this interpretation. The youngest single detrital grain from the entire measured section was found in the basal sands, and has an age of 322 ± 3.7 Ma. This indicates a maximum depositional age of late Serpukhovian to early Bashkirian for the glacial strata. Due to the young age of this grain, it is unlikely to have originated from a Chañic post-collisional intrusion. Instead, this grain may have been derived from an active magmatic arc situated along the Panthalassa margin.

Sample SE1D 1905 (n=215) comes from an interlayered sand lens within diamictite from stage 2. The age spectrum ranges from 321-2702 Ma and has a primary Chañic age peak of 364, and secondary Mesoproterozoic peaks at 1102 and 1384 Ma. The increasing quantity of first cycle zircons (364 Ma) is interpreted to represent a glacier sourcing material directly from a late Devonian to early Carboniferous aged intrusive complexe or reworked from an equivalent volcanic deposit. These sources correspond to local basement rocks from the Precordillera and

the Cuyania Composite Terrane. Late Devonian to early Carboniferous intrusions are absent in the southern and central Precordillera, however Moreno et al. (2020) and the La Rioja Province geologic map show some small intrusions of this age in the northern Precordillera in the vicinity of Sierra de Umango and Sierra de Maz. These are the closest intrusions of this age to the Ansilta Formation, so it is interpreted that this area provided the source for the Chañic-aged zircons.

Sample SE1E 1907 (n=214) comes from an interval of sandstone and pebble conglomerate with diamictite at the base of stage 2. This sample has a principal age peak of 366 Ma, a lesser peak at 1098 Ma, and the detrital zircon age spectrum ranges from 330-2785 Ma. This sample is dominated by a Chañic age peak, and the absence of significant Famatinian and Mesoproterizoic ages imply that ice was sourcing material from local post-orogenic granitic intrusions during the height of glaciation with minimal sediment reworking. The closest source of late Devonian to early Carboniferous intrusions occur in the northern Precordillera, which likely serves as the source area for these young grains (Dahlquist et al., 2018; Moreno et al., 2020; Fig. 22).

Sample SE1F 1910 (n=215) was collected from the upper member of the Ansilta formation, with these sandstones representing a wave-dominated deltaic environment overlying interpreted post-glacial transgressive shale due to the absence of striated clasts in this interval. The age spectrum ranges from 352-2129 Ma and has a primary age peak at 467 Ma, and secondary peaks at 533 and 1082 Ma. The disappearance of Chañic aged grains may indicate a potential migration of sediment sourcing further to the east, however the provenance signature shows similar age clusters as those in the lowermost diamictite interval. Therefore, this

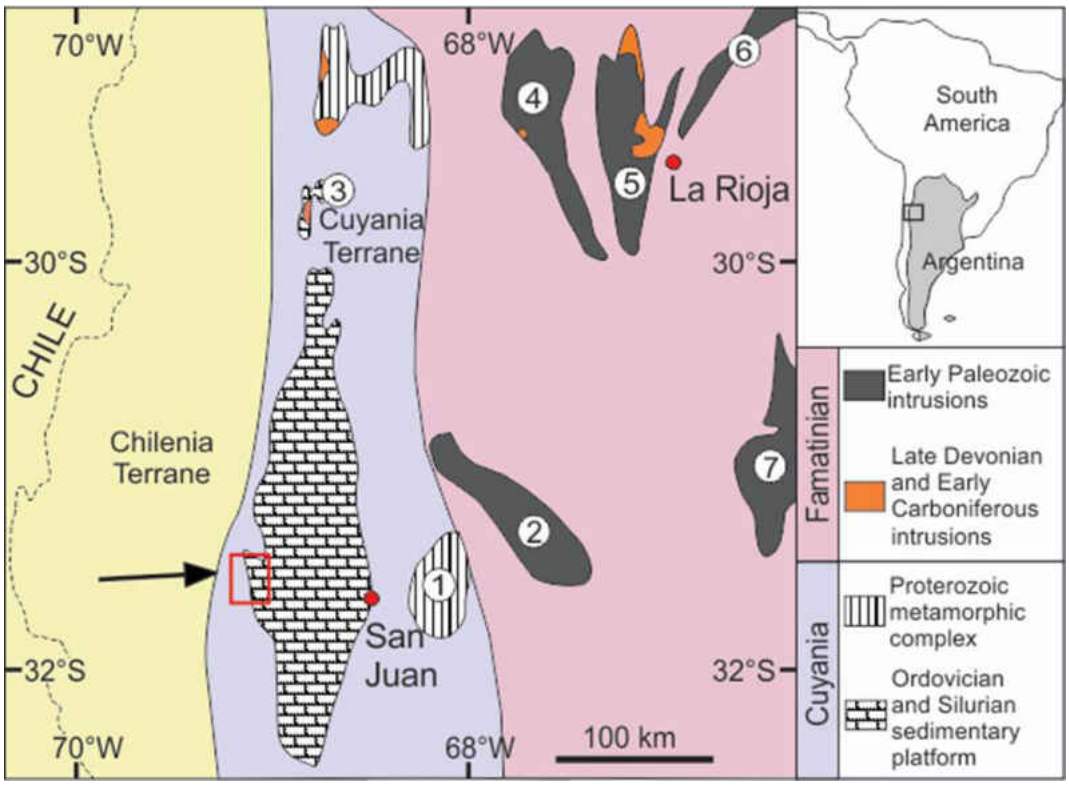

Figure 22 – Simplified geologic terrane map of north western Argentina and the location of Mesoproterizoic-Carboniferous igneous, metamorphic, and sedimentary provinces. Map is modified from Dahlquist et al. (2012) and Pauls et al. (2020). Inset numbers correspond to present-day mountain ranges in the region: (1) Pie de Palo; (2) Valle Fértil; (3) Umango and Maz; (4) Famatina; (5) Velasco; (6) Ambato; (7) Chepes.

depositional system is likely still sourcing and reworking material from the same region as those of the underlying glacial units.

Sample SE1F 1911 (n=271) was collected from fluvial sandstones near the top of the measured section. The age spectrum ranges from 327 to 3412 Ma, and has a primary age peak of 465 Ma, with secondary peaks at 526 and 1094 Ma. The change in age population dominance from Mesoproterozoic at the base of the upper member (SE1F 1910) to a very distinct Famatinian signature at the top (SE1F 1911) as well as sharing similar age clusters with the Guandacol and Tupe formation supports the idea that the Protoprecordillera was an uplift during glaciation, and during the late Carboniferous it was already subsiding and was no longer a substantial topographic high. In addition, the oldest analyzed zircons originated from this

sample, including four Archean aged grains and the oldest being 3412 ± 10.2 Ma. Archean aged crust (> 3.0 Ga) can be found in the Rio de la Plata craton in Uruguay and southern Brazil, and in the São Francisco and Amazon cratons in eastern and central Brazil (Hartmann et al., 2001; Cordani and Neves, 2018). Archean aged crust is nonexistent in western South America, so the presence of these grains indicates a distal sediment contribution and will be discussed further in the following paragraph. Although these were probably derived from basement on the eastern side of South America, the likelihood of these being reworked from sedimentary sources as second or multicycle zircons are high since there are so few Archean-aged grains in the Ansilta.

A Kolmogorov-Smirnov (K-S) analysis was performed on the cumulative probability curves of the analyzed zircons as a way of determining the statistical similarity of samples age spectra distributions. P-values greater than 0.05 indicate that the age spectra are statistically not different at the 95% confidence level and thus the samples may share the same provenance. If a sample shows a P > 0.05 match with another, the possibility that they have the same statistical distribution by means of a similar source area cannot be rejected, however it doesn't mean the samples are the same or share a spatial or temporal link. P-values show that the lower two samples are statistically related (US1A 1902 and SE1A 1901; p-value: 0.229); the second and third samples (SE1A 1901 and SE1D 1905; p-value: 0.054) also are related (Table 2). SE1F 1907 and SE1F 1910 are unrelated to any other sample. However, the uppermost sample SE1F 1911 is statistically similar to the Guandacol (p-value: 0.469) and Tupe (p-value: 0.381) formations in the Paganzo Basin. These datasets were provided from the Paganzo basin Guandacol and Tupe Formations by Craddock et al., 2019 and Pauls et al., 2020. Due to the statistical similarity of grains from fluvial sandstones of the upper member of the Ansilta

	USA1 1902	SE1A 1901	SE1D 1905	SE1E 1907	SE1F 1910	SE1F 1911	Guandacol	Tupe
USA1 1902		**0.228**	0.000	0.000	0.001	0.000	0.000	0.000
SE1A 1901	**0.228**		**0.054**	0.000	0.004	0.000	0.000	0.000
SE1D 1905	0.000	**0.054**		0.000	0.003	0.000	0.000	0.025
SE1E 1907	0.000	0.000	0.000		0.000	0.000	0.000	0.000
SE1F 1910	0.001	0.004	0.003	0.000		0.000	0.000	0.001
SE1F 1911	0.000	0.000	0.000	0.000	0.000		**0.982**	**0.210**
Guandacol	0.000	0.000	0.000	0.000	0.000	**0.982**		**0.548**
Tupe	0.000	0.000	0.025	0.000	0.001	**0.210**	**0.548**	

Table 2 – K-S analysis of late Paleozoic glaciogenic strata in NW Argentina. Red and blue = this study, orange = Paganzo basin (Craddock et al., 2019; Pauls et al., 2020). Yellow-bold = P-value of > 0.05, which indicates the age spectra are statistically not different and thus the samples may share the same provenance.

Formation with formations in the Paganzo basin combined with the similar age clusters, it is likely these grains were reworked for analogous deposits in the western Paganzo basin and were then transported to the late Ansilta area via fluvial processes.

7. Discussion

For this study, depositional processes have been refined from previous studies in order to incorporate new data from the Ansilta Formation (López-Gamundí, 1987; Taboada, 2004; Henry, 2010). The lithofacies are dominated by glacimarine and normal marine processes, similar to those found in modern day shelf and slope settings. While the occurrence of striated and faceted clasts is common in the lower 400m of the section, evidence for direct glacial contact is lacking (i.e., grooved pavements, sheared diamictites, roche moutonnées).

López-Gamundí (1987) characterized the depositional model for the glacimarine strata as a glacial drift build-up on a depositional slope, dominated by sediment gravity flows and turbidity currents. This interpretation conforms to our new findings, and our contribution includes a refined depositional model for the glacial, shallow marine, and fluvial strata that comprise the Ansilta formation, with an emphasis on glacial cyclicity and the delivery of large

volumes of sediment to a shelf-slope margin, and the subsequently re-deposition of this glacigenic sediment via sediment-gravity flow and mass transport processes.

Based on facies successions, the sequence stratigraphy interpretation for the lower diamictite-bearing member indicates at minimum five glacial advances, although some of these are likely short-distance readvances. The interpreted depositional system for the rocks in Stage 1, which records two glacial advances, is an ice proximal prograding distal morainal bank front or glacially influenced subaqueous fan, which transitions upward into mudstones and marls deposited on a basinal shelf in the absence of sea ice. Because of the lack of sub-glacial textures and features (i.e. striated and grooved pavements, thrust structures), and little relief along the basal contact of the formation, the lower diamictite-bearing interval was likely deposited during open marine conditions instead of being confined to a paleovalley. These fine-grained sediments are in turn overlain by pebbly mudstones, representing a glacial readvance and subsequent retreat. Stage 2 and 3 are interpreted to represent the distal and core portions of a morainal bank system, and records three glacial advances of varying degree. The facies successions for Stage 2 and Stage 3 are amalgamated, reactivated, and complexly interfingered, and the overall thickness of this interval (~275 m) is attributed to the dynamic environment of a morainal bank actively receiving sediments from the adjacent ice front. Post-glacial mudstone sedimentation replaces diamictites recorded in Stage 4, and corresponds with deeper water shales from localities in the Calingasta-Uspallata, Río Blanco, and Paganzo basins. The shallow marine (Stage 5) and fluvial (Stage 6) strata from the upper member of the Ansilta formation shows no further evidence of continued glaciation because of an absence of glacially faceted clasts and diamictites (López-Gamundí, 1997; Limarino et al., 2006).

The maximum depositional age for the Ansilta Formation is 333.6±2.4 Ma based on the twenty youngest detrital zircons found within the formation, while the youngest detrital zircon is 322 ± 3.7 Ma. This suggests that the Ansilta formation is broadly correlative with similar strata in the Calingasta-Uspallata Basin as well as in the Río Blanco and Paganzo basins, and was deposited during the Serpukhovian-Bashkirian glacial episode (cf. Limarino et al. 2006, 2014; Henry et al., 2010; Isbell et al., 2012; Montañez and Poulsen, 2013; Craddock et al., 2019; López-Gamundí et al. 2020). The underlying Ordovician and Silurian strata, which forms the basement that the Ansilta Formation rests on unconformibly, are dominated by zircons derived from basement rocks formed from Mesoproterozoic (1000-1450 Ma) aged rocks derived from the Precordillera and Cuyania Terranes, which originally may have been derived from the Laurentia Craton (Ramos, 1988; Azcuy et al., 1999; Thomas et al., 2015). Samples with direct glacial influence (SE1A 1901, SE1D 1905, SE1E 1907) show a distinct population of young zircons related to the Chañic orogeny (~360-390 Ma). This Chañic peak becomes more prominent in the uppermost sample collected from the lower member of the Ansilta Formation (SE1E 1907). Small age peak at ~465 Ma exists in each of these samples as well, indicating that rocks from the underlying Ordovician to Silurian aged accretionary prism contributed sediment to the lower member of the Ansilta formation. The number of younger grains increases over time while the Mesoproterozoic population decreases, suggesting a proximal sediment source area contributing first cycle late Devonian to early Carboniferous zircons and less sediment reworking from the underlying early Paleozoic basement. Samples SE1F 1910 and SE1F 1911 have a much different detrital zircon age spectra than our lowermost samples. No Chañic signal is evident here and the ~465 Famatinian signal is the most dominant, and also show prominent Pampean (~530 Ma) and Grenvillian (~1090 Ma) ages. These signals

share some resemblance to the lower most sample (SE1A 1901) with the distinction of having a more dominate Famatinian peak, it is likely that grains were derived locally from the underlying Ordovician and Silurian aged basement as well as reworked from Carboniferous aged sedimentary deposits to the east. Sample SE1F 1911 contained the oldest analyzed zircons, including 3 that are >3000 Ma and indicate a distal sediment contribution. These were originally derived from the Rio de la Plata craton, but have likely been reworked multiple times suggesting that they are from previously deposited sediments east of the Ansilta Formation.

Our uppermost sample (SE1F 1911) has a K-S match with both the Tupe and Guandacol Formations in the Paganzo basin. This relationship suggests a spatial and temporal link between the top of the Ansilta and the Tupe and Guandacol formations, and suggests that glacial deposits in the Paganzo basin were reworked and transported via large fluvial systems westward late in Ansilta deposition, well after glaciation had ceased in this portion of the Calingasta-Uspallata Basin.

8. Conclusion

Sediment derivation and transport was directly impacted by the presence of local ice centers. During the height of glaciation, as indicated by the volume of coarse clastic rocks, sediment was derived locally from the Precordillera and Cuyania terranes, or reworked from sediment originally derived from the Cuyania terrane, and then transported by glaciers to the study area before being deposited by glacial meltwater (plumes and underflows), debris flows, and iceberg rafting before being deposited as an ice proximal morainal bank and ice distal iceberg rain-out in a glacimarine shelf margin environment. In concordance with our detrital zircon analysis, an initial glacial center was situated over the Protoprecordillera during the late

Serpukhovian, which radiated outward, incising, transporting, and depositing the initial glacially derived sediments in the numerous paleovalleys across the region. During the early Bashkirian, an ice center was situated over the northern Precordillera, resulting in large amounts of locally sourced first cycle zircons from Chañic-aged intrusions. After local glaciation ceased and ice no longer filled fjord-like valleys during the collapse of the Protoprecordillera, sediment was derived from reworked glacial deposits, early Paleozoic and Mesoproterizoic metasedimentary, plutonic rocks from the Precordillera and Cuyania Terranes, as well as a minor amount of distally source material from the east. These sediments were then transported by fluvial systems into the area during late Ansilta time, potentially flowing through previous glacially carved paleovalleys, to littoral environments during a regional regression.

9. References

Abre, P., Cingolani, C.A., Cairncross, B., Chemale Jr, F., 2012. Siliciclastic Ordovician to Silurian units of the Argentine Precordillera: Constraints on provenance and tectonic setting in the proto-Andean margin of Gondwana. Journal of South American Earth Sciences 40, p. 1-22. doi: 10.1016/j.jsames.2012.07.013

Alonso-Muruaga, P.J., Limarino, C.O., Spalletti, L.A., Colombo Piñol, F., 2018. Depositional settings and evolution of a fjord system during the carboniferous glaciation in Northwest Argentina. Sedimentary Geology 369, 28-45. doi:10.1016/j.sedgeo.2018.03.002

Amos, A.J., Rolleri, E., 1965. El Carbónico marino en el valle Calingasta-Uspallata, San Juan-Mendoza. Boletin de Informaciones Petroleras 368, 50-71.

Aquino, C.D., Milana, J.P., Faccini, U.F., 2014. New glacial evidences at the Talacasto paleofjord (Paganzo basin, W-Argentina) and its implications for the paleogeography of the Gondwana margin. Journal of South American Earth Sciences 56, 278-300. doi:10.1016/j.jsames.2014.09.001

Azcuy, C.L., Carrizo, H.A., Caminos, R., 1999. Carbonífero y Pérmico de las Sierras Pampeanas, Famatina, Precordillera, Cordillera Frontal y Bloque de San Rafael. Geología Argentina 29(12), 261-318.

Boulton, G.S., 1990. Sedimentary and sea level changes during glacial cycles and their control on glacimarine facies architecture. Geological Society, London, Special Publications 53(1), 15-52. doi:10.1144/GSL.SP.1990.053.01.02

Buatois, L.A., Netto, R.G., Mángano, M.G., Balistieri, P.R., 2006. Extreme freshwater release during the late Paleozoic Gondwana deglaciation and its impact on coastal ecosystems. Geology 34(12), 1021-1024. doi:10.1130/G22994A.1

Cagliari, J., Philipp, R.P., Buso, V.V., Netto, R.G., Klaus Hillebrand, P., da Cunha Lopes, R., Stipp Basei, M.A., Faccini, U.F., 2016. Age constraints of the glaciation in the Paraná Basin: evidence from new U–Pb dates. Journal of the Geological Society 173, 871-874. doi:10.1144/jgs2015-161

Cai, J., Powell, R.D., Cowan, E.A., Carlson, P.R., 1997. Lithofacies and seismic-reflection interpretation of temperate glacimarine sedimentation in Tarr Inlet, Glacier Bay, Alaska. Marine Geology 143(1-4), 5-37. doi:10.1144/jgs2015-161

Catuneanu, O., Abreu, V., Bhattacharya, J.P., Blum, M.D., Dalrymple, R.W., Eriksson, P.G., Fielding, C.R., Fisher, W.L., Galloway, W.E., Gibling, M.R., Giles, K.A., 2009. Towards the standardization of sequence stratigraphy. Earth-Science Reviews 92(1-2), 1-33. doi:10.1016/j.earscirev.2008.10.003

Césari, S.N., Gutiérrez, P.R., 2000. Palynostratigraphy of Upper Paleozoic sequences in central-western Argentina. Palynology 24(1), 113–146. doi:10.1080/01916122.2000.9989541

Césari, S.N., Limarino, C.O., Gulbranson, E.L., 2011. An Upper Paleozoic bio-chronostratigraphic scheme for the western margin of Gondwana. Earth-Science Reviews 106, 149-160. doi:10.1080/01916122.2000.9989541

Césari, S.N., Gaido, M.F., Cegarra, M.I., Anselmi, G., 2014. The First Record of Permian Flora in the Ansilta Formation (Western Precordillera of Argentina) and its Regional Correlation. Ameghiniana 51(5), 428-432. doi:10.5710/AMGH.24.07.2014.2764

Césari, S.N., Limarino, C.O., Spalletti, L.A., Piñol, F.C., Perez Loinaze, V.S., Ciccioli, P.L., Friedmane, R., 2019. New U-Pb zircon age for the Pennsylvanian in Argentina: Implications in palynostratigraphy and regional stratigraphy. Journal of South American Earth Sciences 92, 400-416. doi:10.1016/j.jsames.2019.02.010

Césari S.N, Perez Loinaze V.S., 2020. Update of the Pennsylvanian palynostratigraphy from central-western Argentina. Journal of South American Earth Sciences, 102933. doi:10.1016/j.jsames.2020.102933

Cordani, U.G., Neves, B.B.D.B., 1982. The geologic evolution of South America during the Archaean and Early Proterozoic. Revista Brasileira de Geociências 12(1-3), 78-88.

Cowan, E.A., Powell, R.D., 1990. Suspended sediment transport and deposition of cyclically interlaminated sediment in a temperate glacial fjord, Alaska, USA. Geological Society, London, Special Publications 53(1), 75-89. doi:10.1144/GSL.SP.1990.053.01.04

Craddock, J.P., Ojakangas, R. W., Malone, D.H., Konstantinous, A., Mory, A., Bauer, W., Thomas, R.J., Craddock-Affinati, S., Pauls, K., Zimmerman, U., Botha, G., Rochas-Campos, A., Tohver, E., Riccomini, C., Martin, J., Redfern, J., Horstwood, M., Gehrels, G., 2019. Provenance of Permo-Carboniferous Glacial Diamictites across Gondwana. Earth-Science Reviews 192, 285-316. doi:10.1016/j.earscirev.2019.01.014

Crowell, J.C., 1978. Gondwana glaciation, cyclothems, continental positioning, and climate change. American Journal of Science 278, 1345-1372. doi:10.2475/ajs.278.10.1345

Crowell, J.C., 1999. Pre-Mesozoic Ice Ages: Their Bearing on Understanding the Climate System. Geological Society of America Memoir 192.

Crowell, J.C., Frakes, L.A., 1970. Phanerozoic glaciation and the causes of ice ages. American Journal of Science 268, 193-224. doi:10.2475/ajs.268.3.193

Csaky, A., 1963. Geología de la zona situada al norte del Cordón del Naranjo y al sur del Cerro Las Cabeceras, departamento Calingasta provincia de San Juan. Facultad de Ciencias Extractas y Naturales de la Universidad Nacional de Buenos Aires.

Dahlquist, J.A., Alasino, P.H., Basei, M.A., Cámera, M.M.M., Grande, M.M., Neto, M.D.C.C., 2018. Petrological, geochemical, isotopic, and geochronological constraints for the Late Devonian–Early Carboniferous magmatism in SW Gondwana (27–32 LS): an example of geodynamic switching. International Journal of Earth Sciences 107(7), 2575-2603. doi:10.1007/s00531-018-1615-9

DeCelles, P.G., Giles, K.A., 1996. Foreland basin systems. Basin research 8(2), 105-123. doi:10.1046/j.1365-2117.1996.01491.x

Deptuck, M.E., Sylvester, Z., 2018. Submarine fans and their channels, levees, and lobes. Submarine Geomorphology, 273-299.

De Rosa, L., 1983. Sedimentitas continentales del Carbónico inferior en el flanco occidental de la Precordillera, departamento Calingasta, provincia de San Juan. Revista de la Asociación Argentina de Mineralogía, Petrografía y Sedimentología 14, 51–69.

Dowdeswell, J.A., Whittington, R.J., Marienfeld, P., 1994. The origin of massive diamicton facies by iceberg rafting and scouring, Scoresby Sund, East Greenland. Sedimentology 41(1), 21-35. doi:10.1111/j.1365-3091.1994.tb01390.x

Dykstra, M., Kneller, B., Milana, J.P., 2006, Deglacial and postglacial sedimentary architecture in a deeply incised paleovalley-paleofjord; the Pennsylvanian (Late Carboniferous) Jejenes Formation, San Juan, Argentina. Geological Society of America Bulletin 118(7-8), 913-937. doi:10.1130/B25810.1

Fielding, C.R., Frank, T.D., Isbell, J.L., 2008. The late Paleozoic ice age – a review of current understanding and synthesis of global climate patterns. Geological Society of America Special Paper 441, 343-354.

Gallastegui, G., Gonzalez-Menendez, L., Rubio-Ordonez, A., Cuesta, A., Gerdes, A., 2014. Origin and provenance of igneous clasts from late Palaeozoic conglomerate formations (Del Raton and El Planchon) in the Andean Precordillera of San Juan, Argentina. Journal of Iberian Geology 40(2), 261-283. doi:10.5209/rev_JIGE.2014.v40.n2.45298

Gehrels, G.E., Valencia, V., Ruiz, J., 2008. Enhanced precision, accuracy, efficiency, and spatial resolution of U-Pb ages by laser ablation-multicollector-inductively coupled plasma-mass spectrometry. Geochemistry, Geophysics, Geosystems 9. doi:10.1029/2007GC001805

Gehrels, G., 2014. Detrital Zircon U-Pb Geochronology Applied to Tectonics. Annual Review of Earth and Planetary Sciences (42), 127-149. doi:10.1146/annurev-earth-050212-124012

Geuna, S.E., Escosteguy, L.D., Miró, R., 2008. Palaeomagnetism of the Late Devonian–Early Carboniferous Achala Batholith, Córdoba, central Argentina: implications for the apparent polar wander path of Gondwana. Gondwana Research 13(2), 227-237. doi:10.1016/j.gr.2007.05.006

Griffis, N.P., Mundil, R., Montanez, I.P., Isbell, J.L., Fedorchuk, N., Vesely, F., Iannuzzi, R.,Yin, Q.Z., 2018. A new stratigraphic framework built on U-Pb single zircon TIMS ages and implications for the timing of the penultimate icehouse (Paraná Basin, Brazil). Geological Society of America Bulletin 130, 848-858. doi:10.1130/B31775.1

Gulbranson, E.L., Montanez, I.P., Schmitz, M.D., Limarino, C.O., Isbell, J.L., Marenssi, S.A., Crowley, J.L., 2010. High-precision U-pb calibration of carboniferous glaciation and climate history, Paganzo group, NW Argentina. Geological Society of America Bulletin 122, 1480-1498. doi:10.1130/B30025.1

Hambrey, M.J., Glasser, N.F., 2012. Discriminating glacier thermal and dynamic regimes in the sedimentary record. Sedimentary Geology 251, 1-33. doi:10.1016/j.sedgeo.2012.01.008

Hampson, G.J., Storms, J.E., 2003. Geomorphological and sequence stratigraphic variability in wave-dominated, shoreface-shelf parasequences. Sedimentology 50(4), 667-701. doi:10.1046/j.1365-3091.2003.00570.x

Handford, C.R., Loucks, R.G., 1993. Carbonate depositional sequences and systems tracts-responses of carbonate platforms to relative sea-level changes: Chapter 1.

Hartmann, L.A., Campal, N., Santos, J.O.S., McNaughton, N.J., Bossi, J., Schipilov, A., Lafon, J.M., 2001. Archean crust in the Rio de la Plata Craton, Uruguay-SHRIMP U-Pb zircon reconnaissance geochronology. Journal of South American Earth Sciences 14(6), 557-570. doi:10.1016/S0895-9811(01)00055-4

Heckel, P.H., 2008. Pennsylvanian cyclothems in midcontinent North America as far-field effects of waxing and waning of Gondowana ice sheets. Geological Society of America Special Paper 441, 275-289. doi:10.1144/GSL.SP.1991.058.01.1

Henry, L.C., Isbell, J.L., Limarino, C.O, 2008. Carboniferous glacigenic deposits of the proto-Precordillera of west-central Argentina. Geological Society of America Special Paper 441, 131–142. doi:10.1130/2008.2441(09)

Henry, L.C., Isbell, J.L., Limarino, C.O., McHenry, L.J., Fraiser, M.L., 2010. Mid-Carboniferous deglaciation of the Protoprecordillera, Argentina recorded in the Agua de Jagüel palaeovalley. Palaeogeography, Palaeoclimatology, Palaeoecology 298(1-2), 112-129. doi:10.1016/j.palaeo.2010.03.051

Hofstra, M., Hodgson, D.M., Peakall, J., Flint, S.S., 2015. Giant scour-fills in ancient channel-lobe transition zones: Formative processes and depositional architecture. Sedimentary Geology 329, 98-114. doi:10.1016/j.sedgeo.2015.09.004

Isbell, J.L., Miller, M.F., Wolfe, K.L., Lenaker, P.A., 2003. Timing of late Paleozoic Glaciation in Gondwana: was glaciation responsible for the development of northern hemisphere cyclothems?. Geological Society of America Special Paper 370, 5-24.

Isbell, J.L., Henry, L.C., Gulbranson, E.L., Limarino, C.O., Fraser, M.L., Koch, Z.L., Ciccioli, P.L., Dineen, A.A., 2012. Glacial paradoxes during the LPIA: evaluating the equilibrium line altitude as a control on glaciation. Earth-Science Reviews 22, 1-19. doi:10.1016/j.gr.2011.11.005

Isbell, J.L., Biakov, A.V., Verdernikov, I., Davydov, V.I., Gulbranson, E.L., Fedorchuk, N.D., 2016. Permian diamictites in northeastern Asia: Their significance concerning the bipolarity of the late Paleozoic ice age. Earth-Science Reviews 154, 279-300. doi:10.1016/j.earscirev.2016.01.007

Kissock, J.K., Finzel, E.S., Malone, D.H., Craddock, J.P., 2018. Lower–Middle Pennsylvanian strata in the North American midcontinent record the interplay between erosional unroofing of the Appalachians and eustatic sea-level rise. Geosphere 14(1), 141-161. doi:10.1130/GES01512

Kneller, B., Milana, J.P., Buckee, C., al Ja'aidi, O., 2004. A depositional record of deglaciation in a paleofjord (Late Carboniferous [Pennsylvanian] of San Juan Province, Argentina): The role of catastrophic sedimentation. GSA Bulletin 116(3-4), 348-367. doi:10.1130/B25242.1

Leclair, S.F., 2002. Preservation of cross-strata due to the migration of subaqueous dunes: an experimental investigation. Sedimentology 49(6), 1157-1180. doi:10.1046/j.1365-3091.2002.00482.x

Limarino, C., Tripaldi, A., Marenssi, S., Fauqué, L., 2006. Tectonic, sealevel, and climatic controls on late Paleozoic sedimentation in the western basins of Argentina. Journal of South American Earth Sciences 33(3-4), 205–226. doi:10.1016/j.jsames.2006.09.011

Limarino, C.O., Alonso-Muruaga, P.J., Ciccioli, P.L., Perez Loinaze, V.S., Césari, S.N., 2014a. Stratigraphy and palynology of a late Paleozoic glacial paleovalley in the Andean Precordillera, Argentina. Palaeogeography, Palaeoclimatology, Palaeoecology 412, 223-240. doi:10.1016/j.palaeo.2014.07.030

Limarino, C.O., Césari, S.N., Spalletti, L.A., Taboada, A.C., Isbell, J.L., Geuna, S., Gulbranson, E.L., 2014b. A paleoclimatic review of southern South America during the late Paleozoic: a record from icehouse to extreme greenhouse conditions. Gondwana Research 25, 1396–1421. doi:10.1016/j.gr.2012.12.022

López-Gamundí, O.R., 1986. Turbiditas en la sección basal de la Formación Ansilta, Paleozoico superior de la Precordillera Occidental, provincia de San Juan: Revista de la Asociacion Geologica Argentina 41, 106-116

López-Gamundi, O.R., 1987. Depositional models for the glaciomarine sequences of Andean Late Paleozoic basin of Argentina. Sedimentary Geology 52, 109-126. doi:10.1016/0037-0738(87)90018-2

López-Gamundí, O.R., Azcuy, C.L., Cuerda, A., Valencio, D.A., Vilas, J.F., 1987. Cuencas Rio Blanco y Calingasta-Uspallata. El Sistema Carbonífero en la República Argentina. Córdoba, Nacional de Ciencias de Córdoba, 101-132.

López-Gamundí, O.R., 1991. Thin-bedded diamictites in the glacimarine Hoyada Verde Formation (Carboniferous), Calingasta-Uspallata Basin, western Argentina: a discussion on the emplacement condition of subaqueous cohesive debris flows. Sedimentary Geology 73(3-4), 247-256. doi:10.1016/0037-0738(91)90087-T

López-Gamundí, O.R, Espejo I.S., Conaghan P.J., Powell C.M., Veevers J.J., 1994. Southern South America. Geological Society of America Memoir 184, 281-329.

López-Gamundi, O.R., 1997. Glacial-Postglacial Transition in the Late Paleozoic Basins of South America. Late Glacial and Postglacial Environmental Changes-Quaternary, Carboniferous-Permian, and Proterozoic, 147-168.

López Gamundí, O.R., Martínez, M., 2003. Esquema estratigráfico-secuencial para las unidades neopaleozoicas de la cuenca Calingasta-Uspallata en el flanco occidental de la Precordillera. Revista de la Asociación Geológica Argentina 58(3), 367-382.

López-Gamundi, O.R., Buatois, L.A., 2010. Late Paleozoic glacial events and postglacial transgressions in Gondwana. GSA Special Paper 468, v-viii.

López-Gamundí, O.R., Sterren, A.F., Cisterna, G.A., 2016. Inter-and intratill boulder pavements in the Carboniferous Hoyada Verde Formation of West Argentina: An insight on glacial advance/retreat fluctuations in Southwestern Gondwana. Palaeogeography, Palaeoclimatology, Palaeoecology 447, 29-41. doi:10.1016/j.palaeo.2016.01.038

Ludwig, K., 2008. Isoplot 3.6: Berkeley Geochronology Center Special Publication 4, 77.

Mitchum Jr, R.M., Van Wagoner, J.C., 1991. High-frequency sequences and their stacking patterns: sequence-stratigraphic evidence of high-frequency eustatic cycles. Sedimentary Geology 70(2-4), 131-160. doi:10.1016/0037-0738(91)90139-5

Moncrieff, A.C.M., 1989. Classification of poorly-sorted sedimentary rocks. Sedimentary Geology 65(1-2), 191-194. doi:10.1016/0037-0738(89)90015-8

Montañez, I.P., Poulsen, C.J., 2013. The Late Paleozoic Ice Age: an evolving paradigm. Annual Reviews of Earth and Planetary Sciences 41, 629-656. doi:10.1146/annurev.earth.031208.100118

Moreno, J.A., Dahlquist, J.A., Cámera, M.M.M., Alasino, P.H., Larrovere, M.A., Basei, M.A., Galindo, C., Zandomeni, P.S., Rocher, S., 2020. Geochronology and geochemistry of the Tabaquito batholith (Frontal Cordillera, Argentina): geodynamic implications and temporal correlations in the SW Gondwana margin. Journal of the Geological Society 177(3), 455-474. doi:10.1144/jgs2019-062

Moxness, L.D., Isbell, J.L., Pauls, K.P., Limarino, C.O., J. Schencman, 2018. Sedimentology of the mid-Carboniferous fill of the Olta paleovalley, eastern Paganzo Basin, Argentina: Implications for glaciation and controls on diachronous deglaciation in western Gondwana during the late Paleozoic Ice Age. Journal of South American Earth Sciences 84, 127-148. doi:10.1016/j.jsames.2018.03.015

Mulder, T., Alexander, J., 2001. The physical character of subaqueous sedimentary density flows and their deposits. Sedimentology 48(2), 269-299. doi:10.1046/j.1365-3091.2001.00360.x

Naipauer, M., Vujovich, G.I., Cingolani, C.A., McClelland, W.C., 2010. Detrital zircon analysis from the Neoproterozoic–Cambrian sedimentary cover (Cuyania terrane), Sierra de Pie de Palo, Argentina: Evidence of a rift and passive margin system?. Journal of South American Earth Sciences 29(2), 306-326. doi:10.1016/j.jsames.2009.10.001

Pauls, K.N., Isbell, J.L., Limarino, C.O., Alonso-Murauga, P.J., Malone, D.H., Schencman, L.J., Colombi, C.E., Moxness, L.D., 2020. Constraining late Paleozoic ice extent in the Paganzo basin of western Argentina: Provenance of the lower Paganzo group strata. Journal of South American Earth Sciences, 102899. doi:10.1016/j.jsames.2020.102899

Pemberton, E.A., Hubbard, S.M., Fildani, A., Romans, B., Stright, L., 2016. The stratigraphic expression of decreasing confinement along a deep-water sediment routing system: Outcrop example from southern Chile. Geosphere 12(1), 114-134. doi:10.1130/GES01233.1

Posamentier, H.W., Allen, G.P., 1999. Siliciclastic sequence stratigraphy: concepts and applications. Society for Sedimentary Geology 7, 210

Powell, R.D., 1983. Glacial-marine sedimentation processes and lithofacies of temperate tidewater glaciers, Glacier Bay, Alaska. Glacial-Marine Sedimentation, 185-232. doi:10.1007/978-1-4613-3793-5_4

Powell, R.D., 1990. Glacimarine processes at grounding-line fans and their growth to ice-contact deltas. Geological Society, London, Special Publications 53(1), 53-73. doi:10.1144/GSL.SP.1990.053.01.03

Powell, R. D., Cooper, J. M., 2002. A glacial sequence stratigraphic model for temperate, glaciated continental shelves. Geological Society, London, Special Publications 203(1), 215-244. doi:10.1144/GSL.SP.2002.203.01.12

Powell, R. and Domack, G.W., 2002. Modern glaciomarine environments. Modern and Past Glacial Environments, 361-389.

Ramos, V.A., Jordan, T.E., Allmendinger, R.W., Kay, S.M., Cortes, J.M., Palma, M.A., 1984. Chilenia: an allochthonous terrane in the Paleozoic evolution of the Central Andes. Actas del Congreso Geológico Argentino 2, 84–106.

Ramos, V.A., Jordan, T.E., Allmendinger, R.W., Mpodozis, M.C., Kay, S.M., Cortes, J.M., Palma, M., 1986. Paleozoic terranes of the central Argentine-Chilean Andes. Tectonics 5, 855–880. doi:10.1029/TC005i006p00855

Ramos, V.A., 1988. The tectonics of the Central Andes; 30 to 33 S latitude. Geological Society of America Special Paper 218, 31.

Ramos, V.A., 2004. Cuyania, an exotic block to Gondwana: review of a historical success and the present problems. Gondwana Research 7(4), 1009-1026. doi:10.1016/S1342-937X(05)71081-9

Rosenblume, J. A., Powell, R. D., 2019. Glacial sequence stratigraphy of ANDRILL-1B core reveals a dynamic subpolar Antarctic Ice Sheet in Ross Sea during the late Miocene. Sedimentology 66(6), 2072-2097. doi:10.1111/sed.12592

Schieber, J., 1999. Microbial mats in terrigenous clastics; the challenge of identification in the rock record. Palaios 14(1), 3-12. doi:10.2307/3515357

Shanmugam, G., 1997. The Bouma sequence and the turbidite mind set. Earth-Science Reviews 42(4), 201-229. doi:10.1016/S0012-8252(97)81858-2

Sobiesiak, M.S., Kneller, B., Alsop, G.I., Milana, J.P., 2018. Styles of basal interaction beneath mass transport deposits. Marine and Petroleum Geology 98, 629-639. doi:10.1016/j.marpetgeo.2018.08.028

Taboada, A. C., 2004. Braquiópodos y bioestratigrafía del Carbonífero del Cordón del Naranjo (Subcuenca Calingasta-Uspallata), Argentina. Ameghiniana 41(3), 405-422.

Taboada, A.C., 2009. An Approach to the Carboniferous-Early Permian Stratigraphy, Paleontology, Paleogeography and Paleoclimatology of the Calingasta-Uspallata Subbasin (Western Argentina) and Tepuel-Genoa Basin (Patagonia, Argentina): A Fieldguide. Permophiles 53, 13-48.

Tedesco, J., Cagliari, J., Júnior, F.C., Girelli, T.J., Lana, C., 2019. Provenance and paleogeography of the Southern Paraná Basin: Geochemistry and UPb zircon geochronology of the Carboniferous-Permian transition. Sedimentary Geology 393, 105539. doi:10.1016/j.sedgeo.2019.105539

Thomas, G.S., Connell, R.J., 1985. Iceberg drop, dump, and grounding structures from Pleistocene glacio-lacustrine sediments, Scotland. Journal of Sedimentary Research 55(2), 243-249. doi:10.1306/212F8689-2B24-11D7-8648000102C1865D

Thomas, W.A., Astini, R.A., Mueller, P.A., McClelland, W.C., 2015. Detrital-zircon geochronology and provenance of the Ocloyic synorogenic clastic wedge, and Ordovician accretion of the Argentine Precordillera terrane. Geosphere 11(6), 1749-1769. doi.org/10.1130/GES01212.1

Valdez Buso, V., di Pasquo, M., Milana, J.P., Kneller, B., Fallgatter, C., Junior, F.C., Paim, P.S.G., 2017. Integrated U-Pb zircon and palynological/palaeofloristic age determinations of a Bashkirian palaeofjord fill, Quebrada Grande (Western Argentina). Journal of South American Earth Sciences 73, 202-222. doi:10.1016/j.jsames.2016.12.009

Valdez Buso, V., Milana, J., di Pasquo, M., Paim, P., Danielski Aquino, C., Cagliari, J., Chemale Junior, F., Kneller, B., 2020. Timing of the Late Palaeozoic glaciation in western Gondwana: New ages and correlations from Paganzo and Paraná basins. Palaeogeography, Palaeoclimatology, Palaeoecology 544, 109624. doi:10.1016/j.palaeo.2020.109624

Veroslavsky, G., Rossello, E.A., López-Gamundí, O., de Santa Ana, H., Assine, M.L., Marmisolle, J., Perinotto, A.D.J., 2020. Late Paleozoic tectono-sedimentary evolution of eastern Chaco-Paraná Basin (Uruguay, Brazil, Argentina and Paraguay). Journal of South American Earth Sciences, 102991. doi:10.1016/j.jsames.2020.102991

Vorren, T.O., Laberg, J.S., 1997. Trough mouth fans-palaeoclimate and ice-sheet monitors. Quaternary Science Reviews 16(8), 865-881. doi:10.1016/S0277-3791(97)00003-6

Woodcock, N.H., 1976. Structural style in slump sheets: Ludlow series, Powys, Wales. Journal of the Geological Society 132(4), 399-415. doi:10.1144/gsjgs.132.4.0399

Appendix

List of Detrital Zircon Samples and Ages

Sample US1A 1902		
Lat: S 31°49'38.5" Lon: W 069°14'53.2"		
Analysis	**Best age (Ma)**	**± (Ma)**
-Spot 79	451.7	3.5
-Spot 196	463.2	3.9
-Spot 61	468.7	6.3
-Spot 209	468.8	4.7
-Spot 40	469.9	4.5
-Spot 117	473.1	4.9
-Spot 217	473.9	4.0
-Spot 176	513.6	5.1
-Spot 214	521.9	5.0
-Spot 14	525.7	4.7
-Spot 202	536.1	5.5
-Spot 205	536.6	8.3
-Spot 166	560.7	5.2
-Spot 126	587.3	6.9
-Spot 204	608.5	6.7
-Spot 174	621.8	5.0
-Spot 149	641.5	6.1
-Spot 156	645.2	6.9
-Spot 171	648.5	6.6
-Spot 164	676.6	6.7
-Spot 172	677.3	7.2
-Spot 122	692.3	8.9
-Spot 195	699.4	6.3
-Spot 109	700.3	5.8
-Spot 103	729.4	8.2
-Spot 178	739.8	9.3
-Spot 131	908.5	16.1
-Spot 21	934.3	16.8
-Spot 58	986.5	20.8
-Spot 45	1000.6	18.5
-Spot 25	1002.3	20.7
-Spot 114	1003.6	13.4
-Spot 185	1017.8	18.5
-Spot 150	1022.8	14.5
-Spot 87	1027.6	21.5
-Spot 197	1027.7	15.3
-Spot 22	1029.6	19.3
-Spot 3	1033.6	16.5
-Spot 175	1035.5	19.6

Sample US1A 1902		
Lat: S 31°49'38.5" Lon: W 069°14'53.2"		
Analysis	**Best age (Ma)**	**± (Ma)**
-Spot 207	1036.5	14.4
-Spot 154	1036.7	13.5
-Spot 26	1039.5	19.5
-Spot 71	1043.2	30.7
-Spot 181	1044.9	15.2
-Spot 17	1047.3	14.7
-Spot 201	1047.3	21.4
-Spot 51	1047.8	17.4
-Spot 80	1050.8	19.0
-Spot 213	1051.6	14.2
-Spot 24	1051.7	13.2
-Spot 27	1054.6	20.7
-Spot 180	1060.6	15.5
-Spot 184	1060.8	16.9
-Spot 133	1062.6	13.8
-Spot 153	1062.9	14.0
-Spot 136	1063.6	39.8
-Spot 119	1064.5	19.2
-Spot 220	1064.6	21.2
-Spot 183	1069.2	13.1
-Spot 42	1069.4	16.6
-Spot 76	1070.4	13.1
-Spot 75	1073.0	12.2
-Spot 118	1075.2	23.7
-Spot 128	1076.0	13.3
-Spot 173	1076.7	19.6
-Spot 179	1077.0	19.9
-Spot 55	1079.7	18.0
-Spot 2	1080.7	17.7
-Spot 158	1080.8	17.1
-Spot 11	1081.0	12.0
-Spot 106	1083.0	13.3
-Spot 77	1083.7	14.1
-Spot 189	1084.4	14.3
-Spot 193	1085.3	14.9
-Spot 135	1087.4	19.9
-Spot 89	1088.2	13.1
-Spot 88	1088.7	21.3
-Spot 6	1089.6	19.2

Sample US1A 1902			Sample US1A 1902		
Lat: S 31°49'38.5" Lon: W 069°14'53.2"			Lat: S 31°49'38.5" Lon: W 069°14'53.2"		
Analysis	**Best age (Ma)**	**± (Ma)**	**Analysis**	**Best age (Ma)**	**± (Ma)**
-Spot 65	1090.8	16.2	-Spot 99	1132.5	19.9
-Spot 41	1091.5	25.6	-Spot 72	1134.7	25.2
-Spot 190	1092.8	14.6	-Spot 31	1137.0	11.1
-Spot 56	1093.7	14.5	-Spot 46	1138.4	16.2
-Spot 5	1094.2	13.6	-Spot 165	1142.5	15.3
-Spot 144	1095.0	16.0	-Spot 127	1144.5	24.4
-Spot 194	1095.2	19.9	-Spot 36	1149.2	13.9
-Spot 28	1095.5	17.5	-Spot 92	1158.0	14.2
-Spot 155	1095.6	13.1	-Spot 120	1167.5	18.2
-Spot 104	1096.6	23.4	-Spot 215	1167.8	17.6
-Spot 8	1097.1	15.7	-Spot 107	1168.5	13.6
-Spot 170	1097.1	16.6	-Spot 29	1169.4	17.3
-Spot 192	1097.5	15.2	-Spot 111	1170.1	12.7
-Spot 216	1097.8	23.5	-Spot 10	1174.2	19.1
-Spot 96	1099.3	17.0	-Spot 39	1175.1	21.2
-Spot 100	1100.9	16.7	-Spot 200	1175.9	11.9
-Spot 62	1103.0	15.3	-Spot 138	1179.5	14.9
-Spot 203	1104.1	15.4	-Spot 163	1179.5	16.3
-Spot 64	1104.8	21.6	-Spot 112	1180.1	14.1
-Spot 4	1105.5	17.3	-Spot 159	1180.6	13.5
-Spot 37	1105.8	16.5	-Spot 169	1184.0	13.0
-Spot 1	1108.0	13.1	-Spot 90	1185.3	13.9
-Spot 67	1109.0	19.8	-Spot 97	1190.0	13.3
-Spot 219	1109.3	19.3	-Spot 83	1202.6	19.1
-Spot 15	1110.2	15.2	-Spot 110	1205.0	17.0
-Spot 102	1110.3	13.0	-Spot 18	1214.1	15.9
-Spot 94	1111.0	11.9	-Spot 208	1220.0	12.0
-Spot 113	1111.1	13.9	-Spot 52	1221.7	18.7
-Spot 49	1112.8	13.6	-Spot 143	1222.4	15.6
-Spot 60	1114.2	14.5	-Spot 74	1223.1	13.2
-Spot 182	1115.8	18.6	-Spot 211	1226.4	16.2
-Spot 129	1119.5	13.9	-Spot 108	1228.1	12.9
-Spot 157	1119.6	14.1	-Spot 82	1233.0	13.2
-Spot 115	1121.7	26.2	-Spot 9	1233.1	14.2
-Spot 19	1122.0	17.1	-Spot 93	1234.2	15.0
-Spot 124	1122.7	24.5	-Spot 81	1234.5	16.3
-Spot 95	1124.7	17.4	-Spot 38	1239.7	14.9
-Spot 78	1124.9	17.6	-Spot 53	1250.6	16.1
-Spot 160	1131.7	14.9	-Spot 34	1253.8	12.3

Sample US1A 1902		
Lat: S 31°49'38.5" Lon: W 069°14'53.2"		
Analysis	**Best age (Ma)**	**± (Ma)**
-Spot 48	1254.1	16.9
-Spot 54	1259.7	11.3
-Spot 101	1261.2	16.6
-Spot 125	1269.5	15.3
-Spot 85	1273.6	18.7
-Spot 47	1280.3	13.1
-Spot 123	1282.3	16.2
-Spot 12	1290.6	17.4
-Spot 137	1291.5	13.2
-Spot 57	1296.2	14.6
-Spot 16	1308.9	13.3
-Spot 191	1309.2	12.2
-Spot 70	1309.2	23.9
-Spot 168	1311.2	16.1
-Spot 147	1313.9	14.3
-Spot 167	1318.6	14.6
-Spot 32	1319.9	13.7
-Spot 134	1328.2	13.0
-Spot 142	1335.7	17.3
-Spot 98	1337.5	16.5
-Spot 161	1342.3	12.3
-Spot 44	1350.6	17.4
-Spot 199	1352.8	16.7
-Spot 151	1357.0	18.6
-Spot 130	1357.6	11.6
-Spot 105	1361.7	16.1
-Spot 35	1371.5	10.6
-Spot 152	1372.7	14.3
-Spot 63	1373.9	15.2
-Spot 141	1376.3	13.2
-Spot 59	1382.7	13.1
-Spot 145	1383.3	14.1
-Spot 20	1388.9	12.8
-Spot 30	1394.3	16.8
-Spot 84	1399.5	14.3
-Spot 210	1407.8	11.8
-Spot 177	1409.3	20.5
-Spot 73	1409.9	16.0
-Spot 198	1441.3	13.3

Sample US1A 1902		
Lat: S 31°49'38.5" Lon: W 069°14'53.2"		
Analysis	**Best age (Ma)**	**± (Ma)**
-Spot 50	1441.3	12.8
-Spot 187	1451.8	12.3
-Spot 43	1497.0	14.1
-Spot 206	1624.9	11.8
-Spot 68	1670.7	11.7
-Spot 86	1703.1	12.8
-Spot 146	1766.0	11.0
-Spot 33	1815.6	11.7
-Spot 140	1997.9	13.5
-Spot 13	2125.3	11.7
-Spot 218	2197.8	11.1
-Spot 186	2600.6	13.4
-Spot 69	2658.9	9.6
-Spot 132	2660.0	8.7
-Spot 23	2853.6	12.0
-Spot 139	2973.9	10.5

Sample SE1A 1901			Sample SE1A 1901		
Lat: S 31°49'38.7" Lon: W 069°14'54.0"			Lat: S 31°49'38.7" Lon: W 069°14'54.0"		
Analysis	**Best age (Ma)**	**± (Ma)**	**Analysis**	**Best age (Ma)**	**± (Ma)**
-Spot 90	322.0	3.7	-Spot 63	1077.2	15.2
-Spot 71	332.2	5.1	-Spot 82	1077.8	20.8
-Spot 39	339.0	4.3	-Spot 83	1077.9	20.8
-Spot 13	359.1	3.9	-Spot 7	1082.4	17.1
-Spot 55	364.1	3.6	-Spot 103	1087.9	12.0
-Spot 27	365.6	5.6	-Spot 18	1091.2	17.5
-Spot 25	366.2	3.6	-Spot 52	1094.8	18.9
-Spot 60	378.0	4.8	-Spot 35	1113.5	21.4
-Spot 15	447.1	4.4	-Spot 99	1124.8	13.9
-Spot 53	452.2	3.7	-Spot 92	1134.5	40.6
-Spot 77	453.1	4.3	-Spot 43	1151.4	12.5
-Spot 91	454.0	4.8	-Spot 74	1152.5	13.6
-Spot 93	460.8	5.3	-Spot 16	1155.1	22.6
-Spot 87	465.0	6.2	-Spot 67	1161.4	48.4
-Spot 68	473.1	4.9	-Spot 65	1162.0	23.1
-Spot 2	475.3	4.4	-Spot 64	1162.2	13.2
-Spot 46	534.9	9.6	-Spot 34	1162.8	12.1
-Spot 78	561.7	6.5	-Spot 110	1164.0	17.2
-Spot 76	562.5	4.6	-Spot 6	1165.4	16.9
-Spot 81	635.1	6.4	-Spot 86	1167.2	18.7
-Spot 72	638.1	5.7	-Spot 89	1167.5	12.4
-Spot 57	658.3	5.9	-Spot 44	1171.9	19.4
-Spot 41	988.3	14.7	-Spot 48	1172.3	15.4
-Spot 108	997.6	13.9	-Spot 107	1173.1	13.6
-Spot 80	1001.8	14.3	-Spot 84	1177.6	14.6
-Spot 37	1002.7	15.1	-Spot 3	1196.1	16.9
-Spot 4	1004.1	24.8	-Spot 104	1197.9	16.3
-Spot 38	1026.9	14.4	-Spot 98	1201.6	22.5
-Spot 58	1027.5	18.5	-Spot 51	1202.7	10.9
-Spot 40	1031.1	14.4	-Spot 85	1207.9	18.8
-Spot 66	1042.1	12.5	-Spot 45	1214.4	15.0
-Spot 96	1044.6	17.6	-Spot 105	1215.8	23.2
-Spot 94	1050.5	19.7	-Spot 95	1225.0	29.1
-Spot 21	1056.8	14.5	-Spot 10	1233.7	12.6
-Spot 23	1060.7	16.9	-Spot 100	1234.9	16.1
-Spot 49	1065.7	19.2	-Spot 56	1257.0	12.1
-Spot 59	1070.0	15.4	-Spot 11	1274.3	12.7
-Spot 30	1070.4	14.1	-Spot 69	1278.2	11.3
-Spot 28	1070.9	28.0	-Spot 26	1300.7	15.2

Sample SE1A 1901		
Lat: S 31°49'38.7" Lon: W 069°14'54.0"		
Analysis	**Best age (Ma)**	**± (Ma)**
-Spot 20	1301.3	14.3
-Spot 19	1309.6	11.6
-Spot 109	1311.3	11.3
-Spot 17	1319.1	13.5
-Spot 32	1320.1	20.8
-Spot 9	1330.2	14.2
-Spot 101	1338.2	11.8
-Spot 36	1355.8	17.2
-Spot 29	1362.0	17.4
-Spot 31	1369.7	18.4
-Spot 1	1412.8	16.3
-Spot 54	1426.1	13.9
-Spot 12	1467.5	13.8
-Spot 42	1475.9	15.9
-Spot 102	1535.6	30.8
-Spot 50	1663.1	12.3
-Spot 70	1696.7	11.4
-Spot 33	1828.0	14.4
-Spot 106	1829.1	13.1
-Spot 22	1856.3	13.7
-Spot 14	1866.7	14.8
-Spot 79	1875.0	11.3
-Spot 97	2042.9	15.2

Sample SE1D 1905		
Lat: S 31°49'45.1" Lon: W 069°14'55.3"		
Analysis	**Best age (Ma)**	**± (Ma)**
-Spot 116	331.7	3.1
-Spot 89	332.7	5.7
-Spot 28	336.0	4.3
-Spot 203	343.7	3.1
-Spot 42	345.1	4.2
-Spot 23	345.2	3.0
-Spot 182	345.7	3.6
-Spot 75	346.9	3.8
-Spot 184	348.5	4.4
-Spot 6	348.7	4.4
-Spot 53	348.9	3.4
-Spot 63	350.7	4.2
-Spot 112	352.6	4.4
-Spot 17	354.2	3.1
-Spot 180	355.0	4.5
-Spot 29	355.5	3.4
-Spot 30	357.8	4.9
-Spot 26	358.3	3.3
-Spot 20	358.6	3.6
-Spot 95	360.2	3.0
-Spot 152	360.8	4.5
-Spot 198	363.6	3.0
-Spot 209	363.9	4.0
-Spot 201	365.4	3.9
-Spot 119	365.7	3.8
-Spot 97	366.1	4.7
-Spot 80	366.2	3.4
-Spot 104	368.7	3.3
-Spot 186	370.8	4.7
-Spot 164	373.2	4.6
-Spot 142	373.4	3.5
-Spot 21	376.4	4.4
-Spot 94	377.9	4.0
-Spot 74	378.9	4.4
-Spot 160	394.5	3.3
-Spot 13	448.1	5.3
-Spot 98	454.5	4.1
-Spot 49	463.2	7.3
-Spot 191	463.5	4.1

Sample SE1D 1905		
Lat: S 31°49'45.1" Lon: W 069°14'55.3"		
Analysis	**Best age (Ma)**	**± (Ma)**
-Spot 205	464.2	5.0
-Spot 84	464.5	5.5
-Spot 132	466.0	4.2
-Spot 67	467.1	5.4
-Spot 35	470.6	4.3
-Spot 131	473.6	6.3
-Spot 31	475.4	4.8
-Spot 56	477.4	6.7
-Spot 121	483.9	5.2
-Spot 210	485.6	4.3
-Spot 126	487.0	5.6
-Spot 208	511.2	4.8
-Spot 122	514.2	4.7
-Spot 188	519.2	5.9
-Spot 185	520.6	4.8
-Spot 71	529.3	5.2
-Spot 69	531.8	4.7
-Spot 10	552.6	4.3
-Spot 50	556.1	6.2
-Spot 51	608.2	5.6
-Spot 190	616.9	5.9
-Spot 81	618.6	6.8
-Spot 105	620.1	9.4
-Spot 93	620.4	9.5
-Spot 143	622.7	6.5
-Spot 46	624.0	6.4
-Spot 39	631.0	5.9
-Spot 153	631.4	4.3
-Spot 37	642.8	6.4
-Spot 128	647.7	6.1
-Spot 24	648.1	7.4
-Spot 72	654.6	6.1
-Spot 206	663.5	6.7
-Spot 79	667.5	8.2
-Spot 2	670.7	5.8
-Spot 171	680.2	12.3
-Spot 140	685.0	8.1
-Spot 199	742.0	8.8
-Spot 14	753.6	8.2

Sample SE1D 1905		
Lat: S 31°49'45.1" Lon: W 069°14'55.3"		
Analysis	**Best age (Ma)**	**± (Ma)**
-Spot 174	760.5	9.4
-Spot 110	791.9	9.0
-Spot 92	946.5	20.9
-Spot 123	953.8	21.6
-Spot 169	973.2	12.9
-Spot 34	986.6	15.1
-Spot 1	1004.6	12.0
-Spot 58	1014.7	15.3
-Spot 54	1015.1	13.9
-Spot 113	1018.6	14.2
-Spot 127	1019.4	16.8
-Spot 117	1023.2	16.3
-Spot 147	1027.6	18.3
-Spot 189	1028.8	15.1
-Spot 125	1032.5	12.9
-Spot 61	1033.2	17.7
-Spot 76	1036.4	13.3
-Spot 88	1055.4	22.2
-Spot 85	1056.9	12.6
-Spot 38	1064.6	15.4
-Spot 90	1068.1	18.5
-Spot 9	1070.8	12.2
-Spot 64	1071.4	20.2
-Spot 59	1072.4	13.2
-Spot 65	1073.0	20.6
-Spot 11	1074.4	10.5
-Spot 139	1075.9	20.1
-Spot 145	1076.4	13.4
-Spot 216	1077.4	12.2
-Spot 150	1086.6	12.8
-Spot 134	1086.6	14.6
-Spot 202	1088.3	15.7
-Spot 27	1088.4	10.9
-Spot 157	1095.1	13.6
-Spot 151	1096.8	17.5
-Spot 5	1096.9	11.1
-Spot 118	1103.1	12.0
-Spot 141	1103.6	14.2
-Spot 148	1104.7	13.0

Sample SE1D 1905		
Lat: S 31°49'45.1" Lon: W 069°14'55.3"		
Analysis	**Best age (Ma)**	**± (Ma)**
-Spot 108	1105.2	14.2
-Spot 138	1108.8	17.1
-Spot 173	1110.0	12.6
-Spot 47	1110.7	18.2
-Spot 130	1111.1	14.6
-Spot 22	1112.7	11.7
-Spot 218	1115.8	15.1
-Spot 3	1117.7	16.5
-Spot 135	1122.4	29.8
-Spot 83	1129.8	16.3
-Spot 103	1132.3	30.5
-Spot 219	1136.3	10.5
-Spot 115	1141.9	12.1
-Spot 179	1150.1	14.4
-Spot 41	1153.1	13.7
-Spot 86	1157.1	14.9
-Spot 96	1159.7	18.9
-Spot 165	1165.8	15.4
-Spot 66	1175.3	15.4
-Spot 170	1176.8	12.8
-Spot 100	1182.2	13.8
-Spot 33	1184.6	18.4
-Spot 154	1187.5	17.3
-Spot 207	1189.9	15.5
-Spot 144	1202.0	12.8
-Spot 87	1204.9	15.3
-Spot 196	1218.3	14.3
-Spot 215	1229.0	13.3
-Spot 172	1229.4	19.7
-Spot 40	1230.1	15.5
-Spot 7	1239.8	14.9
-Spot 167	1247.7	10.1
-Spot 192	1248.8	11.4
-Spot 18	1250.7	16.9
-Spot 204	1253.9	23.3
-Spot 183	1256.4	14.5
-Spot 109	1264.0	12.5
-Spot 193	1267.6	13.5
-Spot 213	1290.0	17.4

Sample SE1D 1905		
Lat: S 31°49'45.1" Lon: W 069°14'55.3"		
Analysis	**Best age (Ma)**	**± (Ma)**
-Spot 181	1292.4	27.4
-Spot 197	1305.5	11.9
-Spot 44	1316.2	14.9
-Spot 220	1316.3	17.0
-Spot 19	1326.8	12.8
-Spot 78	1332.9	13.1
-Spot 43	1334.2	14.9
-Spot 57	1360.6	12.8
-Spot 124	1363.4	15.6
-Spot 200	1364.3	12.8
-Spot 176	1366.8	9.7
-Spot 161	1369.7	14.4
-Spot 91	1372.2	11.9
-Spot 73	1376.4	12.1
-Spot 159	1376.8	12.7
-Spot 137	1377.1	10.1
-Spot 120	1378.9	11.9
-Spot 129	1379.0	17.8
-Spot 214	1379.4	11.9
-Spot 8	1381.5	16.6
-Spot 136	1384.9	11.1
-Spot 166	1386.6	14.2
-Spot 48	1391.1	10.5
-Spot 178	1392.4	13.1
-Spot 82	1395.6	10.4
-Spot 77	1401.7	10.2
-Spot 111	1406.3	11.6
-Spot 16	1419.7	12.6
-Spot 15	1424.6	12.2
-Spot 70	1426.7	13.5
-Spot 158	1432.7	13.3
-Spot 62	1433.4	12.3
-Spot 107	1453.3	11.2
-Spot 217	1456.0	15.2
-Spot 12	1490.0	10.8
-Spot 155	1490.3	10.2
-Spot 168	1560.7	20.7
-Spot 163	1584.9	13.5
-Spot 114	1626.3	10.9

Sample SE1D 1905		
Lat: S 31°49'45.1" Lon: W 069°14'55.3"		
Analysis	**Best age (Ma)**	**± (Ma)**
-Spot 60	1638.3	11.4
-Spot 32	1717.9	14.5
-Spot 212	1752.3	15.7
-Spot 177	1769.6	12.1
-Spot 146	1788.1	16.7
-Spot 101	1805.5	10.3
-Spot 162	1832.3	9.6
-Spot 149	1850.8	11.9
-Spot 52	1864.2	12.8
-Spot 102	1867.5	11.9
-Spot 194	1880.0	13.0
-Spot 211	1922.3	10.4
-Spot 25	1972.3	11.4
-Spot 45	1973.8	9.9
-Spot 4	2048.7	12.2
-Spot 99	2096.4	14.7
-Spot 187	2186.6	11.9
-Spot 175	2190.4	13.1
-Spot 133	2470.4	14.4
-Spot 36	2702.4	10.1

Sample SE1E 1907		
Lat: S 31°49'48.4" Lon: W 069°14'57.3"		
Analysis	**Best age (Ma)**	**± (Ma)**
-Spot 160	330.3	2.6
-Spot 164	334.1	3.1
-Spot 49	334.9	2.5
-Spot 40	338.8	10.8
-Spot 212	344.4	3.3
-Spot 107	344.5	3.4
-Spot 219	344.6	3.6
-Spot 18	344.9	3.1
-Spot 54	345.7	2.9
-Spot 100	346.5	3.2
-Spot 165	347.6	2.7
-Spot 30	347.8	2.9
-Spot 64	348.1	2.7
-Spot 157	349.1	2.9
-Spot 124	349.5	3.0
-Spot 96	349.8	2.9
-Spot 118	350.0	2.8
-Spot 133	350.0	3.3
-Spot 125	350.3	2.7
-Spot 146	350.5	3.1
-Spot 183	350.5	3.8
-Spot 67	351.0	3.0
-Spot 156	351.2	3.4
-Spot 21	351.2	3.0
-Spot 123	351.4	3.1
-Spot 190	351.7	3.8
-Spot 188	352.0	2.9
-Spot 203	352.4	4.4
-Spot 114	352.6	3.5
-Spot 184	353.7	3.7
-Spot 163	354.4	2.8
-Spot 1	354.8	2.8
-Spot 103	354.8	2.8
-Spot 20	354.8	3.3
-Spot 5	355.0	3.8
-Spot 134	355.0	3.0
-Spot 22	355.5	4.0
-Spot 194	355.7	2.9
-Spot 105	355.7	3.1

Sample SE1E 1907		
Lat: S 31°49'48.4" Lon: W 069°14'57.3"		
Analysis	**Best age (Ma)**	**± (Ma)**
-Spot 68	355.8	2.7
-Spot 137	356.0	3.5
-Spot 193	356.1	2.8
-Spot 202	356.1	3.1
-Spot 65	356.3	3.0
-Spot 83	357.0	2.8
-Spot 191	357.4	4.2
-Spot 115	357.7	3.3
-Spot 93	358.2	4.0
-Spot 76	358.3	3.0
-Spot 45	359.5	3.0
-Spot 75	359.5	2.6
-Spot 206	359.8	3.7
-Spot 50	360.2	3.5
-Spot 187	360.9	3.6
-Spot 185	360.9	3.6
-Spot 48	361.0	3.6
-Spot 210	361.3	3.7
-Spot 127	362.2	4.2
-Spot 97	362.9	4.1
-Spot 99	363.0	3.1
-Spot 172	363.8	2.9
-Spot 89	364.0	3.9
-Spot 162	364.3	3.1
-Spot 73	364.6	4.3
-Spot 33	364.8	3.6
-Spot 8	364.9	2.4
-Spot 148	365.0	4.2
-Spot 145	365.4	4.3
-Spot 88	365.4	4.2
-Spot 51	365.6	3.7
-Spot 71	366.0	3.1
-Spot 23	366.2	3.8
-Spot 19	366.2	3.5
-Spot 72	366.2	4.6
-Spot 81	366.5	3.3
-Spot 17	366.9	5.3
-Spot 16	367.0	4.4
-Spot 91	367.3	4.0

Sample SE1E 1907		
Lat: S 31°49'48.4" Lon: W 069°14'57.3"		
Analysis	**Best age (Ma)**	**± (Ma)**
-Spot 29	367.5	3.7
-Spot 106	367.6	3.1
-Spot 26	367.6	4.0
-Spot 158	367.7	4.3
-Spot 218	368.1	4.0
-Spot 102	368.2	5.1
-Spot 78	368.8	3.8
-Spot 85	369.0	4.7
-Spot 46	369.1	3.3
-Spot 169	369.3	4.7
-Spot 7	370.0	3.2
-Spot 205	370.3	3.2
-Spot 47	371.2	3.7
-Spot 178	371.4	3.6
-Spot 121	372.0	3.5
-Spot 44	372.5	3.1
-Spot 122	372.5	3.9
-Spot 142	372.5	4.1
-Spot 116	372.9	4.6
-Spot 82	373.1	6.0
-Spot 57	373.3	3.9
-Spot 62	373.5	3.9
-Spot 200	375.6	4.8
-Spot 209	375.7	3.7
-Spot 175	379.4	7.0
-Spot 4	379.7	3.3
-Spot 41	385.3	5.6
-Spot 167	429.0	3.6
-Spot 9	454.5	4.6
-Spot 66	461.3	4.1
-Spot 98	462.9	3.8
-Spot 214	467.9	3.8
-Spot 189	472.8	4.4
-Spot 198	472.9	4.7
-Spot 182	475.7	4.1
-Spot 86	476.8	4.4
-Spot 92	511.7	4.5
-Spot 152	515.3	5.0
-Spot 220	522.1	4.7

Sample SE1E 1907		
Lat: S 31°49'48.4" Lon: W 069°14'57.3"		
Analysis	**Best age (Ma)**	**± (Ma)**
-Spot 87	541.0	5.0
-Spot 36	628.1	4.6
-Spot 55	633.6	6.0
-Spot 95	635.2	4.6
-Spot 132	666.9	8.0
-Spot 10	746.2	5.3
-Spot 28	943.5	13.2
-Spot 216	953.3	14.3
-Spot 131	984.4	19.8
-Spot 104	988.6	13.3
-Spot 201	994.7	11.4
-Spot 117	1017.9	12.3
-Spot 90	1020.8	21.1
-Spot 84	1022.6	12.7
-Spot 151	1041.6	15.9
-Spot 181	1044.7	16.4
-Spot 32	1045.4	13.7
-Spot 140	1047.4	11.6
-Spot 31	1048.2	12.0
-Spot 58	1049.7	19.8
-Spot 15	1050.0	14.1
-Spot 208	1052.7	10.5
-Spot 149	1054.3	16.5
-Spot 70	1059.7	15.7
-Spot 174	1064.5	13.4
-Spot 2	1066.6	12.2
-Spot 141	1068.5	17.6
-Spot 14	1071.5	13.0
-Spot 168	1071.8	13.4
-Spot 13	1075.9	11.4
-Spot 180	1077.0	10.1
-Spot 173	1086.6	11.1
-Spot 24	1088.1	10.7
-Spot 144	1091.1	15.9
-Spot 12	1092.5	12.0
-Spot 199	1093.7	15.0
-Spot 170	1095.4	16.0
-Spot 207	1095.5	13.6
-Spot 113	1099.8	14.2

Sample SE1E 1907		
Lat: S 31°49'48.4" Lon: W 069°14'57.3"		
Analysis	**Best age (Ma)**	**± (Ma)**
-Spot 77	1103.2	18.3
-Spot 39	1103.5	21.2
-Spot 6	1106.5	14.5
-Spot 192	1113.2	12.0
-Spot 35	1115.2	16.9
-Spot 215	1119.2	11.9
-Spot 196	1120.2	16.4
-Spot 179	1129.4	15.4
-Spot 126	1141.7	13.0
-Spot 53	1146.2	20.7
-Spot 34	1150.6	10.8
-Spot 155	1150.7	15.2
-Spot 171	1158.4	9.4
-Spot 52	1164.2	12.0
-Spot 60	1177.5	15.8
-Spot 176	1177.7	13.9
-Spot 211	1192.0	13.2
-Spot 108	1192.0	13.9
-Spot 59	1195.2	15.6
-Spot 101	1196.8	15.6
-Spot 110	1200.9	11.6
-Spot 94	1210.7	19.4
-Spot 128	1212.8	13.3
-Spot 197	1213.3	12.4
-Spot 25	1213.8	13.4
-Spot 130	1215.4	16.4
-Spot 111	1218.9	17.4
-Spot 63	1221.8	13.4
-Spot 186	1223.3	12.8
-Spot 69	1228.7	18.2
-Spot 150	1259.1	13.6
-Spot 143	1278.3	15.4
-Spot 109	1315.5	11.3
-Spot 120	1324.1	8.7
-Spot 138	1326.8	11.6
-Spot 79	1328.3	14.0
-Spot 195	1338.2	26.4
-Spot 139	1339.4	15.5
-Spot 153	1360.5	28.9

Sample SE1E 1907		
Lat: S 31°49'48.4" Lon: W 069°14'57.3"		
Analysis	**Best age (Ma)**	**± (Ma)**
-Spot 74	1366.3	13.7
-Spot 37	1367.1	11.7
-Spot 56	1370.3	11.8
-Spot 119	1371.0	13.2
-Spot 204	1379.8	13.3
-Spot 166	1388.5	11.0
-Spot 147	1395.5	11.9
-Spot 177	1404.3	15.0
-Spot 129	1404.4	16.3
-Spot 213	1427.3	12.9
-Spot 43	1428.8	11.3
-Spot 135	1439.9	10.0
-Spot 42	1440.3	12.1
-Spot 38	1519.6	18.3
-Spot 161	1868.9	11.2
-Spot 154	1941.0	12.1
-Spot 112	1987.4	10.0
-Spot 217	2516.9	13.5
-Spot 80	2785.8	97.5

Sample SE1F 1910		
Lat: S 31°50'02.0" Lon: W 069°15'00.2"		
Analysis	**Best age (Ma)**	**± (Ma)**
-Spot 210	353.0	3.9
-Spot 15	367.0	4.3
-Spot 60	401.6	4.1
-Spot 183	406.5	3.0
-Spot 97	436.4	3.0
-Spot 54	442.5	3.3
-Spot 156	449.2	6.2
-Spot 24	453.0	5.1
-Spot 180	456.0	4.3
-Spot 144	458.0	5.3
-Spot 137	459.3	3.4
-Spot 18	459.6	7.1
-Spot 11	459.8	6.7
-Spot 130	460.4	4.7
-Spot 167	461.3	4.2
-Spot 188	462.1	5.0
-Spot 135	462.5	3.9
-Spot 79	463.6	6.1
-Spot 91	464.6	4.0
-Spot 26	466.7	4.3
-Spot 70	468.2	4.0
-Spot 172	468.7	5.3
-Spot 179	468.8	3.8
-Spot 190	469.1	5.0
-Spot 110	469.2	5.1
-Spot 102	469.3	3.6
-Spot 128	470.5	4.4
-Spot 117	470.6	3.3
-Spot 14	474.2	5.1
-Spot 108	474.3	4.2
-Spot 165	477.4	3.2
-Spot 6	477.7	4.8
-Spot 1	481.4	3.9
-Spot 174	482.1	3.7
-Spot 89	484.1	7.6
-Spot 139	488.1	4.3
-Spot 187	513.0	6.4
-Spot 141	513.3	7.5
-Spot 132	520.3	3.5

Sample SE1F 1910		
Lat: S 31°50'02.0" Lon: W 069°15'00.2"		
Analysis	**Best age (Ma)**	**± (Ma)**
-Spot 147	522.6	5.2
-Spot 136	524.6	5.4
-Spot 200	525.8	5.8
-Spot 81	530.4	5.0
-Spot 121	531.2	5.1
-Spot 178	534.0	5.8
-Spot 3	535.3	4.3
-Spot 56	538.3	4.8
-Spot 217	539.5	3.6
-Spot 203	551.6	4.8
-Spot 214	609.9	6.8
-Spot 134	612.0	4.4
-Spot 205	620.8	7.9
-Spot 92	623.5	5.9
-Spot 10	652.3	7.2
-Spot 63	660.2	7.8
-Spot 19	660.6	9.4
-Spot 116	676.1	7.1
-Spot 8	682.4	7.9
-Spot 218	696.7	7.8
-Spot 206	700.0	6.0
-Spot 164	805.1	5.9
-Spot 123	818.4	10.1
-Spot 192	862.4	8.3
-Spot 67	934.9	18.8
-Spot 4	940.3	20.1
-Spot 112	973.0	19.1
-Spot 80	982.7	13.5
-Spot 16	985.0	20.0
-Spot 5	986.4	11.8
-Spot 65	1001.3	14.6
-Spot 158	1012.8	16.2
-Spot 75	1017.4	17.3
-Spot 76	1018.3	13.7
-Spot 36	1025.1	18.6
-Spot 208	1026.3	18.0
-Spot 53	1026.7	19.5
-Spot 13	1029.0	25.3
-Spot 148	1029.5	17.9

Sample SE1F 1910		
Lat: S 31°50'02.0" Lon: W 069°15'00.2"		
Analysis	**Best age (Ma)**	**± (Ma)**
-Spot 25	1030.8	11.7
-Spot 2	1031.6	16.3
-Spot 149	1034.4	14.1
-Spot 198	1037.3	14.7
-Spot 154	1037.8	11.7
-Spot 146	1038.4	18.3
-Spot 78	1040.4	14.1
-Spot 57	1042.3	15.3
-Spot 7	1046.2	21.7
-Spot 170	1050.1	17.6
-Spot 87	1050.5	20.0
-Spot 73	1052.2	13.0
-Spot 161	1052.8	16.6
-Spot 68	1053.2	33.1
-Spot 83	1054.4	14.0
-Spot 21	1055.4	21.1
-Spot 35	1057.3	16.2
-Spot 194	1059.0	11.7
-Spot 47	1060.4	25.1
-Spot 129	1063.1	18.0
-Spot 125	1063.2	12.9
-Spot 99	1064.6	21.1
-Spot 100	1067.7	12.0
-Spot 219	1068.3	24.3
-Spot 103	1069.7	11.5
-Spot 101	1072.0	28.5
-Spot 166	1072.6	13.1
-Spot 38	1072.6	17.0
-Spot 131	1074.3	16.2
-Spot 151	1075.5	17.5
-Spot 153	1076.4	13.9
-Spot 220	1077.6	15.6
-Spot 64	1078.3	10.5
-Spot 162	1079.7	11.7
-Spot 171	1080.6	12.6
-Spot 216	1081.3	18.3
-Spot 109	1083.0	11.6
-Spot 72	1083.0	16.9
-Spot 58	1083.3	13.3

Sample SE1F 1910		
Lat: S 31°50'02.0" Lon: W 069°15'00.2"		
Analysis	**Best age (Ma)**	**± (Ma)**
-Spot 69	1086.7	17.4
-Spot 12	1089.5	12.9
-Spot 202	1089.9	14.7
-Spot 175	1090.3	8.9
-Spot 182	1090.8	11.9
-Spot 105	1090.8	24.0
-Spot 44	1091.1	17.4
-Spot 181	1091.5	15.6
-Spot 177	1091.5	14.7
-Spot 107	1091.9	17.7
-Spot 49	1096.1	13.3
-Spot 186	1099.3	16.3
-Spot 29	1102.4	16.3
-Spot 45	1105.4	18.9
-Spot 115	1106.0	13.7
-Spot 17	1107.2	17.4
-Spot 176	1107.3	18.1
-Spot 71	1108.4	13.1
-Spot 30	1108.8	15.8
-Spot 96	1109.3	44.6
-Spot 50	1110.1	11.1
-Spot 133	1110.9	16.9
-Spot 124	1112.0	15.4
-Spot 169	1114.1	19.7
-Spot 113	1115.0	14.6
-Spot 85	1115.8	27.9
-Spot 59	1119.3	13.9
-Spot 46	1120.2	17.0
-Spot 43	1121.4	18.4
-Spot 106	1125.3	14.4
-Spot 94	1128.7	19.8
-Spot 48	1131.0	12.0
-Spot 184	1134.0	16.5
-Spot 155	1140.7	19.1
-Spot 163	1141.6	17.2
-Spot 51	1142.6	12.8
-Spot 88	1143.7	15.3
-Spot 77	1146.8	21.4
-Spot 31	1146.8	18.2

Sample SE1F 1910		
Lat: S 31°50'02.0" Lon: W 069°15'00.2"		
Analysis	**Best age (Ma)**	**± (Ma)**
-Spot 145	1149.3	16.3
-Spot 41	1152.3	16.1
-Spot 27	1154.9	16.8
-Spot 93	1160.9	16.2
-Spot 209	1163.1	13.6
-Spot 23	1163.5	14.2
-Spot 37	1163.6	17.8
-Spot 150	1165.4	11.7
-Spot 152	1166.2	14.0
-Spot 213	1170.6	12.1
-Spot 34	1177.0	13.7
-Spot 42	1178.8	13.6
-Spot 142	1179.5	17.6
-Spot 20	1180.5	17.0
-Spot 32	1183.4	16.4
-Spot 119	1185.9	14.2
-Spot 114	1189.7	14.7
-Spot 111	1191.5	16.0
-Spot 212	1191.8	10.5
-Spot 82	1196.6	14.9
-Spot 159	1202.3	13.1
-Spot 55	1204.3	12.8
-Spot 204	1222.5	13.6
-Spot 191	1228.4	19.3
-Spot 40	1234.5	14.1
-Spot 157	1235.7	14.7
-Spot 201	1239.5	12.3
-Spot 160	1253.1	12.7
-Spot 28	1258.5	13.1
-Spot 196	1258.5	19.9
-Spot 33	1262.7	11.3
-Spot 211	1269.9	14.5
-Spot 197	1276.1	14.4
-Spot 138	1277.8	16.1
-Spot 199	1284.8	18.9
-Spot 215	1290.7	21.1
-Spot 195	1307.4	14.2
-Spot 84	1309.8	28.8
-Spot 173	1310.6	26.4

Sample SE1F 1910		
Lat: S 31°50'02.0" Lon: W 069°15'00.2"		
Analysis	**Best age (Ma)**	**± (Ma)**
-Spot 120	1313.4	14.9
-Spot 22	1316.1	25.5
-Spot 193	1332.4	13.5
-Spot 95	1344.4	16.1
-Spot 52	1351.9	33.1
-Spot 98	1352.1	15.8
-Spot 118	1355.3	13.0
-Spot 122	1356.5	10.6
-Spot 66	1387.8	13.2
-Spot 39	1388.1	14.4
-Spot 143	1400.6	17.1
-Spot 140	1416.2	14.0
-Spot 189	1461.7	13.7
-Spot 61	1488.2	11.7
-Spot 168	1511.0	22.0
-Spot 185	1521.6	13.3
-Spot 74	1748.6	22.5
-Spot 90	2036.4	11.5
-Spot 62	2129.5	15.9

Sample SE1F 1911		
Lat: S 31°50'10.0" Lon: W 069°14'54.1"		
Analysis	**Best age (Ma)**	**± (Ma)**
-Spot 62	337.8	3.5
-Spot 202	341.7	3.4
-Spot 35	351.3	3.2
-Spot 126	353.5	2.6
-Spot 201	375.4	3.2
-Spot 288	381.6	3.3
-Spot 157	388.5	3.4
-Spot 176	399.7	4.6
-Spot 96	402.4	4.2
-Spot 174	407.2	5.8
-Spot 76	409.9	4.3
-Spot 236	418.5	3.6
-Spot 211	433.9	3.9
-Spot 270	446.3	4.8
-Spot 237	455.4	3.8
-Spot 158	456.1	2.7
-Spot 156	458.4	4.6
-Spot 7	458.4	5.5
-Spot 105	458.5	6.5
-Spot 287	458.5	4.6
-Spot 75	458.8	5.3
-Spot 258	459.9	3.9
-Spot 63	460.2	5.6
-Spot 137	460.6	5.1
-Spot 110	460.8	3.4
-Spot 206	460.8	3.5
-Spot 181	461.5	3.8
-Spot 220	461.8	4.7
-Spot 146	462.1	4.9
-Spot 40	462.1	4.5
-Spot 261	462.3	3.6
-Spot 132	462.3	5.0
-Spot 133	462.7	4.1
-Spot 251	463.3	4.0
-Spot 238	465.0	3.5
-Spot 188	466.0	3.8
-Spot 70	466.0	4.4
-Spot 204	466.1	5.3
-Spot 274	466.4	4.2

Sample SE1F 1911		
Lat: S 31°50'10.0" Lon: W 069°14'54.1"		
Analysis	**Best age (Ma)**	**± (Ma)**
-Spot 265	466.4	4.2
-Spot 271	467.0	3.8
-Spot 224	467.2	4.8
-Spot 249	468.2	5.7
-Spot 160	468.3	5.7
-Spot 245	468.8	4.6
-Spot 128	469.1	4.3
-Spot 125	469.2	4.5
-Spot 214	469.8	4.5
-Spot 117	470.0	4.7
-Spot 205	471.4	4.1
-Spot 175	471.5	4.7
-Spot 177	471.8	5.1
-Spot 74	472.0	6.0
-Spot 140	472.3	3.9
-Spot 286	473.0	5.4
-Spot 88	473.9	3.8
-Spot 269	474.0	5.3
-Spot 216	474.2	4.3
-Spot 171	474.9	5.7
-Spot 210	475.4	4.1
-Spot 1	475.9	4.2
-Spot 113	476.3	4.6
-Spot 192	476.5	4.4
-Spot 97	477.1	4.0
-Spot 91	478.1	3.5
-Spot 9	479.3	5.0
-Spot 196	479.4	6.5
-Spot 198	479.6	4.9
-Spot 193	479.7	4.3
-Spot 239	480.1	3.9
-Spot 257	480.3	5.9
-Spot 221	481.5	4.9
-Spot 78	481.7	3.1
-Spot 50	481.9	7.1
-Spot 254	483.6	4.2
-Spot 243	483.9	6.3
-Spot 213	484.2	5.9
-Spot 232	486.8	5.0

Sample SE1F 1911		
Lat: S 31°50'10.0" Lon: W 069°14'54.1"		
Analysis	**Best age (Ma)**	**± (Ma)**
-Spot 141	487.3	4.2
-Spot 60	487.6	5.0
-Spot 273	488.3	4.8
-Spot 233	491.4	5.6
-Spot 147	505.1	6.1
-Spot 285	512.1	4.6
-Spot 227	514.7	5.0
-Spot 186	516.6	5.7
-Spot 102	517.1	4.0
-Spot 53	517.4	4.4
-Spot 246	517.9	3.8
-Spot 52	520.2	4.1
-Spot 242	522.6	4.6
-Spot 260	522.8	5.2
-Spot 79	524.7	4.5
-Spot 134	525.9	4.8
-Spot 279	526.2	4.5
-Spot 136	526.8	5.5
-Spot 22	527.5	4.3
-Spot 215	527.7	5.3
-Spot 99	527.7	5.1
-Spot 165	528.7	5.2
-Spot 226	529.7	3.7
-Spot 179	533.2	4.4
-Spot 212	533.4	3.9
-Spot 87	533.9	4.7
-Spot 36	538.3	4.4
-Spot 92	538.8	3.4
-Spot 267	539.2	6.8
-Spot 155	540.7	5.1
-Spot 30	541.9	4.4
-Spot 120	544.7	4.0
-Spot 289	546.7	6.8
-Spot 277	549.9	4.9
-Spot 119	550.3	4.4
-Spot 57	552.4	4.5
-Spot 11	554.6	6.2
-Spot 61	556.3	4.8
-Spot 20	557.0	4.7

Sample SE1F 1911		
Lat: S 31°50'10.0" Lon: W 069°14'54.1"		
Analysis	**Best age (Ma)**	**± (Ma)**
-Spot 240	557.5	5.3
-Spot 290	565.2	5.6
-Spot 104	565.4	5.1
-Spot 235	568.1	3.9
-Spot 169	569.7	3.8
-Spot 127	575.9	5.1
-Spot 184	576.6	4.7
-Spot 58	579.6	6.3
-Spot 225	580.8	5.5
-Spot 48	583.5	5.5
-Spot 83	586.1	4.8
-Spot 163	587.0	4.7
-Spot 56	587.9	4.6
-Spot 152	590.6	5.9
-Spot 17	598.7	5.9
-Spot 80	601.9	5.4
-Spot 266	606.0	5.0
-Spot 95	609.5	4.6
-Spot 276	613.8	5.7
-Spot 10	618.6	6.1
-Spot 15	620.7	7.1
-Spot 4	621.7	6.5
-Spot 145	622.9	6.2
-Spot 3	625.2	5.9
-Spot 219	627.6	8.7
-Spot 24	629.7	7.0
-Spot 13	645.0	6.6
-Spot 77	647.2	6.8
-Spot 262	647.9	7.8
-Spot 106	648.8	6.8
-Spot 85	649.0	8.2
-Spot 195	651.2	7.8
-Spot 218	655.1	6.0
-Spot 44	687.7	7.1
-Spot 191	692.1	19.1
-Spot 172	756.5	8.9
-Spot 26	761.5	10.2
-Spot 167	821.9	10.3
-Spot 180	828.7	8.2

Sample SE1F 1911		
Lat: S 31°50'10.0" Lon: W 069°14'54.1"		
Analysis	**Best age (Ma)**	**± (Ma)**
-Spot 281	844.5	9.5
-Spot 253	854.6	12.2
-Spot 65	872.6	6.5
-Spot 38	873.4	9.7
-Spot 73	942.7	14.0
-Spot 34	957.4	21.8
-Spot 199	959.1	40.4
-Spot 122	963.8	16.8
-Spot 47	964.0	20.5
-Spot 250	972.9	17.1
-Spot 94	994.4	25.5
-Spot 27	998.9	16.9
-Spot 207	1001.6	22.1
-Spot 107	1001.8	19.1
-Spot 203	1005.3	18.6
-Spot 64	1008.1	18.2
-Spot 173	1009.7	10.2
-Spot 268	1012.4	12.7
-Spot 149	1018.7	26.3
-Spot 264	1019.2	13.5
-Spot 112	1023.2	24.3
-Spot 263	1024.1	15.4
-Spot 284	1029.2	23.0
-Spot 230	1029.9	15.5
-Spot 283	1033.5	20.5
-Spot 168	1034.8	12.2
-Spot 16	1034.9	17.3
-Spot 234	1035.2	14.0
-Spot 166	1041.1	13.4
-Spot 187	1046.5	13.6
-Spot 131	1048.7	22.2
-Spot 84	1049.6	11.4
-Spot 178	1050.7	12.8
-Spot 208	1053.9	14.6
-Spot 159	1056.1	20.4
-Spot 144	1056.6	14.4
-Spot 101	1058.5	11.4
-Spot 66	1058.5	24.0
-Spot 109	1059.8	13.9

Sample SE1F 1911		
Lat: S 31°50'10.0" Lon: W 069°14'54.1"		
Analysis	**Best age (Ma)**	**± (Ma)**
-Spot 121	1062.2	13.7
-Spot 114	1062.8	11.5
-Spot 194	1067.9	13.7
-Spot 100	1072.5	12.3
-Spot 39	1074.4	15.9
-Spot 118	1076.1	15.0
-Spot 37	1082.5	13.8
-Spot 278	1085.0	22.1
-Spot 46	1085.4	11.4
-Spot 18	1086.4	24.4
-Spot 123	1087.4	13.1
-Spot 209	1088.1	20.1
-Spot 259	1088.6	14.1
-Spot 45	1089.5	17.1
-Spot 200	1091.1	11.8
-Spot 162	1094.6	14.6
-Spot 108	1094.9	10.2
-Spot 164	1096.3	15.3
-Spot 51	1097.7	13.0
-Spot 143	1099.1	16.6
-Spot 280	1110.1	17.0
-Spot 154	1110.2	27.3
-Spot 28	1112.7	16.5
-Spot 255	1114.5	11.8
-Spot 89	1115.3	12.9
-Spot 282	1116.5	26.5
-Spot 272	1121.6	13.5
-Spot 2	1124.1	17.2
-Spot 5	1129.5	15.5
-Spot 244	1135.3	17.6
-Spot 43	1138.6	12.9
-Spot 42	1143.8	16.0
-Spot 161	1144.9	17.8
-Spot 116	1150.6	11.4
-Spot 90	1152.7	30.9
-Spot 222	1159.5	16.0
-Spot 124	1161.5	12.9
-Spot 228	1162.6	12.2
-Spot 275	1163.8	19.7

Sample SE1F 1911		
Lat: S 31°50'10.0" Lon: W 069°14'54.1"		
Analysis	**Best age (Ma)**	**± (Ma)**
-Spot 25	1164.3	13.5
-Spot 185	1167.7	14.0
-Spot 81	1169.0	12.0
-Spot 182	1173.5	12.5
-Spot 86	1179.4	16.6
-Spot 252	1182.2	12.7
-Spot 217	1189.6	13.7
-Spot 59	1190.0	11.3
-Spot 256	1203.6	13.9
-Spot 29	1207.6	15.2
-Spot 93	1209.4	12.9
-Spot 19	1209.5	27.5
-Spot 67	1220.3	9.7
-Spot 248	1245.4	16.4
-Spot 32	1252.5	14.3
-Spot 142	1253.5	15.6
-Spot 69	1256.2	16.7
-Spot 54	1261.8	14.8
-Spot 103	1276.4	16.4
-Spot 223	1290.2	14.2
-Spot 189	1339.5	12.9
-Spot 111	1346.0	21.9
-Spot 33	1346.9	15.3
-Spot 55	1353.7	13.3
-Spot 129	1366.4	14.3
-Spot 190	1368.8	8.5
-Spot 153	1373.1	11.5
-Spot 231	1381.8	12.6
-Spot 49	1393.9	25.3
-Spot 41	1443.3	11.6
-Spot 130	1689.1	9.9
-Spot 247	1851.3	14.3
-Spot 170	2020.9	11.1
-Spot 98	2671.4	10.7
-Spot 8	2816.7	10.5
-Spot 138	3117.0	13.1
-Spot 6	3412.2	10.3